

2014-01-01

3D Printed Spatially Variant Anisotropic Metamaterials

Cesar Roman Garcia

University of Texas at El Paso, cg0210794@gmail.com

Follow this and additional works at: https://digitalcommons.utep.edu/open_etd



Part of the [Electrical and Electronics Commons](#)

Recommended Citation

Garcia, Cesar Roman, "3D Printed Spatially Variant Anisotropic Metamaterials" (2014). *Open Access Theses & Dissertations*. 848.
https://digitalcommons.utep.edu/open_etd/848

This is brought to you for free and open access by DigitalCommons@UTEP. It has been accepted for inclusion in Open Access Theses & Dissertations by an authorized administrator of DigitalCommons@UTEP. For more information, please contact lweber@utep.edu.

3D PRINTED SPATIALLY VARIANT
ANISOTROPIC METAMATERIALS

CESAR ROMAN GARCIA

Department of Electrical and Computer Engineering

APPROVED:

Raymond Rumpf, Ph.D., Chair

Joseph Pierluissi, Ph.D.

Virgilio Gonzalez, Ph.D.

Helmut Knaust, Ph.D.

Bess Sirmon-Taylor, Ph.D.
Interim Dean of the Graduate School

Copyright ©

by

Cesar Roman Garcia

2014

3D PRINTED SPATIALLY VARIANT
ANISOTROPIC METAMATERIALS

by

CESAR ROMAN GARCIA, BSEP

DISSERTATION

Presented to the Faculty of the Graduate School of
The University of Texas at El Paso
in Partial Fulfillment
of the Requirements
for the Degree of

DOCTOR OF PHILOSOPHY

Department of Electrical and Computer Engineering

THE UNIVERSITY OF TEXAS AT EL PASO

May 2014

Acknowledgements

Primarily, I would like to thank my family for their support during my graduate studies. Thank you to my wife, Dalia, who put up with a husband in graduate school, my parents, Mom and Dad, for always supporting me, and my son, Cesar Rene, who I have spent so much time away from.

Thank you to my advisor, Dr. Raymond Rumpf (Tipper), for mentoring and teaching me during this process of obtaining my Ph.D. I have learned a great deal from you. Also, I would like to thank my committee members for their time and their contributions: Dr. Virgilio Gonzalez, Dr. Joseph Pierluissi, and Dr. Helmut Knaust.

Thank you to Dr. Benjamin Flores, Dr. Helmut Knaust, and Mrs. Ariana Arciero-Pino. I am extremely grateful for your advice and for receiving the NSF Bridge to Doctorate Fellowship.

Finally, I would like to acknowledge my work wife, J.H.B., there will always be a filing cabinet in between us.

Abstract

The recent advancement in 3D printing has created a new way to design electronics and electromagnetic devices. This allows for a new breed of non-planar designs to be used, fully exploiting all three dimensions like never before. More functions can be fit into the same amount of space, products with novel form factors can be more easily manufactured, interconnects can be routed more smoothly, interfaces can be better implemented, electrical and mechanical functions can be comingled, and entirely new device paradigms will be invented. When departing from traditional planar topologies many new problems arise like signal integrity, crosstalk, noise, and unintentional coupling between devices. The primary focus of this dissertation is to demonstrate that spatially variant anisotropic metamaterials (SVAM's) are a viable solution to alleviate those unwanted problems. Currently, there are no solutions to fix these problems in a fully 3D device, but there have been numerous efforts to alleviate those problems in traditional devices. Those solutions often use metals that introduce unwanted loss and require extra space to be added to the device. SVAM's do not introduce significant loss, since they are all-dielectric, and better accommodate systems that have size restraints.

To be able to design and model SVAM's, six numerical tools were formulated and implemented. In addition, one commercial software package was used.

First, a design methodology was developed for generating an all-dielectric metamaterial with a specific dielectric tensor. Next, a microstrip transmission line was isolated from a metal object placed in close proximity by embedding it in a SVAM so that the field avoided the object. Next, the electromagnetic impact of the typical surface roughness in metal parts produced by 3D print metals was evaluated. Finally, a SVAM was built into a cell phone case to minimize the interaction of two cell phone antennas in close proximity.

Table of Contents

Acknowledgements.....	iv
Abstract.....	v
Table of Contents.....	vi
List of Tables	viii
List of Figures.....	ix
Chapter 1: Introduction.....	1
1.1 Overview of Dissertation	1
1.2 3D Printing.....	2
1.3 Anisotropic Materials.....	5
1.4 Electromagnetic Metamaterials	5
1.5 State-of-the-Art in Electromagnetic Isolation.....	7
Chapter 2: Numerical Tools.....	10
2.1 Ansys® HFSS.....	10
2.2 4×4 Transfer Matrix Method for Anisotropic Materials (ATMM)	10
2.3 2D Plane Wave Expansion Method	20
2.4 Finite-Difference Analysis of Arbitrary Transmission Lines Embedded in Anisotropic Media	23
2.5 Anisotropic Finite-Difference Frequency-Domain Method	31
2.6 Tool for Synthesizing Spatially Variant Lattices.....	42
2.7 Transformation Optics	47
Chapter 3: 3D Printing of Anisotropic Metamaterials.....	54
3.1 Device Design.....	54
3.2 Experimental Results	57
3.3 Conclusions.....	60
Chapter 4: Electromagnetic Isolation of A Microstrip by Embedding in a Spatially Variant Anisotropic Metamaterial	61
4.1 Microstrip embedded in anisotropic media.....	61
4.2 Device Design.....	63
4.3 Experimental Results	66

4.4	Conclusions.....	70
Chapter 5: Effects of Extreme Surface Roughness on a 3D Printed Horn Antenna		71
5.1	Device and Manufacturing.....	71
5.2	Experimental Results	73
5.4	Conclusions.....	75
Chapter 6: Electromagnetic Isolation of Cell Phone Antennas by Embedding in a Spatially Variant Anisotropic Metamaterial		76
6.1	Envelope Correlation Coefficient	76
6.2	Cell Phone Antenna Design	77
6.3	Effects of Second Antenna.....	79
6.4	SVAM Design.....	82
6.5	SVAM Reduction of ECC	84
6.6	Conclusions.....	85
Chapter 7: Conclusions.....		86
7.1	Conclusions.....	86
7.2	Suggestion for Future Work.....	87
References.....		89
Appendix.....		93
A1	Derivation of Expression for Scattering Parameters.....	93
A2	Derivation of Redheffer Star Product	97
Vita.....		99

List of Tables

Table 5.1.1: Measured lengths of horn antennas	73
Table 5.1.2: Simulated and measured gain at 15 GHz at normal incidence	73
Table 6.6.1: ECC.....	85

List of Figures

Figure 1.2.1: Illustration of FDM machine [8]	3
Figure 1.2.2: Illustration for SL machine [9]	4
Figure 1.2.3: Illustration of EBM machine [11]	4
Figure 1.4.1: Sub-sections of engineered materials [12]	6
Figure 1.4.2: Photonic Band Diagram of light lines and real bands [12]	7
Figure 1.5.1: State-of-the-Art in microstrip isolation	8
Figure 1.5.2: State-of-the-Art in antenna isolation	9
Figure 2.2.1: 3D to 1D homogenization [12]	11
Figure 2.2.2: Geometry of an embedded layer [12]	18
Figure 2.4.1: 4×4 grid for the finite-difference solution to Eq. (2.80)	26
Figure 2.4.2: Grid strategy for finite-difference analysis of a microstrip transmission line	29
Figure 2.4.3: Four arrays describing the distribution of dielectric	30
Figure 2.4.4: Numerical results for an ordinary microstrip	30
Figure 2.5.1 3D Yee cell along with position of the tensor elements	34
Figure 2.5.2: Anisotropic GMR filter spectral response simulated with Ansys HFSS b) Anisotropic GMR spectral response simulated with AFDFD	41
Figure 2.5.3: Prototype of anisotropic GMR filter	42
Figure 2.6.1: Metamaterial unit cell and its constituent 1D gratings [12]	43
Figure 2.6.2: Direction field and resulting spatially variant lattice [12]	44
Figure 2.6.3: Lattice period field and resulting spatially variant lattice [12]	44
Figure 2.6.4.: Correct method for generating spatially variant 1D gratings [12]	46
Figure 2.7.1: Example of coordinate transformation [12]	48
Figure 2.7.2: Material parameters for a far-zone lens	51
Figure 2.7.3: Simulated far zone lens using AFDFD	51
Figure 2.7.4: Material Parameters of Cloak	52
Figure 2.7.5: AFDFD simulation of cloak	53
Figure 3.1.1: Pictures of various unit cells simulated	56
Figure 3.1.2: Double Parameter Sweep of Anisotropic Unit Cell	57
Figure 3.2.1: Manufactured Anisotropic Metamaterials	58
Figure 3.2.2: Materials under test. (Top) Rods in the z-direction. (Middle) Rods in the y- direction. (Bottom) Rods in the x-direction	59
Figure 3.2.3: Measured dielectric tensor	60
Figure 4.1.1: Study on the effect of the strength of the anisotropy of the surrounding medium	61
Figure 4.1.2: Study on the effect of the strength of spatially varying the anisotropy of the surrounding medium	62
Figure 4.1.3: Rigorous 3D simulation of standard microstrip transmission line with and without a metal ball placed in close proximity.	63
Figure 4.1.4: Rigorous 3D simulation of standard microstrip transmission line with and without a metal ball placed in close proximity.	63
Figure 4.2.1: Cross section of the unit cell. For $\epsilon_{r1} = 40$ and $\epsilon_{r2} = 2.33$, the optimized ratio d/a is 0.8	65
Figure 4.2.2: SVAM to be placed on top of an otherwise ordinary microstrip	65
Figure 4.2.3: Orientation of the anisotropy of the SVAM	66
Figure 4.3.1: 3D printed spatially variant anisotropic metamaterial	67

Figure 4.3.2: SVAM packed with TiO ₂ nano-powder	68
Figure 4.3.3: Microstrip transmission line in test setup, with and without the SVAM in place...	68
Figure 4.3.4: Reflection from the bare microstrip, with and without the SVAM in place	69
Figure 4.3.5: Change in S11 as ball is placed and removed for two cases: (1) solid blue line is for the microstrip in air, and (2) dashed red line is for the microstrip embedded in the SVAM.....	70
Figure 5.1.1: (a) Reference horn, (b) 3D printed horn #1, (c) 3D printed horn #2	71
Figure 5.1.2: Geometry of horn antennas	72
Figure 5.2.1: Experimental Setup	74
Figure 5.2.2: Measured transmission	74
Figure 6.1.1: One IFA design	77
Figure 6.1.2: Simulated IFA	78
Figure 6.2.3: 3D field radiation pattern of IFA at 740 MHz.....	79
Figure 6.3.1: Two IFA design.....	80
Figure 6.3.2: Simulated two antenna design	80
Figure 6.3.3: Near-field of two IFA's	81
Figure: 6.3.4: 3D field radiation pattern of IFA one excited at 660 MHz	82
Figure 6.4.1: SVAM unit cell design	83
Figure 6.4.2: SVAM to be incorporated in cell phone packaging	83
Figure 6.4.2: Simulated cell phone with SVAM.....	84
Figure 6.4.3: Near-field of two IFA's embedded in a SVAM	85
Figure 7.2.1: Cell phone with SVAM design	87
Figure 7.2.2: Illustration of hybrid algorithm composed of transformation optics and spatially variant synthesis.....	88

Chapter 1: Introduction

1.1 Overview of Dissertation

3D printing is on the verge of revolutionizing manufacturing [1] and changing the way electronics and electromagnetic devices are designed. 3D printing allows for materials to be placed arbitrarily in three dimensions with extremely high precision. This enables a new breed of non-planar designs to be used, which fully exploit all three dimensions like never before. More functions can be fit into the same amount of space, products with novel form factors can be more easily manufactured, interconnect can be routed more smoothly, interfaces can be better implemented, electrical and mechanical functions can be comingled, and entirely new device paradigms will be invented. [2-5].

When departing from traditional planar topologies many new problems arise like signal integrity, crosstalk, noise, and unintentional coupling between devices. This dissertation proposes spatially variant anisotropic metamaterials (SVAMs) as an all-dielectric technique to mitigate these problems. Anisotropic materials possess a different dielectric response, depending on the direction of the field. In such a case, the permittivity and/or permeability are described by tensors instead of scalar quantities. Inside an anisotropic medium, near-fields tend to develop in the directions with the highest constitutive parameters. This can be confined to a single direction if the anisotropy is uniaxial. By spatially varying the orientation of the anisotropy around a device, the near-field can be sculpted almost arbitrarily on a highly subwavelength scale.

1.1.1 Outline of Dissertation

Chapter 1 introduces the topic of this dissertation and the motivation and the importance of the results obtained. 3D printing is briefly explained, primarily focusing on fused deposition modeling (FDM), electron beam melting (EBM), and stereolithography (SL). Metamaterials and anisotropic materials are introduced. A survey of current state-of-the-art technology is presented.

Chapter 2 provides a brief overview and derivation of all numerical tools used in this dissertation. The tools used were Ansys HFSS (HFSS), 4×4 anisotropic transfer matrix method (ATMM), 2D plane wave expansion method (PWEM), finite-difference analysis, spatiality variant lattice (SVL) tool, and transformation optics (TO).

Chapter 3 summarizes the design methodology for an artificially anisotropic 3D printed metamaterial. The chapter also explains how the design methodology was experimentally verified.

Chapter 4 summarizes how a microstrip transmission line was isolated from a metal object placed in close proximity by embedding it in a SVAM so that the field avoids the object.

Chapter 5 summarizes the evaluation of the electromagnetic impact of the typical surface roughness in metal parts produced when 3D printed with EBM.

Chapter 6 summarizes the reduction of two cell phone antenna's interaction, in close proximity, by building a SVAM into the surrounding cell phone case.

Chapter 7 summarizes this dissertation and highlights the main developments achieved. Suggestions for future work are identified.

1.2 3D Printing

3D printing, or additive manufacturing, is any process that builds a 3D solid object, in virtually any shape, from a digital file in successive layers. 3D printing is considered distinct from traditional machining techniques, which rely on the removal of material [1, 6].

1.2.1 Fused Deposition Modeling

In this process, an inexpensive thermoplastic filament is fed through a print head where it is melted and deposited onto the surface of a platform. The print head is translated across the platform to deposit a layer of material in the desired pattern. After the layer is printed, the platform is lowered and the next layer is printed on top of the previous. This process is repeated for all layers until the part is complete [7]. Figure 1.2.1 depicts how a typical FDM machine works.

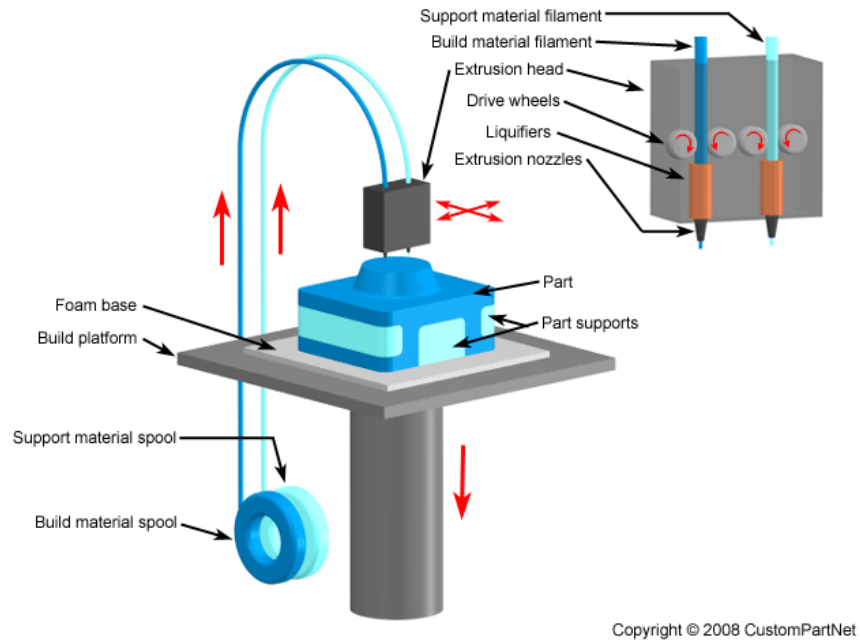


Figure 1.2.1: Illustration of FDM machine [8]

1.2.3 Stereolithography

In this process, a vat of liquid ultraviolet (uv) curable photopolymer, also called resin, is cured with a low-power, highly focused uv-laser, one layer at a time. Each layer, a cross section of the part, is exposed to the uv-laser, which causes the resin to solidify. After the layer solidifies, the platform is then lowered and the process is then repeated until the part is completed [7]. Figure 1.2.2 depicts how a typical SL machine works.

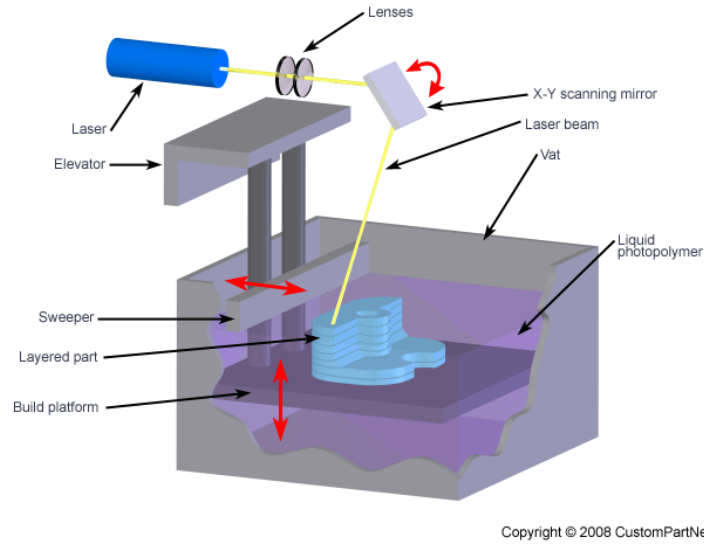


Figure 1.2.2: Illustration for SL machine [9]

1.2.4 Electron Beam Melting

In this process, metal powder is fused together inside a vacuum chamber, one layer at a time, with an electron beam. When a layer is completed, the powder bed is moved and an automated roller adds a new layer of powder; the process is repeated until the part is completed [10]. Figure 1.2.3 depicts how a typical EBM machine works.

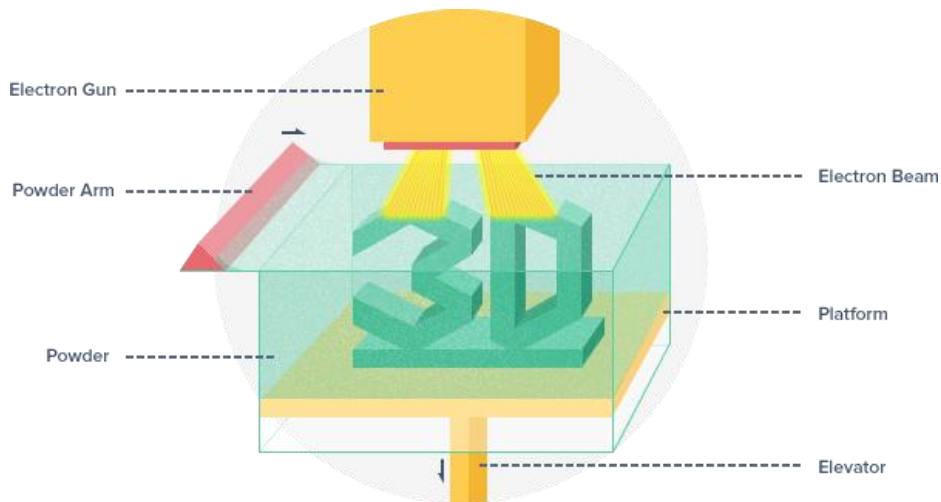


Figure 1.2.3: Illustration of EBM machine [11]

1.3 Anisotropic Materials

In some materials, charges are more easily displaced along certain directions. For this reason, the material can become polarized in directions slightly different than the applied field. In this case, the electric susceptibility, $[\chi_e]$, is a tensor quantity.

$$\begin{bmatrix} P_x(\omega) \\ P_y(\omega) \\ P_z(\omega) \end{bmatrix} = \epsilon_0 \begin{bmatrix} \chi_{xx}(\omega) & \chi_{xy}(\omega) & \chi_{xz}(\omega) \\ \chi_{yx}(\omega) & \chi_{yy}(\omega) & \chi_{yz}(\omega) \\ \chi_{zx}(\omega) & \chi_{zy}(\omega) & \chi_{zz}(\omega) \end{bmatrix} \begin{bmatrix} E_x(\omega) \\ E_y(\omega) \\ E_z(\omega) \end{bmatrix} \quad (1.1)$$

This is most often treated through a dielectric tensor.

$$\tilde{\epsilon}_r(\omega) = 1 + \chi_e(\omega) \quad (1.2)$$

The constitutive relation between the electric field, \vec{E} , and the electric flux density, \vec{D} , in an anisotropic medium is

$$\begin{bmatrix} D_x(\omega) \\ D_y(\omega) \\ D_z(\omega) \end{bmatrix} = \epsilon_0 \begin{bmatrix} \tilde{\epsilon}_{xx}(\omega) & \tilde{\epsilon}_{xy}(\omega) & \tilde{\epsilon}_{xz}(\omega) \\ \tilde{\epsilon}_{yx}(\omega) & \tilde{\epsilon}_{yy}(\omega) & \tilde{\epsilon}_{yz}(\omega) \\ \tilde{\epsilon}_{zx}(\omega) & \tilde{\epsilon}_{zy}(\omega) & \tilde{\epsilon}_{zz}(\omega) \end{bmatrix} \begin{bmatrix} E_x(\omega) \\ E_y(\omega) \\ E_z(\omega) \end{bmatrix} \quad (1.3)$$

Analogously, this can be done for the magnetic flux density, B , using the magnetic susceptibility, $[\chi_m]$. This means that the fields are no longer independent of each other [12]. Equation (1.4) is the magnetic response of a fully anisotropic material.

$$\begin{bmatrix} B_x(\omega) \\ B_y(\omega) \\ B_z(\omega) \end{bmatrix} = \mu_0 \begin{bmatrix} \tilde{\mu}_{xx}(\omega) & \tilde{\mu}_{xy}(\omega) & \tilde{\mu}_{xz}(\omega) \\ \tilde{\mu}_{yx}(\omega) & \tilde{\mu}_{yy}(\omega) & \tilde{\mu}_{yz}(\omega) \\ \tilde{\mu}_{zx}(\omega) & \tilde{\mu}_{zy}(\omega) & \tilde{\mu}_{zz}(\omega) \end{bmatrix} \begin{bmatrix} H_x(\omega) \\ H_y(\omega) \\ H_z(\omega) \end{bmatrix} \quad (1.4)$$

1.4 Electromagnetic Metamaterials

Currently, there is no universally accepted definition for metamaterials. The most basic definition of a metamaterial is any material that is simply anything other than an ordinary material [13]. There are recurring themes in literature that describe metamaterials such as: engineered composites [14], material properties that are derived from their physical structure

rather than their chemistry [15], exhibit properties not observed in nature [13], and exhibit properties not observed in their constituent materials [16]. This dissertation offers the following definition: “A composite material that is purposely engineered to provide material properties that are not otherwise attainable with ordinary materials [12].”

Electromagnetic metamaterials fall under the umbrella of engineered materials. Figure 1.4.1 shows the four main classifications of engineered materials. Electromagnetic metamaterials typically have their lattice spacing much smaller than the wavelength of the desired operating frequency [12, 13, 16].

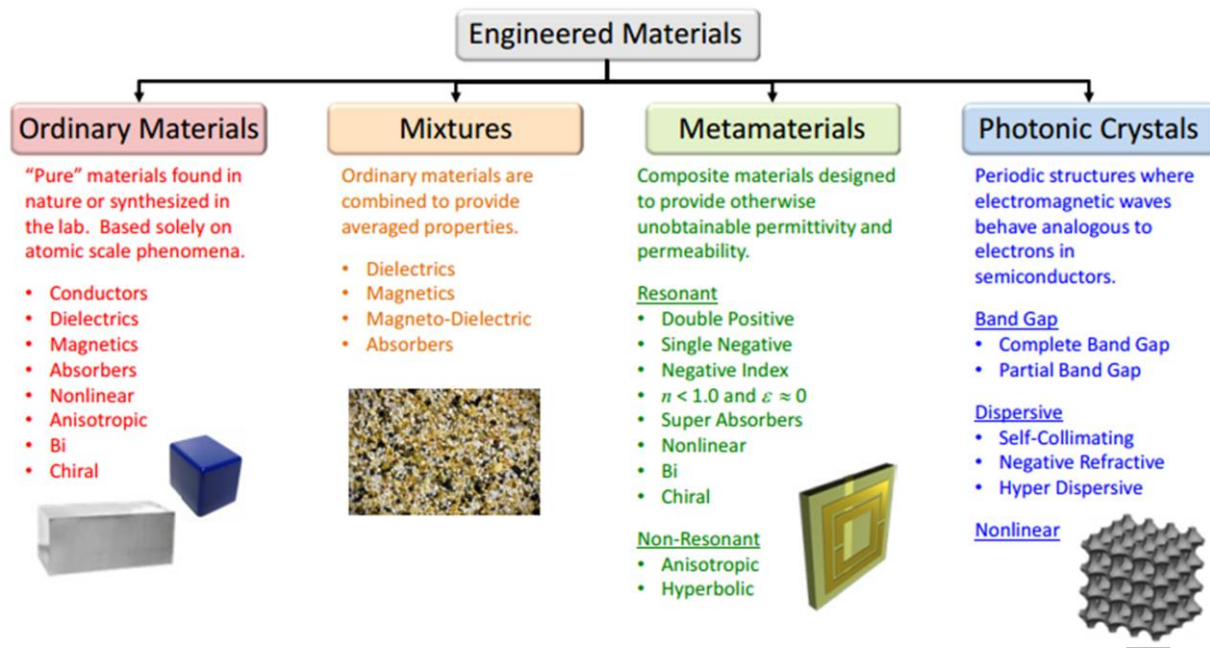


Figure 1.4.1: Sub-sections of engineered materials [12]

A metamaterial is considered to be non-resonant when the light lines do not deviate from the actual calculated bands of the structure. Light lines are the bands that would be calculated from a homogenous structure where the dielectric constant is taken as an average of a composite structure [12]. Figure 1.4.2 depicts this concept and how metamaterials can be categorized based on this framework. The green lines are the light lines and the blue lines are the real bands.

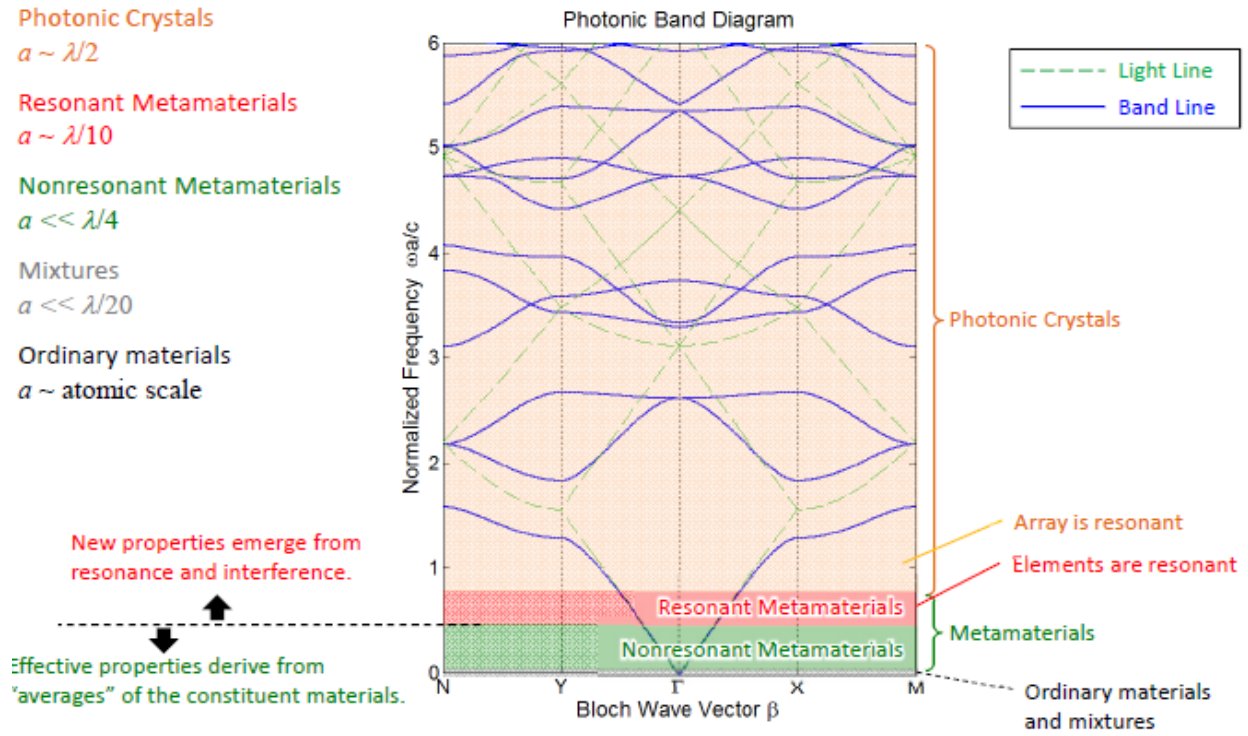


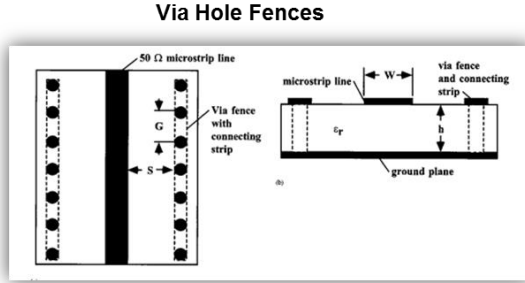
Figure 1.4.2: Photonic Band Diagram of light lines and real bands [12]

In this dissertation, only non-resonate metamaterials were studied. Non-resonate metamaterials were chosen because they are extremely broadband, can be all-dielectric (low loss), can be spatially varied, and can be 3D printed.

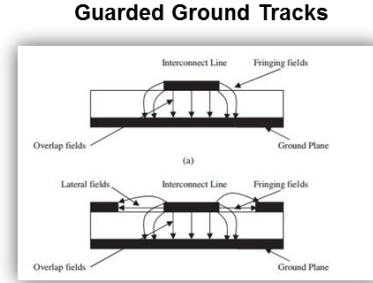
1.5 State-of-the-Art in Electromagnetic Isolation

1.5.1 Microstrip Transmission Line Isolation

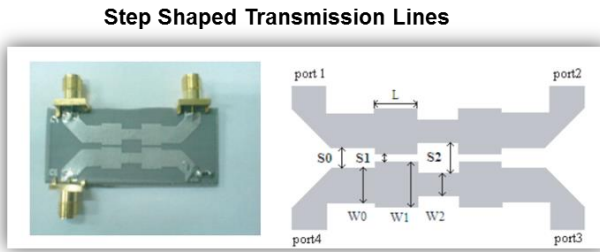
Many solutions have been proposed to reduce coupling and cross talk, including via hole fences [17, 18], guarded ground tracks [19], step shaped transmission lines [20], and even Faraday cages [21]. All of these approaches, however, use metals and can produce even more problems in the framework of a 3D system because the isolation structures themselves occupy space and limit how closely components can be spaced.



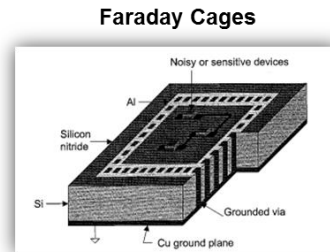
G. E. Ponchak *et al*, *Advanced Packaging, IEEE Transactions on*, vol. 24, pp. 76-80, 2001.



R. Y. Sharma *et al*, *Progress In Electromagnetics Research*, vol. 82, pp. 189-202, 2008.



A. R. Mallahzadeh *et al*, *Progress In Electromagnetics Research C*, vol. 12, pp. 139-148, 2010.

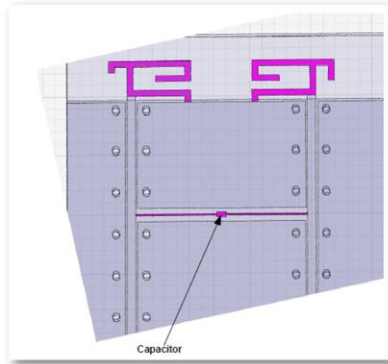


J. H. Wu *et al*, *Microwave and Wireless Components Letters, IEEE*, vol. 11, pp. 410-412, 2001.

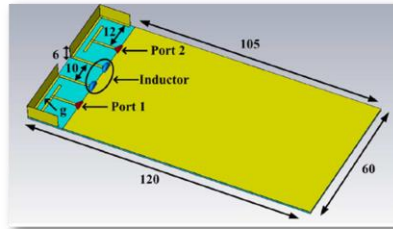
Figure 1.5.1: State-of-the-Art in microstrip isolation

1.5.2 Antenna Isolation

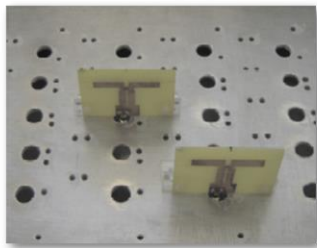
Many solutions have been proposed to mitigate the coupling of antennas in close proximity. Some of the more common solutions include: switched diversity [22], antenna radiation direction [23], connecting impedance elements [24, 25], array configuration [26] and antenna placement [23]. These have all proved effective, but they introduce more complicated feeding networks to the device, increasing the cost to manufacture the device and the time required to optimize the antenna system.



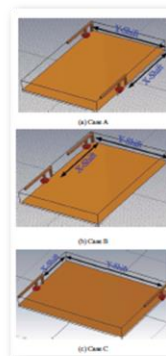
A. Lhailalih *et al*, *Antenna Technology and Applied Electromagnetics & the American Electromagnetics Conference (ANTEM-AMEREM)*, 2010 14th International Symposium on, 2010, pp. 1-4.



S. Zhang *et al*, *IEEE transactions on antennas and propagation*, vol. 61, pp. 3280-3291, 2013.



C. Votis *et al*, *Engineering*, vol. 2, 2010



M. K. T. Al-Nuaimi *et al*, in *Antennas and Propagation Conference (LAPC)*, 2011 Loughborough, 2011, pp. 1-5.

Figure 1.5.2: State-of-the-Art in antenna isolation

Chapter 2: Numerical Tools

2.1 Ansys® HFSS

HFSS is currently the industry standard for simulating 3-D full-wave electromagnetic fields. HFSS offers multiple solvers based on the finite element method, integral equations, and hybrid methods. For each method there is an automated solution process; only the geometry, material properties, and the desired output need to be selected by the user, although much more control of the solution process is provided if the user wishes to use it. HFSS automatically generates the mesh and solves for the electromagnetic fields [27].

Since HFSS requires a 3D geometry, it is not the most efficient solver for devices that can be solved as a 2D or 1D geometry. Also, it only allows materials to be diagonally anisotropic which makes it inconvenient for materials that must be defined by a full material tensor. The geometries are limited to ones that can be drawn in a standard CAD program. Geometries generated with the SVL tool, explained in Section 2.6, cannot currently be imported into HFSS to be modeled.

2.2 4×4 Transfer Matrix Method for Anisotropic Materials (ATMM)

ATMM is a very simple, but powerful method, to solve Maxwell's equations for anisotropic devices that can be solved as 1D geometries. Each 1D geometry is modeled as a structure with an infinite cross section and a finite thickness. Those structures can be referred to as layers. ATMM can account for a large number of layers which are stacked together. Figure 2.2.1 depicts how a 3D problem can be approximated using effective medium approximation, so ATMM can be used to simulate the device [12, 28].

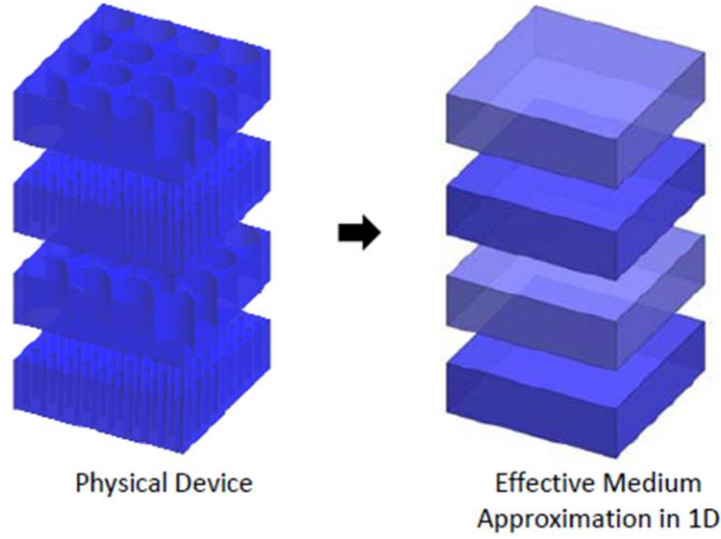


Figure 2.2.1: 3D to 1D homogenization [12]

ATMM can account for angle of incidence, polarization, and dispersion. The thickness of the layers can be any size and ATMM can exploit longitudinal periodicity. ATMM cannot account for diffraction effects, and being a frequency-domain technique it is difficult to incorporate nonlinear effects [12, 28-31].

2.2.1 Formulation

The formulation of the method begins with Maxwell's equations in the following form.

$$\nabla \times \vec{E} = -j\omega[\mu]\vec{H} \quad (2.1)$$

$$\nabla \times \vec{H} = j\omega[\varepsilon]\vec{E} \quad (2.2)$$

The magnetic field and electric field are three orders magnitude different from one another. When performing any time type of computation it is best practice to normalize all values close to one another to minimize computational error [12]. Therefore, the magnetic field is normalized by $\tilde{\vec{H}} = -j\eta_0\vec{H}$.

$$\nabla \times \vec{E} = k_0[\mu]\tilde{\vec{H}} \quad (2.3)$$

$$\nabla \times \vec{H} = k_0 [\varepsilon] \vec{E} \quad (2.4)$$

These vector equations expand to six coupled scalar partial differential equations.

$$\begin{aligned} \frac{\partial E_z}{\partial y} - \frac{\partial E_y}{\partial z} &= k_0 (\mu_{xx} \tilde{H}_x + \mu_{xy} \tilde{H}_y + \mu_{xz} \tilde{H}_z) \\ \frac{\partial E_x}{\partial z} - \frac{\partial E_z}{\partial x} &= k_0 (\mu_{yx} \tilde{H}_x + \mu_{yy} \tilde{H}_y + \mu_{yz} \tilde{H}_z) \\ \frac{\partial E_y}{\partial x} - \frac{\partial E_x}{\partial y} &= k_0 (\mu_{zx} \tilde{H}_x + \mu_{zy} \tilde{H}_y + \mu_{zz} \tilde{H}_z) \end{aligned} \quad (2.5)$$

$$\begin{aligned} \frac{\partial \tilde{H}_z}{\partial y} - \frac{\partial \tilde{H}_y}{\partial z} &= k_0 (\varepsilon_{xx} E_x + \varepsilon_{xy} E_y + \varepsilon_{xz} E_z) \\ \frac{\partial \tilde{H}_x}{\partial z} - \frac{\partial \tilde{H}_z}{\partial x} &= k_0 (\varepsilon_{yx} E_x + \varepsilon_{yy} E_y + \varepsilon_{yz} E_z) \\ \frac{\partial \tilde{H}_y}{\partial x} - \frac{\partial \tilde{H}_x}{\partial y} &= k_0 (\varepsilon_{zx} E_x + \varepsilon_{zy} E_y + \varepsilon_{zz} E_z) \end{aligned} \quad (2.6)$$

Waves propagating in a homogeneous layer are a plane wave, and have the following mathematical form.

$$\begin{aligned} \vec{E}(\vec{r}) &= \vec{E}_0 e^{-j\beta_x x} e^{-j\beta_y y} e^{-j\beta_z z} \\ \vec{H}(\vec{r}) &= \vec{H}_0 e^{-j\beta_x x} e^{-j\beta_y y} e^{-j\beta_z z} \end{aligned} \quad (2.7)$$

Taking the derivatives of these solutions, we see that

$$\frac{\partial}{\partial x} \vec{E}(\vec{r}) = -j\beta_x \vec{E}(\vec{r}) \rightarrow \frac{\partial}{\partial x} = -j\beta_x \quad (2.8)$$

$$\frac{\partial}{\partial y} \vec{E}(\vec{r}) = -j\beta_y \vec{E}(\vec{r}) \rightarrow \frac{\partial}{\partial y} = -j\beta_y \quad (2.9)$$

Maxwell's equations then become

$$\begin{aligned}
-j\beta_y E_z - \frac{dE_y}{dz} &= k_0 (\mu_{xx} \tilde{H}_x + \mu_{xy} \tilde{H}_y + \mu_{xz} \tilde{H}_z) \\
\frac{dE_x}{dz} + j\beta_x E_z &= k_0 (\mu_{yx} \tilde{H}_x + \mu_{yy} \tilde{H}_y + \mu_{yz} \tilde{H}_z) \\
-j\beta_x E_y + j\beta_y E_x &= k_0 (\mu_{zx} \tilde{H}_x + \mu_{zy} \tilde{H}_y + \mu_{zz} \tilde{H}_z)
\end{aligned} \tag{2.10}$$

$$\begin{aligned}
-j\beta_y \tilde{H}_z - \frac{d\tilde{H}_y}{dz} &= k_0 (\varepsilon_{xx} E_x + \varepsilon_{xy} E_y + \varepsilon_{xz} E_z) \\
\frac{d\tilde{H}_x}{dz} + j\beta_x \tilde{H}_z &= k_0 (\varepsilon_{yx} E_x + \varepsilon_{yy} E_y + \varepsilon_{yz} E_z) \\
-j\beta_x \tilde{H}_y + j\beta_y \tilde{H}_x &= k_0 (\varepsilon_{zx} E_x + \varepsilon_{zy} E_y + \varepsilon_{zz} E_z)
\end{aligned} \tag{2.11}$$

Normalizing Maxwell's equations according to

$$\tilde{z} = k_0 z, \quad \hat{\beta}_x = \frac{\beta_x}{k_0}, \quad \hat{\beta}_y = \frac{\beta_y}{k_0} \tag{2.12}$$

$$\begin{aligned}
-j\hat{\beta}_y E_z - \frac{dE_y}{d\tilde{z}} &= (\mu_{xx} \tilde{H}_x + \mu_{xy} \tilde{H}_y + \mu_{xz} \tilde{H}_z) \\
\frac{dE_x}{d\tilde{z}} + j\hat{\beta}_x E_z &= (\mu_{yx} \tilde{H}_x + \mu_{yy} \tilde{H}_y + \mu_{yz} \tilde{H}_z) \\
-j\hat{\beta}_x E_y + j\hat{\beta}_y E_x &= (\mu_{zx} \tilde{H}_x + \mu_{zy} \tilde{H}_y + \mu_{zz} \tilde{H}_z)
\end{aligned} \tag{2.13}$$

$$\begin{aligned}
-j\hat{\beta}_y \tilde{H}_z - \frac{d\tilde{H}_y}{d\tilde{z}} &= k_0 (\varepsilon_{xx} E_x + \varepsilon_{xy} E_y + \varepsilon_{xz} E_z) \\
\frac{d\tilde{H}_x}{d\tilde{z}} + j\hat{\beta}_x \tilde{H}_z &= k_0 (\varepsilon_{yx} E_x + \varepsilon_{yy} E_y + \varepsilon_{yz} E_z) \\
-j\hat{\beta}_x \tilde{H}_y + j\hat{\beta}_y \tilde{H}_x &= k_0 (\varepsilon_{zx} E_x + \varepsilon_{zy} E_y + \varepsilon_{zz} E_z)
\end{aligned} \tag{2.14}$$

Solving equations (2.13) and (2.14) for the longitudinal components

$$\begin{aligned}
-j\hat{\beta}_y E_z - \frac{dE_y}{d\tilde{z}} &= (\mu_{xx} \tilde{H}_x + \mu_{xy} \tilde{H}_y + \mu_{xz} \tilde{H}_z) \\
\frac{dE_x}{d\tilde{z}} + j\hat{\beta}_x E_z &= (\mu_{yx} \tilde{H}_x + \mu_{yy} \tilde{H}_y + \mu_{yz} \tilde{H}_z) \\
-j\hat{\beta}_x E_y + j\hat{\beta}_y E_x &= (\mu_{zx} \tilde{H}_x + \mu_{zy} \tilde{H}_y + \mu_{zz} \tilde{H}_z) \rightarrow \tilde{H}_z = \frac{j\hat{\beta}_y E_x}{\mu_{zz}} - \frac{j\hat{\beta}_x E_y}{\mu_{zz}} + \frac{\mu_{zx} \tilde{H}_x}{\mu_{zz}} - \frac{\mu_{zy} \tilde{H}_y}{\mu_{zz}}
\end{aligned} \tag{2.15}$$

$$\begin{aligned}
-j\hat{\beta}_y\tilde{H}_z - \frac{d\tilde{H}_y}{d\tilde{z}} &= (\varepsilon_{xx}E_x + \varepsilon_{xy}E_y + \varepsilon_{xz}E_z) \\
\frac{d\tilde{H}_x}{d\tilde{z}} + j\hat{\beta}_x\tilde{H}_z &= (\varepsilon_{yx}E_x + \varepsilon_{yy}E_y + \varepsilon_{yz}E_z) \\
-j\hat{\beta}_x\tilde{H}_y + j\hat{\beta}_y\tilde{H}_x &= (\varepsilon_{zx}E_x + \varepsilon_{zy}E_y + \varepsilon_{zz}E_z) \rightarrow E_z = \frac{j\hat{\beta}_y\tilde{H}_x}{\varepsilon_{zz}} - \frac{j\hat{\beta}_x\tilde{H}_y}{\varepsilon_{zz}} - \frac{\varepsilon_{zx}E_x}{\varepsilon_{zz}} - \frac{\varepsilon_{zy}E_y}{\varepsilon_{zz}}
\end{aligned} \tag{2.16}$$

Eliminating the longitudinal components by substitution

$$\begin{aligned}
\frac{\hat{\beta}_y^2}{\varepsilon_{zz}}\tilde{H}_x - \frac{\hat{\beta}_y\hat{\beta}_x}{\varepsilon_{zz}}\tilde{H}_y + \frac{j\hat{\beta}_y\varepsilon_{zx}}{\varepsilon_{zz}}E_x + \frac{j\hat{\beta}_y\varepsilon_{zy}}{\varepsilon_{zz}}E_y - \frac{d\tilde{H}_y}{d\tilde{z}} &= \mu_{xx}\tilde{H}_x + \mu_{xy}\tilde{H}_y + \frac{\mu_{xz}j\hat{\beta}_y}{\mu_{zz}}E_x - \frac{\mu_{yz}j\hat{\beta}_x}{\mu_{zz}}E_y + \frac{\mu_{xz}\mu_{zx}}{\mu_{zz}}\tilde{H}_x - \frac{\mu_{xz}\mu_{zy}}{\mu_{zz}}\tilde{H}_y \\
\frac{d\tilde{H}_x}{d\tilde{z}} - \frac{\hat{\beta}_x\hat{\beta}_y}{\varepsilon_{zz}}\tilde{H}_x + \frac{\hat{\beta}_x^2}{\varepsilon_{zz}}\tilde{H}_y - \frac{j\hat{\beta}_x\varepsilon_{zx}}{\varepsilon_{zz}}E_x - \frac{j\hat{\beta}_x\varepsilon_{zy}}{\varepsilon_{zz}}E_y &= \mu_{yx}\tilde{H}_x + \mu_{yy}\tilde{H}_y + \frac{\mu_{yz}j\hat{\beta}_y}{\mu_{zz}}E_x - \frac{\mu_{yx}j\hat{\beta}_x}{\mu_{zz}}E_y - \frac{\mu_{yz}\mu_{zx}}{\mu_{zz}}\tilde{H}_x - \frac{\mu_{yz}\mu_{zy}}{\mu_{zz}}\tilde{H}_y
\end{aligned} \tag{2.17}$$

$$\begin{aligned}
\frac{\hat{\beta}_x^2}{\mu_{zz}}E_x - \frac{\hat{\beta}_x\hat{\beta}_y}{\mu_{zz}}E_y + \frac{j\hat{\beta}_y\mu_{zx}}{\mu_{zz}}\tilde{H}_x + \frac{j\hat{\beta}_y\mu_{zy}}{\mu_{zz}}\tilde{H}_y - \frac{d\tilde{H}_y}{d\tilde{z}} &= \varepsilon_{xx}E_x + \varepsilon_{xy}E_y + \frac{\varepsilon_{xz}j\hat{\beta}_y}{\varepsilon_{zz}}\tilde{H}_x - \frac{\varepsilon_{yz}j\hat{\beta}_x}{\varepsilon_{zz}}\tilde{H}_y - \frac{\varepsilon_{xz}\varepsilon_{zx}}{\varepsilon_{zz}}E_x - \frac{\varepsilon_{xz}\varepsilon_{zy}}{\varepsilon_{zz}}E_y \\
\frac{d\tilde{H}_x}{d\tilde{z}} - \frac{\hat{\beta}_x\hat{\beta}_y}{\mu_{zz}}E_x + \frac{\hat{\beta}_x^2}{\mu_{zz}}E_y - \frac{j\hat{\beta}_x\mu_{zx}}{\mu_{zz}}\tilde{H}_x - \frac{j\hat{\beta}_x\mu_{zy}}{\mu_{zz}}\tilde{H}_y &= \varepsilon_{yx}E_x + \varepsilon_{yy}E_y + \frac{\varepsilon_{yz}j\hat{\beta}_y}{\varepsilon_{zz}}\tilde{H}_x - \frac{\varepsilon_{yx}j\hat{\beta}_x}{\varepsilon_{zz}}\tilde{H}_y - \frac{\varepsilon_{yz}\varepsilon_{zx}}{\varepsilon_{zz}}E_x - \frac{\varepsilon_{yz}\varepsilon_{zy}}{\varepsilon_{zz}}E_y
\end{aligned} \tag{2.18}$$

Rearranging equations(2.17) and (2.18)

$$\begin{aligned}
\frac{dE_x}{d\tilde{z}} &= j\left(\frac{\mu_{yz}\hat{\beta}_y}{\mu_{zz}} + \frac{\hat{\beta}_x\varepsilon_{zx}}{\varepsilon_{zz}}\right)E_x + j\hat{\beta}_x\left(\frac{\varepsilon_{zy}}{\varepsilon_{zz}} - \frac{\mu_{yz}}{\mu_{zz}}\right)E_y + \left(\mu_{yx} - \frac{\mu_{yz}\mu_{zx}}{\mu_{zz}} + \frac{\hat{\beta}_y\hat{\beta}_y}{\varepsilon_{zz}}\right)\tilde{H}_x + \left(\mu_{yy} - \frac{\mu_{yz}\mu_{zy}}{\mu_{zz}} - \frac{\hat{\beta}_x^2}{\varepsilon_{zz}}\right)\tilde{H}_y \\
\frac{dE_y}{d\tilde{z}} &= j\hat{\beta}_y\left(\frac{\varepsilon_{zx}}{\varepsilon_{zz}} - \frac{\mu_{xz}}{\mu_{zz}}\right)E_x + j\left(\frac{\mu_{xz}\hat{\beta}_x}{\mu_{zz}} + \frac{\hat{\beta}_y\varepsilon_{zy}}{\varepsilon_{zz}}\right)E_y + \left(\frac{\mu_{xz}\mu_{zx}}{\mu_{zz}} - \mu_{xx} + \frac{\hat{\beta}_y^2}{\varepsilon_{zz}}\right)\tilde{H}_x + \left(\frac{\mu_{xz}\mu_{zy}}{\mu_{zz}} - \mu_{xy} - \frac{\hat{\beta}_y\hat{\beta}_x}{\varepsilon_{zz}}\right)\tilde{H}_y
\end{aligned} \tag{2.19}$$

$$\begin{aligned}
\frac{d\tilde{H}_x}{d\tilde{z}} &= \left(\varepsilon_{yx} - \frac{\varepsilon_{yz}\varepsilon_{zx}}{\varepsilon_{zz}} + \frac{\hat{\beta}_x\hat{\beta}_y}{\mu_{zz}}\right)E_x + \left(\varepsilon_{yy} - \frac{\varepsilon_{yz}\varepsilon_{zy}}{\varepsilon_{zz}} - \frac{\hat{\beta}_x^2}{\mu_{zz}}\right)E_y + j\left(\frac{\varepsilon_{yz}\hat{\beta}_y}{\varepsilon_{zz}} + \frac{\hat{\beta}_x\mu_{zx}}{\mu_{zz}}\right)\tilde{H}_x + j\hat{\beta}_x\left(\frac{\mu_{zy}}{\mu_{zz}} - \frac{\varepsilon_{yx}}{\varepsilon_{zz}}\right)\tilde{H}_y \\
\frac{d\tilde{H}_y}{d\tilde{z}} &= \left(\frac{\varepsilon_{xz}\varepsilon_{zx}}{\varepsilon_{zz}} - \varepsilon_{xx} + \frac{\hat{\beta}_y^2}{\mu_{zz}}\right)E_x + \left(\frac{\varepsilon_{xz}\varepsilon_{zy}}{\varepsilon_{zz}} - \varepsilon_{xy} - \frac{\hat{\beta}_y\hat{\beta}_x}{\mu_{zz}}\right)E_y + j\hat{\beta}_y\left(\frac{\mu_{zx}}{\mu_{zz}} - \frac{\varepsilon_{xz}}{\varepsilon_{zz}}\right)\tilde{H}_x + \tilde{H}_y
\end{aligned} \tag{2.20}$$

Writing equations (2.19) and (2.20) in matrix form

$$\frac{d}{dz} \begin{bmatrix} E_x \\ E_y \\ \tilde{H}_x \\ \tilde{H}_y \end{bmatrix} = \begin{bmatrix} j \left(\frac{\mu_{yz} \hat{\beta}_y}{\mu_{zz}} + \frac{\hat{\beta}_x \varepsilon_{zx}}{\varepsilon_{zz}} \right) & j \hat{\beta}_x \left(\frac{\varepsilon_{zy}}{\varepsilon_{zz}} - \frac{\mu_{yz}}{\mu_{zz}} \right) & \left(\mu_{yx} - \frac{\mu_{yz} \mu_{zx}}{\mu_{zz}} + \frac{\hat{\beta}_x \hat{\beta}_y}{\varepsilon_{zz}} \right) & \left(\mu_{yy} - \frac{\mu_{yz} \mu_{zy}}{\mu_{zz}} - \frac{\hat{\beta}_x^2}{\varepsilon_{zz}} \right) \\ j \hat{\beta}_y \left(\frac{\varepsilon_{zx}}{\varepsilon_{zz}} - \frac{\mu_{xz}}{\mu_{zz}} \right) & j \left(\frac{\mu_{xz} \hat{\beta}_x}{\mu_{zz}} + \frac{\hat{\beta}_y \varepsilon_{zy}}{\varepsilon_{zz}} \right) & \left(\frac{\mu_{xz} \mu_{zx}}{\mu_{zz}} - \mu_{xx} + \frac{\hat{\beta}_y^2}{\varepsilon_{zz}} \right) & \left(\frac{\mu_{xz} \mu_{zy}}{\mu_{zz}} - \mu_{xy} - \frac{\hat{\beta}_y \hat{\beta}_x}{\varepsilon_{zz}} \right) \\ \left(\varepsilon_{yx} - \frac{\varepsilon_{yz} \varepsilon_{zx}}{\varepsilon_{zz}} + \frac{\hat{\beta}_x \hat{\beta}_y}{\mu_{zz}} \right) & \left(\varepsilon_{yy} - \frac{\varepsilon_{yz} \varepsilon_{zy}}{\varepsilon_{zz}} - \frac{\hat{\beta}_x^2}{\mu_{zz}} \right) & j \left(\frac{\varepsilon_{yz} \hat{\beta}_y}{\varepsilon_{zz}} + \frac{\hat{\beta}_x \mu_{zx}}{\mu_{zz}} \right) & j \hat{\beta}_x \left(\frac{\mu_{zy}}{\mu_{zz}} - \frac{\varepsilon_{yz}}{\varepsilon_{zz}} \right) \\ \left(\frac{\varepsilon_{xz} \varepsilon_{zx}}{\varepsilon_{zz}} - \varepsilon_{xx} + \frac{\hat{\beta}_y^2}{\mu_{zz}} \right) & \left(\frac{\varepsilon_{xz} \varepsilon_{zy}}{\varepsilon_{zz}} - \varepsilon_{xy} - \frac{\hat{\beta}_y \hat{\beta}_x}{\mu_{zz}} \right) & j \hat{\beta}_y \left(\frac{\mu_{zx}}{\mu_{zz}} - \frac{\varepsilon_{xz}}{\varepsilon_{zz}} \right) & j \left(\frac{\varepsilon_{xz} \hat{\beta}_x}{\varepsilon_{zz}} + \frac{\hat{\beta}_y \mu_{zy}}{\mu_{zz}} \right) \end{bmatrix} \begin{bmatrix} E_x \\ E_y \\ \tilde{H}_x \\ \tilde{H}_y \end{bmatrix} \quad (2.21)$$

Maxwell's equations can now be written as a single matrix differential equation

$$\frac{d\psi}{dz} - \mathbf{\Omega}\psi = 0, \quad (2.22)$$

where

$$\psi(\tilde{z}) = \begin{bmatrix} E_x(\tilde{z}) \\ E_y(\tilde{z}) \\ \tilde{H}_x(\tilde{z}) \\ \tilde{H}_y(\tilde{z}) \end{bmatrix}$$

$$\mathbf{\Omega} = \begin{bmatrix} j \left(\frac{\mu_{yz} \hat{\beta}_y}{\mu_{zz}} + \frac{\hat{\beta}_x \varepsilon_{zx}}{\varepsilon_{zz}} \right) & j \hat{\beta}_x \left(\frac{\varepsilon_{zy}}{\varepsilon_{zz}} - \frac{\mu_{yz}}{\mu_{zz}} \right) & \left(\mu_{yx} - \frac{\mu_{yz} \mu_{zx}}{\mu_{zz}} + \frac{\hat{\beta}_x \hat{\beta}_y}{\varepsilon_{zz}} \right) & \left(\mu_{yy} - \frac{\mu_{yz} \mu_{zy}}{\mu_{zz}} - \frac{\hat{\beta}_x^2}{\varepsilon_{zz}} \right) \\ j \hat{\beta}_y \left(\frac{\varepsilon_{zx}}{\varepsilon_{zz}} - \frac{\mu_{xz}}{\mu_{zz}} \right) & j \left(\frac{\mu_{xz} \hat{\beta}_x}{\mu_{zz}} + \frac{\hat{\beta}_y \varepsilon_{zy}}{\varepsilon_{zz}} \right) & \left(\frac{\mu_{xz} \mu_{zx}}{\mu_{zz}} - \mu_{xx} + \frac{\hat{\beta}_y^2}{\varepsilon_{zz}} \right) & \left(\frac{\mu_{xz} \mu_{zy}}{\mu_{zz}} - \mu_{xy} - \frac{\hat{\beta}_y \hat{\beta}_x}{\varepsilon_{zz}} \right) \\ \left(\varepsilon_{yx} - \frac{\varepsilon_{yz} \varepsilon_{zx}}{\varepsilon_{zz}} + \frac{\hat{\beta}_x \hat{\beta}_y}{\mu_{zz}} \right) & \left(\varepsilon_{yy} - \frac{\varepsilon_{yz} \varepsilon_{zy}}{\varepsilon_{zz}} - \frac{\hat{\beta}_x^2}{\mu_{zz}} \right) & j \left(\frac{\varepsilon_{yz} \hat{\beta}_y}{\varepsilon_{zz}} + \frac{\hat{\beta}_x \mu_{zx}}{\mu_{zz}} \right) & j \hat{\beta}_x \left(\frac{\mu_{zy}}{\mu_{zz}} - \frac{\varepsilon_{yz}}{\varepsilon_{zz}} \right) \\ \left(\frac{\varepsilon_{xz} \varepsilon_{zx}}{\varepsilon_{zz}} - \varepsilon_{xx} + \frac{\hat{\beta}_y^2}{\mu_{zz}} \right) & \left(\frac{\varepsilon_{xz} \varepsilon_{zy}}{\varepsilon_{zz}} - \varepsilon_{xy} - \frac{\hat{\beta}_y \hat{\beta}_x}{\mu_{zz}} \right) & j \hat{\beta}_y \left(\frac{\mu_{zx}}{\mu_{zz}} - \frac{\varepsilon_{xz}}{\varepsilon_{zz}} \right) & j \left(\frac{\varepsilon_{xz} \hat{\beta}_x}{\varepsilon_{zz}} + \frac{\hat{\beta}_y \mu_{zy}}{\mu_{zz}} \right) \end{bmatrix} \quad (2.23)$$

The general solution to equation (2.22) is

$$\psi(\tilde{z}) = e^{-\mathbf{\Omega}\tilde{z}} \psi(0) \quad (2.24)$$

Since $\mathbf{\Omega}$ is a matrix, applying the exponential function is not straight forward; this identity can be used [32]:

$$f(\mathbf{A}) = \mathbf{W} \cdot f(\boldsymbol{\lambda}) \cdot \mathbf{W}^{-1} \quad (2.25)$$

Where \mathbf{A} is a matrix, \mathbf{W} is the Eigen-vector matrix of \mathbf{A} , $\boldsymbol{\lambda}$ is the Eigen-value matrix of \mathbf{A} , and $f()$ is the function performed on \mathbf{A} . Therefore

$$e^{-\Omega \tilde{z}} = \mathbf{W} e^{-\lambda \tilde{z}} \mathbf{W}^{-1} \quad (2.26)$$

Equation (2.24) becomes

$$\boldsymbol{\psi}(\tilde{z}) = \mathbf{W} e^{-\lambda \tilde{z}} \mathbf{W}^{-1} \boldsymbol{\psi}(0) \quad (2.27)$$

Equation (2.27) can be rewritten as

$$\boldsymbol{\psi}(\tilde{z}) = \mathbf{W} e^{-\lambda \tilde{z}} \mathbf{c}; \text{ where } \mathbf{c} = \mathbf{W}^{-1} \boldsymbol{\psi}(0) \quad (2.28)$$

Due to reflections at interfaces, there will also be backward traveling waves in each layer. These waves can also have wave vectors that are real, imaginary or complex. ATMM treats all waves as if they are forward propagating. Decaying fields associated with backwards waves become exponentially growing fields and quickly become numerically unstable. This can be fixed by distinguishing between forward and backward waves. This can be done by calculating the Poynting vector associated with each eigen-mode.

$$\vec{\phi} = \vec{E} \times \vec{H} \quad (2.29)$$

The waves are propagating the z -direction, so the Poynting vector only needs to be calculated in the z -direction.

$$\phi_z = E_x \tilde{H}_y - E_y \tilde{H}_x \quad (2.30)$$

The magnetic field is normalized so it must be unnormalized.

$$\phi_z = E_x \left(j \frac{\tilde{H}_y}{\eta_0} \right) - E_y \left(j \frac{\tilde{H}_x}{\eta_0} \right) \quad (2.31)$$

$$\phi_z = \frac{j}{\eta_0} (E_x \tilde{H}_y - E_y \tilde{H}_x) \quad (2.32)$$

Now, the forward and backward waves can be distinguished by looking at the sign of the Poynting vector calculated in Eq. (2.32). Now that we know which eigen-modes correspond to forward and backward propagating waves, we can rearrange the eigen-vector and eigen-value matrices to group them together.

After distinguishing between forward and backward propagating waves, eq. (2.28) can be rewritten as

$$\Psi(\tilde{z}) = \begin{bmatrix} \mathbf{W}_E^+ & \mathbf{W}_E^- \\ \mathbf{W}_H^+ & \mathbf{W}_H^- \end{bmatrix} \begin{bmatrix} e^{-\lambda \tilde{z}} & \mathbf{0} \\ \mathbf{0} & e^{\lambda \tilde{z}} \end{bmatrix} \begin{bmatrix} \mathbf{c}^+ \\ \mathbf{c}^- \end{bmatrix} \quad (2.33)$$

Since the propagating waves obey reciprocity, Eq. (2.33) can be rewritten in terms of just the forward propagating terms

$$\Psi(\tilde{z}) = \begin{bmatrix} \mathbf{W} & \mathbf{W} \\ -\mathbf{V} & \mathbf{V} \end{bmatrix} \begin{bmatrix} e^{-\lambda \tilde{z}} & \mathbf{0} \\ \mathbf{0} & e^{\lambda \tilde{z}} \end{bmatrix} \begin{bmatrix} \mathbf{c}^+ \\ \mathbf{c}^- \end{bmatrix} \quad (2.34)$$

where

$$\begin{aligned} \mathbf{W} &= \mathbf{W}_E^+ \\ \mathbf{V} &= \mathbf{W}_H^+ \end{aligned} \quad (2.35)$$

Instead of numerically calculating \mathbf{W} , \mathbf{V} , and λ , it is possible to calculate them analytically by using the dispersion relation. For isotropic materials with dielectric constant ϵ_c , the solution is

$$\kappa = \sqrt{\epsilon_c - \beta^2} \quad (2.36)$$

$$\mathbf{W} = \begin{bmatrix} 1 & 0 \\ 0 & \epsilon_c \end{bmatrix} \quad (2.37)$$

$$\mathbf{V} = \begin{bmatrix} 0 & -\kappa \\ \kappa & 0 \end{bmatrix} \quad (2.38)$$

$$\lambda = \begin{bmatrix} \kappa & 0 \\ 0 & \kappa \end{bmatrix} \quad (2.39)$$

For uniaxial materials, the solution is

$$\kappa_o = -\sqrt{n_o^2 - \beta^2} \quad (2.40)$$

$$\kappa_e = -\sqrt{n_o^2 - \beta^2 \left(n_e^2 \cos^2 \theta + n_o^2 \sin^2 \theta / n_o^2 \right)} \quad (2.41)$$

$$\mathbf{W} = \begin{bmatrix} \kappa_o \cos \theta & -\varepsilon_o \sin \theta \\ \varepsilon_o \sin \theta & \kappa_e \varepsilon_o \cos \theta \end{bmatrix} \quad (2.42)$$

$$\mathbf{V} = \begin{bmatrix} -\kappa_o \sin \theta & (\beta^2 - \varepsilon_o) \cos \theta \\ \kappa_o \cos \theta & -\kappa_e \varepsilon_o \sin \theta \end{bmatrix} \quad (2.43)$$

$$\boldsymbol{\lambda} = \begin{bmatrix} \kappa_o & 0 \\ 0 & \kappa_e \end{bmatrix} \quad (2.44)$$

In Eqs. (2.40) - (2.44), θ is the rotation of the optical axis away from the longitudinal direction. The subscripts o and e indicate the ordinary and extraordinary modes respectively. The geometry of the fields inside a layer is illustrated in Figure 2.2.2.

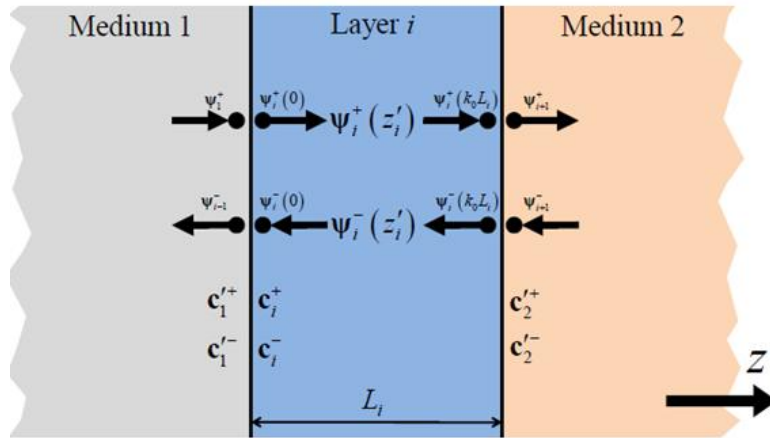


Figure 2.2.2: Geometry of an embedded layer [12]

The field inside the i^{th} layer is as follows.

$$\Psi(\tilde{z}) = \begin{bmatrix} E_{x,i}(\tilde{z}) \\ E_{y,i}(\tilde{z}) \\ \tilde{H}_{x,i}(\tilde{z}) \\ \tilde{H}_{y,i}(\tilde{z}) \end{bmatrix} = \begin{bmatrix} \mathbf{W}_i & \mathbf{W}_i \\ -\mathbf{V}_i & \mathbf{V}_i \end{bmatrix} \begin{bmatrix} e^{-\lambda_i \tilde{z}} & 0 \\ 0 & e^{\lambda_i \tilde{z}} \end{bmatrix} \begin{bmatrix} \mathbf{c}_i^+ \\ \mathbf{c}_i^- \end{bmatrix} \quad (2.45)$$

The boundary conditions at the first interface are as follows.

$$\begin{aligned} \Psi_1 &= \Psi_i(0) \\ \begin{bmatrix} \mathbf{W}_1 & \mathbf{W}_1 \\ \mathbf{V}_1 & -\mathbf{V}_1 \end{bmatrix} \begin{bmatrix} \mathbf{c}_1'^+ \\ \mathbf{c}_1'^- \end{bmatrix} &= \begin{bmatrix} \mathbf{W}_i & \mathbf{W}_i \\ -\mathbf{V}_i & \mathbf{V}_i \end{bmatrix} \begin{bmatrix} \mathbf{c}_i^+ \\ \mathbf{c}_i^- \end{bmatrix} \end{aligned} \quad (2.46)$$

The boundary conditions at the second interface are as follows.

$$\begin{aligned} \Psi_i(k_0 L_i) &= \Psi_2 \\ \begin{bmatrix} \mathbf{W}_i & \mathbf{W}_i \\ -\mathbf{V}_i & \mathbf{V}_i \end{bmatrix} \begin{bmatrix} e^{-\lambda_i k_0 L_i} & \mathbf{0} \\ \mathbf{0} & e^{\lambda_i k_0 L_i} \end{bmatrix} \begin{bmatrix} \mathbf{c}_i^+ \\ \mathbf{c}_i^- \end{bmatrix} &= \begin{bmatrix} \mathbf{W}_2 & \mathbf{W}_2 \\ -\mathbf{V}_2 & \mathbf{V}_2 \end{bmatrix} \begin{bmatrix} \mathbf{c}_2'^+ \\ \mathbf{c}_2'^- \end{bmatrix} \end{aligned} \quad (2.47)$$

The scattering matrix \mathbf{S}_i of the i^{th} layer is defined as

$$\begin{bmatrix} \mathbf{c}_1'^- \\ \mathbf{c}_2'^+ \end{bmatrix} = \mathbf{S}_i \begin{bmatrix} \mathbf{c}_1'^+ \\ \mathbf{c}_2'^- \end{bmatrix} \quad \mathbf{S}_i = \begin{bmatrix} \mathbf{S}_{11}^i & \mathbf{S}_{12}^i \\ \mathbf{S}_{21}^i & \mathbf{S}_{22}^i \end{bmatrix} \quad (2.48)$$

After some algebra, which is shown in appendix A1, the components of the transfer matrix are computed as

$$\begin{aligned} \mathbf{A}_{i,j} &= \mathbf{W}_i^{-1} \mathbf{W}_j + \mathbf{V}_i^{-1} \mathbf{V}_j \\ \mathbf{B}_{i,j} &= \mathbf{W}_i^{-1} \mathbf{W}_j - \mathbf{V}_i^{-1} \mathbf{V}_j \\ \mathbf{X}_i &= e^{-\lambda_i k_0 L_i} \end{aligned} \quad (2.49)$$

$$\begin{aligned} \mathbf{s}_{11}^i &= (\mathbf{A}_{i,i-1} - \mathbf{X}_i \mathbf{B}_{i,i+1} \mathbf{A}_{i,i+1}^{-1} \mathbf{X}_i \mathbf{B}_{i,i-1})^{-1} (\mathbf{X}_i \mathbf{B}_{i,i+1} \mathbf{A}_{i,i+1}^{-1} \mathbf{X}_i \mathbf{A}_{i,i-1} - \mathbf{B}_{i,i-1}) \\ \mathbf{s}_{12}^i &= (\mathbf{A}_{i,i-1} - \mathbf{X}_i \mathbf{B}_{i,i+1} \mathbf{A}_{i,i+1}^{-1} \mathbf{X}_i \mathbf{B}_{i,i-1})^{-1} \mathbf{X}_i (\mathbf{A}_{i,i+1} - \mathbf{B}_{i,i-1} \mathbf{A}_{i,i+1}^{-1} \mathbf{B}_{i,i+1}) \\ \mathbf{s}_{21}^i &= (\mathbf{A}_{i,i-1} - \mathbf{X}_i \mathbf{B}_{i,i+1} \mathbf{A}_{i,i+1}^{-1} \mathbf{X}_i \mathbf{B}_{i,i-1})^{-1} \mathbf{X}_i (\mathbf{A}_{i,i+1} - \mathbf{B}_{i,i-1} \mathbf{A}_{i,i+1}^{-1} \mathbf{B}_{i,i+1}) \\ \mathbf{s}_{22}^i &= (\mathbf{A}_{i,i-1} - \mathbf{X}_i \mathbf{B}_{i,i+1} \mathbf{A}_{i,i+1}^{-1} \mathbf{X}_i \mathbf{B}_{i,i-1})^{-1} (\mathbf{X}_i \mathbf{B}_{i,i+1} \mathbf{A}_{i,i+1}^{-1} \mathbf{X}_i \mathbf{A}_{i,i-1} - \mathbf{B}_{i,i-1}) \end{aligned} \quad (2.50)$$

The transfer matrix method consists of working through the device one layer at a time and calculating an overall (global) scattering matrix.

$$\mathbf{S}_{\text{global}} = \mathbf{S}_5 \otimes \mathbf{S}_4 \otimes \mathbf{S}_3 \otimes \mathbf{S}_2 \otimes \mathbf{S}_1 \quad (2.51)$$

Here the \otimes operator denotes the Redheffer star product [33]. The definition of the Redheffer star product is as follows.

$$\mathbf{S} = \mathbf{S}_b \otimes \mathbf{S}_a \quad \mathbf{S}_b = \begin{bmatrix} \mathbf{b}_{11} & \mathbf{b}_{12} \\ \mathbf{b}_{21} & \mathbf{b}_{22} \end{bmatrix} \quad \mathbf{S}_a = \begin{bmatrix} \mathbf{a}_{11} & \mathbf{a}_{12} \\ \mathbf{a}_{21} & \mathbf{a}_{22} \end{bmatrix} \quad (2.52)$$

The combined scattering matrix is then

$$\begin{aligned} \mathbf{S} &= \begin{bmatrix} \mathbf{S}_{11} & \mathbf{S}_{12} \\ \mathbf{S}_{21} & \mathbf{S}_{22} \end{bmatrix} \\ \mathbf{S}_{11} &= \mathbf{a}_{11} + \mathbf{a}_{12}(\mathbf{I} - \mathbf{b}_{11}\mathbf{a}_{22})^{-1}\mathbf{b}_{11}\mathbf{a}_{21} \\ \mathbf{S}_{12} &= \mathbf{a}_{12}(\mathbf{I} - \mathbf{b}_{11}\mathbf{a}_{22})^{-1}\mathbf{b}_{12} \\ \mathbf{S}_{21} &= \mathbf{b}_{21}(\mathbf{I} - \mathbf{a}_{22}\mathbf{b}_{11})^{-1}\mathbf{a}_{21} \\ \mathbf{S}_{22} &= \mathbf{b}_{11} + \mathbf{b}_{21}(\mathbf{I} - \mathbf{a}_{22}\mathbf{b}_{11})^{-1}\mathbf{a}_{22}\mathbf{b}_{12} \end{aligned} \quad (2.53)$$

The final scattering matrix is

$$\begin{bmatrix} \mathbf{c}'_1 \\ \mathbf{c}'_2 \end{bmatrix} = \begin{bmatrix} \mathbf{S}_{11} & \mathbf{S}_{12} \\ \mathbf{S}_{21} & \mathbf{S}_{22} \end{bmatrix} \begin{bmatrix} \mathbf{c}'_1 \\ \mathbf{c}'_2 \end{bmatrix} \quad (2.54)$$

2.3 2D Plane Wave Expansion Method

The PWEM is extremely efficient for calculating the band diagrams for periodic structures. PWEM works best with unit cells that are on the order of a wavelength and have a low to moderate refractive index contrast [34-39].

2.3.1 Formulation

The method begins with Maxwell's equations in the following form

$$\nabla \times \vec{E} = -j\omega\mu_0\mu_r\vec{H} \quad (2.55)$$

$$\nabla \times \vec{H} = j\omega\epsilon_0\epsilon_r\vec{E}a \quad (2.56)$$

After normalizing the magnetic field according to $\vec{\tilde{H}} = -j\eta_0\vec{H}$, Maxwell's equations become

$$\nabla \times \vec{E} = k_0 \mu_r \vec{H} \quad (2.57)$$

$$\nabla \times \vec{H} = k_0 \epsilon_r \vec{E} \quad (2.58)$$

These vector equations expand into six coupled scalar partial differential equations.

$$\begin{aligned} \frac{\partial E_z}{\partial y} - \frac{\partial E_y}{\partial z} &= k_0 \mu_r \tilde{H}_x \\ \frac{\partial E_x}{\partial z} - \frac{\partial E_z}{\partial x} &= k_0 \mu_r \tilde{H}_y \\ \frac{\partial E_y}{\partial x} - \frac{\partial E_x}{\partial y} &= k_0 \mu_r \tilde{H}_z \end{aligned} \quad (2.59)$$

$$\begin{aligned} \frac{\partial \tilde{H}_z}{\partial y} - \frac{\partial \tilde{H}_y}{\partial z} &= k_0 \epsilon_r E_x \\ \frac{\partial \tilde{H}_x}{\partial z} - \frac{\partial \tilde{H}_z}{\partial x} &= k_0 \epsilon_r E_y \\ \frac{\partial \tilde{H}_y}{\partial x} - \frac{\partial \tilde{H}_x}{\partial y} &= k_0 \epsilon_r E_z \end{aligned} \quad (2.60)$$

These equations can be Fourier transformed, shown in detail in [40], which yields:

$$\begin{aligned} k_{y,pqr} S_{z,pqr} - k_{z,pqr} S_{y,pqr} &= j k_0 \mu_{pqr} * U_{x,pqr} \\ k_{z,pqr} S_{x,pqr} - k_{x,pqr} S_{z,pqr} &= j k_0 \mu_{pqr} * U_{y,pqr} \\ k_{x,pqr} S_{y,pqr} - k_{y,pqr} S_{x,pqr} &= j k_0 \mu_{pqr} * U_{z,pqr} \end{aligned} \quad (2.61)$$

$$\begin{aligned} k_{y,pqr} U_{z,pqr} - k_{z,pqr} U_{y,pqr} &= j k_0 \epsilon_{pqr} * S_{x,pqr} \\ k_{z,pqr} U_{x,pqr} - k_{x,pqr} U_{z,pqr} &= j k_0 \epsilon_{pqr} * S_{y,pqr} \\ k_{x,pqr} U_{y,pqr} - k_{y,pqr} U_{x,pqr} &= j k_0 \epsilon_{pqr} * S_{z,pqr} \end{aligned} \quad (2.62)$$

Each of these equations is written once for every spatial harmonic (Fourier term) retained in the expansion. This large set of equations can be written in matrix form as

$$\mathbf{K}_y \mathbf{s}_z - \mathbf{K}_z \mathbf{s}_y = j k_0 \boldsymbol{\mu}_r \mathbf{u}_x \quad (2.63)$$

$$\mathbf{K}_z \mathbf{s}_x - \mathbf{K}_x \mathbf{s}_z = j k_0 \boldsymbol{\mu}_r \mathbf{u}_y \quad (2.64)$$

$$\mathbf{K}_x \mathbf{s}_y - \mathbf{K}_y \mathbf{s}_x = jk_0 \boldsymbol{\mu}_r \mathbf{u}_z \quad (2.65)$$

$$\mathbf{K}_y \mathbf{u}_z - \mathbf{K}_z \mathbf{u}_y = jk_0 \boldsymbol{\epsilon}_r \mathbf{s}_x \quad (2.66)$$

$$\mathbf{K}_z \mathbf{u}_x - \mathbf{K}_x \mathbf{u}_z = jk_0 \boldsymbol{\epsilon}_r \mathbf{s}_y \quad (2.67)$$

$$\mathbf{K}_x \mathbf{u}_y - \mathbf{K}_y \mathbf{u}_x = jk_0 \boldsymbol{\epsilon}_r \mathbf{s}_z \quad (2.68)$$

The matrices \mathbf{K}_x , \mathbf{K}_y , and \mathbf{K}_z are diagonal matrices containing the wave vector components of all of the spatial harmonics. The matrices $\boldsymbol{\mu}_r$ and $\boldsymbol{\epsilon}_r$ are full convolution matrices that arise from the Fourier transform operation [40]. The terms \mathbf{s}_x , \mathbf{s}_y , and \mathbf{s}_z are column vectors containing the electric field amplitudes of the spatial harmonics. Similarly, \mathbf{u}_x , \mathbf{u}_y , and \mathbf{u}_z are column vectors containing the magnetic field amplitudes of the spatial harmonics.

When the structure is uniform in one direction (2D lattices) and propagation is restricted to be within the transverse plane, we have $\mathbf{K}_z = 0$ and Eqs. (2.63)-(2.68) decouple into two sets of three equations. These sets of equations correspond to two independent electromagnetic modes. The transverse electric (TE) mode is described by

$$\mathbf{K}_x \mathbf{u}_y - \mathbf{K}_y \mathbf{u}_x = jk_0 \boldsymbol{\epsilon}_r \mathbf{s}_z \quad (2.69)$$

$$\mathbf{K}_y \mathbf{s}_z = jk_0 \boldsymbol{\mu}_r \mathbf{u}_x \quad (2.70)$$

$$-\mathbf{K}_x \mathbf{s}_z = jk_0 \boldsymbol{\mu}_r \mathbf{u}_y \quad (2.71)$$

and the transverse magnetic (TM) mode is described by

$$\mathbf{K}_x \mathbf{s}_y - \mathbf{K}_y \mathbf{s}_x = jk_0 \boldsymbol{\mu}_r \mathbf{u}_z \quad (2.72)$$

$$\mathbf{K}_y \mathbf{u}_z = jk_0 \boldsymbol{\epsilon}_r \mathbf{s}_x \quad (2.73)$$

$$-\mathbf{K}_x \mathbf{u}_z = jk_0 \boldsymbol{\epsilon}_r \mathbf{s}_y \quad (2.74)$$

A matrix wave equation can be derived for each of the above modes just in terms of either \mathbf{s}_z or \mathbf{u}_z . These are

$$\left(\mathbf{K}_x \boldsymbol{\mu}_r^{-1} \mathbf{K}_x + \mathbf{K}_y \boldsymbol{\mu}_r^{-1} \mathbf{K}_y\right) \mathbf{s}_z = k_0^2 \boldsymbol{\epsilon}_r \mathbf{s}_z \quad \text{TE Mode} \quad (2.75)$$

$$\left(\mathbf{K}_x \boldsymbol{\epsilon}_r^{-1} \mathbf{K}_x + \mathbf{K}_y \boldsymbol{\epsilon}_r^{-1} \mathbf{K}_y\right) \mathbf{u}_z = k_0^2 \boldsymbol{\mu}_r \mathbf{u}_z \quad \text{TM Mode} \quad (2.76)$$

These can be recognized as generalized eigen-value problems where k_0^2 is the eigen-value. The E mode has the electric field polarized out of the transverse plane while the H mode has the electric field polarized within the transverse plane.

2.4 Finite-Difference Analysis of Arbitrary Transmission Lines Embedded in Anisotropic Media

The fundamental mode in a transmission line is very close to TEM (transverse electromagnetic) mode. In this case, the analysis reduces to an electrostatic problem and transmission lines can be modeled using the inhomogeneous Laplace's equation instead of the more rigorous wave equation. This is done for greater speed and efficiency.

2.4.1 Formulation

Starting with Maxwell's divergence equation, the constitutive relation for the electric field in an anisotropic material, and the relation between the electric field and the scalar potential is given by

$$\begin{bmatrix} \frac{\partial}{\partial x} & \frac{\partial}{\partial y} \end{bmatrix} \begin{bmatrix} D_x(x, y) \\ D_y(x, y) \end{bmatrix} = 0 \quad (2.77)$$

$$\begin{bmatrix} D_x(x, y) \\ D_y(x, y) \end{bmatrix} = \epsilon_0 \begin{bmatrix} \epsilon_{xx}(x, y) & \epsilon_{xy}(x, y) \\ \epsilon_{yx}(x, y) & \epsilon_{yy}(x, y) \end{bmatrix} \begin{bmatrix} E_x(x, y) \\ E_y(x, y) \end{bmatrix} \quad (2.78)$$

$$\begin{bmatrix} E_x(x, y) \\ E_y(x, y) \end{bmatrix} = - \begin{bmatrix} \partial/\partial x \\ \partial/\partial y \end{bmatrix} V(x, y) \quad (2.79)$$

Deriving the inhomogeneous Laplace's equation by substituting Eq. (2.78) into (2.77) to eliminate the D field, and then substituting Eq. (2.79) into this new expression to eliminate the E field we obtain

$$\left[\begin{array}{cc} \frac{\partial}{\partial x} & \frac{\partial}{\partial y} \end{array} \right] \left[\begin{array}{cc} \epsilon_{xx}(x, y) & \epsilon_{xy}(x, y) \\ \epsilon_{yx}(x, y) & \epsilon_{yy}(x, y) \end{array} \right] \left[\begin{array}{c} \partial/\partial x \\ \partial/\partial y \end{array} \right] V(x, y) = 0 \quad (2.80)$$

Given a solution to this equation, the E field can be computed using (2.79) and then the D field computed using Eq. (2.78). At this point, all of the fields surrounding the device are known, can be visualized, and can be used to calculate the transmission line parameters. First, we calculate the distributed capacitance C of the line by looking at it as a capacitor. Given the electric fields, the total energy U stored in this system is

$$U = \frac{1}{2} \iint_A (\vec{D} \bullet \vec{E}) dx dy \quad (2.81)$$

This integral is taken over the entire cross section of the transmission line and must encompass all of the field energy. The energy stored in a capacitor is related to its capacitance C and stored voltage V_0 through Eq. (2.82).

$$U = CV_0^2/2 \quad (2.82)$$

Combining Eqs. (2.81) and (2.82) gives an equation to calculate the distributed capacitance from the electric fields.

$$C = \frac{1}{V_0^2} \iint_A (\vec{D} \bullet \vec{E}) dx dy \quad (2.83)$$

Second, if the medium surrounding the transmission line has no magnetic response, we can calculate the distributed inductance L directly from the distributed capacitance C_{air} of the same transmission line embedded in air instead of the anisotropic dielectric. In this case, the velocity of the wave on the line is related to the transmission line parameters through $c_0 \cong 1/\sqrt{LC_{air}}$.

Solving this for L yields

$$L = 1/(c_0^2 C_{air}). \quad (2.84)$$

Given the distributed inductance and capacitance, the characteristic impedance of the transmission line is

$$Z_0 = \sqrt{L/C} \quad (2.85)$$

and the propagation constant at frequency ω is

$$\beta = \omega\sqrt{LC}. \quad (2.86)$$

2.4.2 Numerical Solution to Equation (2.80)

The remaining challenge is to obtain the solution to Eq. (2.80). This was solved using a simple finite-difference method. This approach approximates the derivatives using central finite-differences. To handle this in a straightforward manner, we staggered the position of E_x , E_y , and V across a two-dimensional (2D) grid. The position of these terms across a 4×4 grid is illustrated in Figure 2.4.1. The potential is located at the origin of each cell in the grid. The electric fields are positioned at the cell boundaries, but offset from the origin by a half cell.

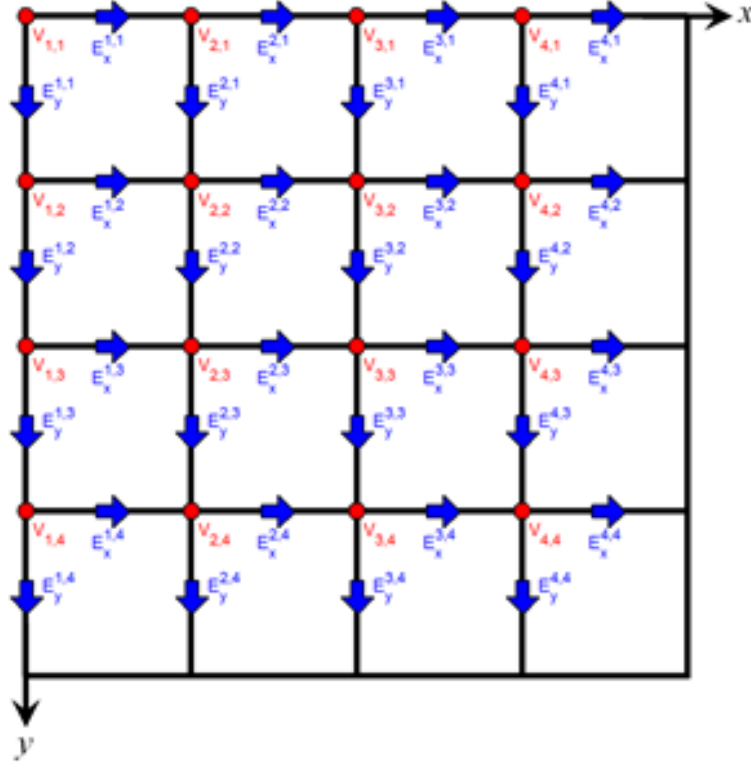


Figure 2.4.1: 4×4 grid for the finite-difference solution to Eq. (2.80)

After approximating the derivatives with finite-differences, each of Eqs. (2.77)-(2.79) are written once for every cell in the grid. These large sets of equations can be written in block matrix form as

$$\begin{bmatrix} \mathbf{D}_x & \mathbf{D}_y \end{bmatrix} \begin{bmatrix} \mathbf{d}_x \\ \mathbf{d}_y \end{bmatrix} = \mathbf{0} \quad (2.87)$$

$$\begin{bmatrix} \mathbf{d}_x \\ \mathbf{d}_y \end{bmatrix} = \begin{bmatrix} \boldsymbol{\epsilon}_{xx} & \mathbf{R}\boldsymbol{\epsilon}_{xy} \\ \mathbf{R}^T\boldsymbol{\epsilon}_{yx} & \boldsymbol{\epsilon}_{yy} \end{bmatrix} \begin{bmatrix} \mathbf{e}_x \\ \mathbf{e}_y \end{bmatrix} \quad (2.88)$$

$$\begin{bmatrix} \mathbf{e}_x \\ \mathbf{e}_y \end{bmatrix} = - \begin{bmatrix} \mathbf{D}_x^T \\ \mathbf{D}_y^T \end{bmatrix} \mathbf{v} \quad (2.89)$$

Here, \mathbf{D}_x and \mathbf{D}_y are banded matrices that calculate spatial derivatives of the electric fields across the staggered grid [41]. The ‘T’ superscript indicates a transposition. The terms $\boldsymbol{\epsilon}_{xx}$, $\boldsymbol{\epsilon}_{xy}$, $\boldsymbol{\epsilon}_{yx}$, and $\boldsymbol{\epsilon}_{yy}$ are diagonal matrices containing the permittivity functions across the grid. The functions $\boldsymbol{\epsilon}_{xx}$

and ϵ_{yx} are defined to be at the same points as E_x while the functions ϵ_{xy} and ϵ_{yy} are defined at the same points as E_y . \mathbf{R} is a banded matrix that interpolates the E_y quantities to be at the same positions as the E_x quantities [41]. \mathbf{R}^T is the transpose of \mathbf{R} and interpolates E_x quantities to be at the same positions as the E_y quantities. The terms \mathbf{d}_x , \mathbf{d}_y , \mathbf{e}_x and \mathbf{e}_y are column vectors containing the field components D_x , D_y , E_x , and E_y respectively throughout the grid. Lastly, \mathbf{v} is a column vector containing the scalar potential V throughout the grid. The matrix form of Eq. (2.80) is derived by substituting Eq. (2.88) into Eq. (2.87) to eliminate \mathbf{d}_x and \mathbf{d}_y , and then using Eq. (2.89) to eliminate \mathbf{e}_x and \mathbf{e}_y . The resulting block equation can be written as

$$\mathbf{L}\mathbf{v} = \mathbf{0} \quad (2.90)$$

$$\mathbf{L} = \begin{bmatrix} \mathbf{D}_x & \mathbf{D}_y \end{bmatrix} \begin{bmatrix} \epsilon_{xx} & \mathbf{R}\epsilon_{xy} \\ \mathbf{R}^T\epsilon_{yx} & \epsilon_{yy} \end{bmatrix} \begin{bmatrix} \mathbf{D}_x^T \\ \mathbf{D}_y^T \end{bmatrix}. \quad (2.91)$$

Eq. (2.90) has only a trivial solution because we have not yet defined the potential applied to the conductors. To do this, we construct a diagonal matrix \mathbf{F} which has 1's in the diagonal positions corresponding to where conductors are placed on the grid. 0's are placed everywhere else. We further construct a column vector \mathbf{v}_f which contains the voltages applied to each of the conductors identified in \mathbf{F} . Given these, we modify (2.90) according to [41]

$$\mathbf{L}'\mathbf{v} = \mathbf{b} \quad (2.92)$$

$$\mathbf{L}' = \mathbf{F} + (\mathbf{I} - \mathbf{F})\mathbf{L} \quad (2.93)$$

$$\mathbf{b} = \mathbf{F}\mathbf{v}_f. \quad (2.94)$$

We can now numerically solve Eq. (2.92) as $\mathbf{v} = (\mathbf{L}')^{-1}\mathbf{b}$. Given \mathbf{v} , the E field components are calculated using Eq. (2.89) and then the \bar{D} field components are calculated using Eq. (2.88). After these functions are obtained, the distributed capacitance is calculated according to Eq. (2.95).

$$C = \frac{\varepsilon_0 \cdot \Delta x \cdot \Delta y}{V_0^2} \begin{bmatrix} \mathbf{d}_x & \mathbf{d}_y \end{bmatrix} \begin{bmatrix} \mathbf{e}_x \\ \mathbf{e}_y \end{bmatrix}. \quad (2.95)$$

Note that the free space permittivity ε_0 was removed from Eq. (2.88) and inserted here for convenience. The entire solution process is repeated with the dielectric set to air. In this case, Eq. (2.91) reduces to the homogeneous Laplace's equation.

$$\mathbf{L}_h = \begin{bmatrix} \mathbf{D}_x & \mathbf{D}_y \end{bmatrix} \begin{bmatrix} \mathbf{D}_x^T \\ \mathbf{D}_y^T \end{bmatrix} \quad (2.96)$$

From this, the distributed inductance L is calculated from the distributed capacitance C_{air} using Eq. (2.84). Finally, the characteristic impedance and propagation constant are calculated using Eq. (2.85) and Eq. (2.86) respectively.

2.4.3 Benchmark Simulations

To demonstrate and benchmark the method described above, an ordinary microstrip transmission line was analyzed. The baseline design was obtained from the closed form expression in [42]. The width of the microstrip was $w = 4.0$ mm, the thickness of the substrate was $h = 3.0$ mm, and the dielectric constant of the substrate was $\varepsilon_r = 9.0$. The impedance calculated analytically using these dimensions was 49Ω .

The grid strategy for the numerical analysis is illustrated in Figure 2.4.2. In practice, many more grid cells are needed. The grid cells representing the substrate are shown in gray while the cells in air are shown in white. In Figure 2.4.2 the grid cells corresponding to the signal trace are shown in red. The digit '1' in these cells indicates that the potential is forced to $V_0 = 1.0$ V at these points. The grid cells corresponding to the ground metals are shown in blue. The digit '0' in these cells indicates that the potential is forced to 0 V at these points. The entire outer boundary was set to ground as the boundary condition. As long as the spacer regions shown in green are made large enough, usually 3 to 5 line widths, the model converges to the properties of a real microstrip in open air.

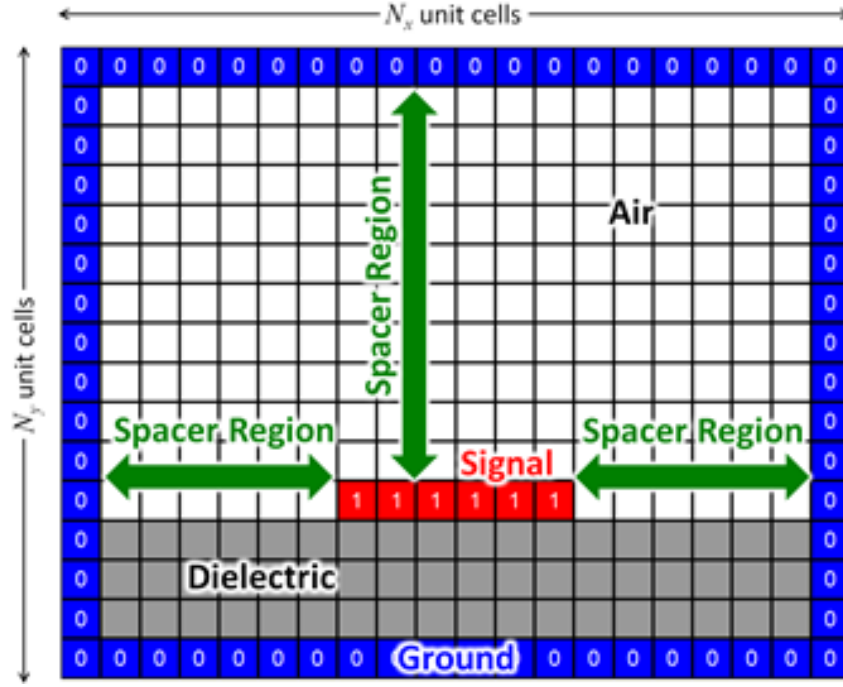


Figure 2.4.2: Grid strategy for finite-difference analysis of a microstrip transmission line

From this, we form four arrays describing the four dielectric tensor components (ϵ_{xx} , ϵ_{xy} , ϵ_{yx} , ϵ_{yy}). These arrays are depicted in Figure 2.4.3. This device has an isotropic substrate, so the off-diagonal terms ϵ_{xy} and ϵ_{yx} are zero here and the diagonal terms ϵ_{xx} and ϵ_{yy} are the same.

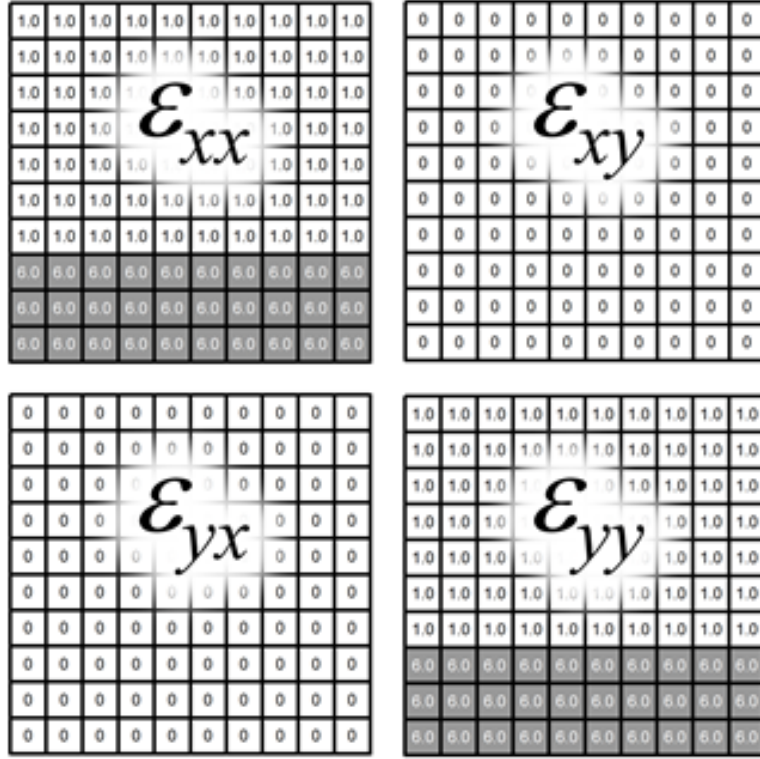


Figure 2.4.3: Four arrays describing the distribution of dielectric

For this analysis, the actual number of grid cells used was $N_x = 211$ and $N_y = 180$ representing a region of size $70.3 \text{ mm} \times 60 \text{ mm}$. The size of the grid cells was $\Delta x = \Delta y = 0.3333 \text{ mm}$. With these parameters, the line width was 12 cells and the substrate thickness was 9 cells. The results of this analysis are summarized in Figure: 2.4.4. The finite-difference analysis predicted the characteristic impedance to be 46Ω , which is very close to that predicted by the equation in [42].

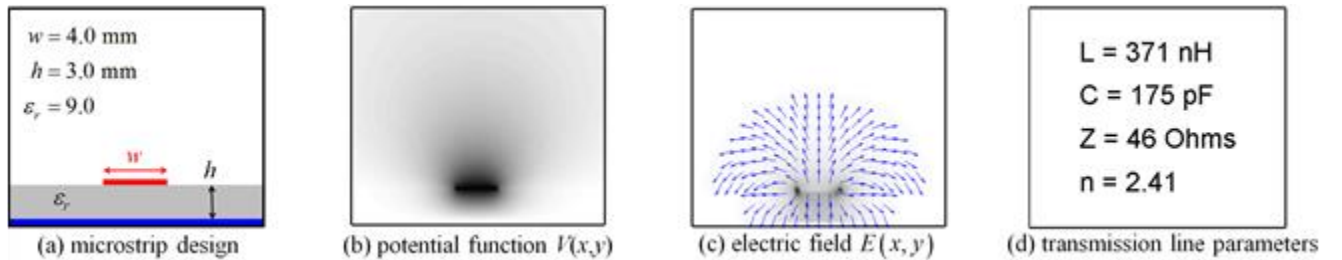


Figure 2.4.4: Numerical results for an ordinary microstrip

2.5 Anisotropic Finite-Difference Frequency-Domain Method

This section discusses in detail how the three-dimensional (3D) FDFD method described in [43] can be modified to incorporate anisotropic materials with arbitrary tensors.

2.5.1 Formulation

The formulation and implementation of the basic FDFD method is described in detail in [43], but this paper used only diagonal material tensors $[\mu]$ and $[\varepsilon]$. Below we generalized the formulation to incorporate arbitrary material tensors. After normalizing the magnetic field according to $\tilde{\vec{H}} = -j\eta_0\vec{H}$, Maxwell's curl equations with a uniaxial PML (UPML) [44] can be written as

$$\nabla \times \vec{E} = k_0 [\mu_r][s] \tilde{\vec{H}} \quad (2.97)$$

$$\nabla \times \tilde{\vec{H}} = k_0 [\varepsilon_r][s] \vec{E} \quad (2.98)$$

For a UPML, the tensor $[s]$ is expressed as

$$[s] = \begin{bmatrix} \frac{s_y s_z}{s_x} & 0 & 0 \\ 0 & \frac{s_x s_z}{s_y} & 0 \\ 0 & 0 & \frac{s_x s_y}{s_z} \end{bmatrix} \quad (2.99)$$

Without any approximation to the material tensors, Eqs. (2.97) and (2.98) can be expanded into the following set of six coupled partial differential equations. The μ_{ij} and ε_{ij} terms are relative to free space because the free space constants μ_0 and ε_0 have already been factored out.

$$\frac{\partial E_z}{\partial y'} - \frac{\partial E_y}{\partial z'} = \mu_{xx} \frac{s_y s_z}{s_x} \tilde{H}_x + \mu_{xy} \tilde{H}_y + \mu_{xz} \tilde{H}_z \quad (2.100)$$

$$\frac{\partial E_x}{\partial z'} - \frac{\partial E_z}{\partial x'} = \mu_{yx} \tilde{H}_x + \mu_{yy} \frac{s_x s_z}{s_y} \tilde{H}_y + \mu_{yz} \tilde{H}_z \quad (2.101)$$

$$\frac{\partial E_y}{\partial x'} - \frac{\partial E_x}{\partial y'} = \mu_{zx} \tilde{H}_x + \mu_{zy} \tilde{H}_y + \mu_{zz} \frac{s_x s_y}{s_z} \tilde{H}_z \quad (2.102)$$

$$\frac{\partial \tilde{H}_z}{\partial y'} - \frac{\partial \tilde{H}_y}{\partial z'} = \varepsilon_{xx} \frac{s_y s_z}{s_x} E_x + \varepsilon_{xy} E_y + \varepsilon_{zx} E_z \quad (2.103)$$

$$\frac{\partial \tilde{H}_x}{\partial z'} - \frac{\partial \tilde{H}_z}{\partial x'} = \varepsilon_{yx} E_x + \varepsilon_{yy} \frac{s_x s_z}{s_y} E_y + \varepsilon_{yz} E_z \quad (2.104)$$

$$\frac{\partial \tilde{H}_y}{\partial x'} - \frac{\partial \tilde{H}_x}{\partial y'} = \varepsilon_{zx} E_x + \varepsilon_{zy} E_y + \varepsilon_{zz} \frac{s_x s_y}{s_z} E_z \quad (2.105)$$

Here, the grid coordinates have been normalized according to

$$x' = k_0 x \quad y' = k_0 y \quad z' = k_0 z \quad (2.106)$$

2.5.1.1 Finite-Difference Approximation of Maxwell's Equations

Following the procedure outlined in [43], the fields and materials are assigned to discrete points on a Yee grid [45] and the derivatives in Eqs. (2.100)-(2.105) are approximated using central finite-differences. The indices i, j , and k are array indices. Figure 2.5.1 illustrates the Yee cell and summarizes where each of the tensor elements are defined to exist relative to the field components.

$$\begin{aligned} \frac{E_z|^{i,j+1,k} - E_z|^{i,j,k}}{\Delta y'} - \frac{E_y|^{i,j,k+1} - E_y|^{i,j,k}}{\Delta z'} &= \mu_{xx} \frac{s_y s_z}{s_x} \tilde{H}_x \Big|^{i,j,k} \\ &+ \frac{\mu_{xy} \tilde{H}_y \Big|^{i-1,j,k} + \mu_{xy} \tilde{H}_y \Big|^{i,j,k} + \mu_{xy} \tilde{H}_y \Big|^{i-1,j+1,k} + \mu_{xy} \tilde{H}_y \Big|^{i,j+1,k}}{4} \\ &+ \frac{\mu_{xz} \tilde{H}_z \Big|^{i-1,j,k} + \mu_{xz} \tilde{H}_z \Big|^{i,j,k} + \mu_{xz} \tilde{H}_z \Big|^{i-1,j,k+1} + \mu_{xz} \tilde{H}_z \Big|^{i,j,k+1}}{4} \end{aligned} \quad (2.107)$$

$$\frac{E_x|^{i,j,k+1} - E_x|^{i,j,k}}{\Delta z'} - \frac{E_z|^{i+1,j,k} - E_z|^{i,j,k}}{\Delta x'} = \frac{\mu_{yx}\tilde{H}_x|^{i,j,k} + \mu_{yx}\tilde{H}_x|^{i+1,j,k} + \mu_{yx}\tilde{H}_x|^{i,j-1,k} + \mu_{yx}\tilde{H}_x|^{i+1,j-1,k}}{4} + \mu_{yy}\frac{s_x s_z}{s_y}\tilde{H}_y\Big|^{i,j,k} \quad (2.108)$$

$$+ \frac{\mu_{yz}\tilde{H}_z|^{i,j-1,k} + \mu_{yz}\tilde{H}_z|^{i,j,k} + \mu_{yz}\tilde{H}_z|^{i,j-1,k+1} + \mu_{yz}\tilde{H}_z|^{i,j,k+1}}{4}$$

$$\frac{E_y|^{i+1,j,k} - E_y|^{i,j,k}}{\Delta x'} - \frac{E_x|^{i,j+1,k} - E_x|^{i,j,k}}{\Delta y'} = \frac{\mu_{zx}\tilde{H}_x|^{i,j,k} + \mu_{zx}\tilde{H}_x|^{i+1,j,k} + \mu_{zx}\tilde{H}_x|^{i,j,k-1} + \mu_{zx}\tilde{H}_x|^{i+1,j,k-1}}{4} + \frac{\mu_{zy}\tilde{H}_y|^{i,j,k} + \mu_{zy}\tilde{H}_y|^{i,j+1,k} + \mu_{zy}\tilde{H}_y|^{i,j,k-1} + \mu_{zy}\tilde{H}_y|^{i,j+1,k-1}}{4} + \mu_{zz}\frac{s_x s_y}{s_z}\tilde{H}_z\Big|^{i,j,k} \quad (2.109)$$

$$\frac{\tilde{H}_z|^{i,j,k} - \tilde{H}_z|^{i,j-1,k}}{\Delta y'} - \frac{\tilde{H}_y|^{i,j,k} - \tilde{H}_y|^{i,j,k-1}}{\Delta z'} = \varepsilon_{xx}\frac{s_y s_z}{s_x}E_x\Big|^{i,j,k} + \frac{\varepsilon_{xy}E_y|^{i,j-1,k} + \varepsilon_{xy}E_y|^{i,j,k} + \varepsilon_{xy}E_y|^{i+1,j-1,k} + \varepsilon_{xy}E_y|^{i+1,j,k}}{4} + \frac{\varepsilon_{xz}E_z|^{i,j,k} + \varepsilon_{xz}E_z|^{i+1,j,k} + \varepsilon_{xz}E_z|^{i,j,k-1} + \varepsilon_{xz}E_z|^{i+1,j,k-1}}{4} \quad (2.110)$$

$$\frac{\tilde{H}_x|^{i,j,k} - \tilde{H}_x|^{i,j,k-1}}{\Delta z'} - \frac{\tilde{H}_z|^{i,j,k} - \tilde{H}_z|^{i-1,j,k}}{\Delta x'} = \frac{\varepsilon_{yx}E_x|^{i-1,j,k} + \varepsilon_{yx}E_x|^{i,j,k} + \varepsilon_{yx}E_x|^{i-1,j+1,k} + \varepsilon_{yx}E_x|^{i,j+1,k}}{4} + \varepsilon_{yy}\frac{s_x s_z}{s_y}E_y\Big|^{i,j,k} + \frac{\varepsilon_{yz}E_z|^{i,j,k} + \varepsilon_{yz}E_z|^{i,j+1,k} + \varepsilon_{yz}E_z|^{i,j,k-1} + \varepsilon_{yz}E_z|^{i,j+1,k-1}}{4} \quad (2.111)$$

$$\frac{\tilde{H}_y|^{i,j,k} - \tilde{H}_y|^{i-1,j,k}}{\Delta x'} - \frac{\tilde{H}_x|^{i,j,k} - \tilde{H}_x|^{i,j-1,k}}{\Delta y'} = \frac{\varepsilon_{zx}E_x|^{i-1,j,k} + \varepsilon_{zx}E_x|^{i,j,k} + \varepsilon_{zx}E_x|^{i-1,j,k+1} + \varepsilon_{zx}E_x|^{i,j,k+1}}{4} + \frac{\varepsilon_{zy}E_y|^{i,j-1,k} + \varepsilon_{zy}E_y|^{i,j,k} + \varepsilon_{zy}E_y|^{i,j-1,k+1} + \varepsilon_{zy}E_y|^{i,j,k+1}}{4} + \varepsilon_{zz}\frac{s_x s_y}{s_z}E_z\Big|^{i,j,k} \quad (2.112)$$

In these equations, the terms containing off diagonal tensor elements require special treatment. Each term in a finite-difference equation must exist at the same point in space. In Eq. (2.107), each term is defined to exist at the same point as \tilde{H}_x . The central finite-difference ensures that the derivative terms on the left exist at this point. The last two terms on the right side of this equation are averaged at four points in the grid to interpolate the value at the same point as \tilde{H}_x . The same interpolation operation is used on every term in Eqs. (2.107)-(2.112) containing an off diagonal element.

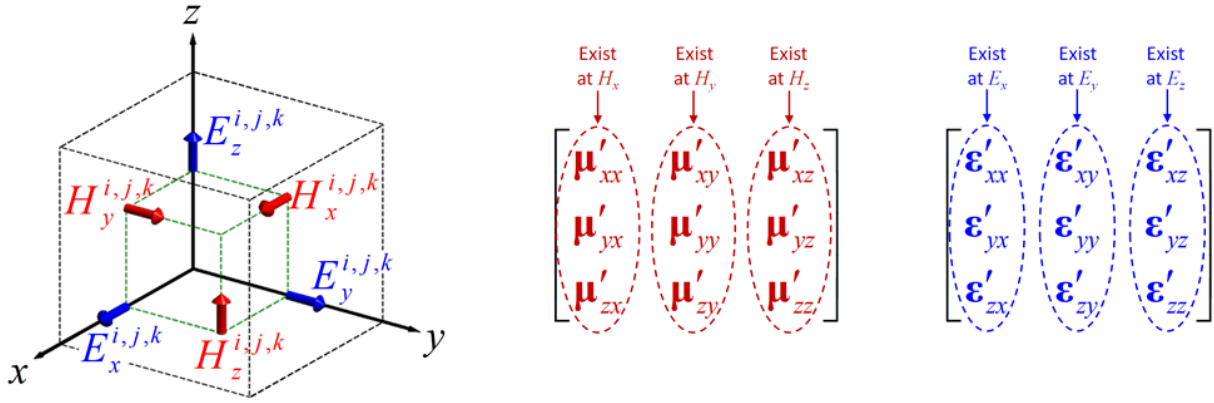


Figure 2.5.1 3D Yee cell along with position of the tensor elements

2.5.1.2 Maxwell's Equations in Matrix Form

Each equation above is written once for every cell in the grid so each finite-difference equation produces a large set of linear algebraic equations that can be written in matrix form as

$$\mathbf{D}'_y \mathbf{e}_z - \mathbf{D}'_z \mathbf{e}_y = \mu'_{xx} \tilde{\mathbf{h}}_x + \mu'_{xy} \tilde{\mathbf{h}}_y + \mu'_{xz} \tilde{\mathbf{h}}_z \quad (2.113)$$

$$\mathbf{D}'_z \mathbf{e}_x - \mathbf{D}'_x \mathbf{e}_z = \mu'_{yx} \tilde{\mathbf{h}}_x + \mu'_{yy} \tilde{\mathbf{h}}_y + \mu'_{yz} \tilde{\mathbf{h}}_z \quad (2.114)$$

$$\mathbf{D}'_x \mathbf{e}_y - \mathbf{D}'_y \mathbf{e}_x = \mu'_{zx} \tilde{\mathbf{h}}_x + \mu'_{zy} \tilde{\mathbf{h}}_y + \mu'_{zz} \tilde{\mathbf{h}}_z \quad (2.115)$$

$$\mathbf{D}^h_y \tilde{\mathbf{h}}_z - \mathbf{D}^h_z \tilde{\mathbf{h}}_y = \epsilon'_{xx} \mathbf{e}_x + \epsilon'_{xy} \mathbf{e}_y + \epsilon'_{xz} \mathbf{e}_z \quad (2.116)$$

$$\mathbf{D}^h_z \tilde{\mathbf{h}}_x - \mathbf{D}^h_x \tilde{\mathbf{h}}_z = \epsilon'_{yx} \mathbf{e}_x + \epsilon'_{yy} \mathbf{e}_y + \epsilon'_{yz} \mathbf{e}_z \quad (2.117)$$

$$\mathbf{D}_{x'}^h \tilde{\mathbf{h}}_y - \mathbf{D}_{y'}^h \tilde{\mathbf{h}}_x = \boldsymbol{\varepsilon}'_{zx} \mathbf{e}_x + \boldsymbol{\varepsilon}'_{zy} \mathbf{e}_y + \boldsymbol{\varepsilon}'_{zz} \mathbf{e}_z \quad (2.118)$$

The terms \mathbf{e}_x , \mathbf{e}_y , \mathbf{e}_z , $\tilde{\mathbf{h}}_x$, $\tilde{\mathbf{h}}_y$, and $\tilde{\mathbf{h}}_z$ are column vectors that contain all of the field components throughout the entire grid reshaped into linear arrays. The terms $\mathbf{D}_{x'}^e$, $\mathbf{D}_{y'}^e$, and $\mathbf{D}_{z'}^e$ are banded matrices that calculate first-order spatial derivatives of the electric fields across the grid. Similarly, the terms $\mathbf{D}_{x'}^h$, $\mathbf{D}_{y'}^h$, and $\mathbf{D}_{z'}^h$ calculate first-order spatial derivatives of the magnetic fields across the grid.

When the 3D code is being used to model 2D or 1D systems, the derivatives along the uniform directions take the special forms in Eq. (2.119) where the wave vector of the source is given by $\vec{k}_{\text{inc}} = k_x \hat{x} + k_y \hat{y} + k_z \hat{z}$.

$$\mathbf{D}_{x'}^e = \mathbf{D}_{x'}^h = -j \frac{k_x}{k_0} \mathbf{I} \quad \text{for devices uniform along } x, N_x = 1 \quad (2.119)$$

$$\mathbf{D}_{y'}^e = \mathbf{D}_{y'}^h = -j \frac{k_y}{k_0} \mathbf{I} \quad \text{for devices uniform along } y, N_y = 1 \quad (2.119)$$

$$\mathbf{D}_{z'}^e = \mathbf{D}_{z'}^h = -j \frac{k_z}{k_0} \mathbf{I} \quad \text{for devices uniform along } z, N_z = 1 \quad (2.119)$$

Finally, the terms $\boldsymbol{\mu}'_{mn}$ and $\boldsymbol{\varepsilon}'_{mn}$ are diagonal matrices containing the relative permeability and relative permittivity of those tensor elements through the grid along their diagonals. In addition, the PML terms and interpolation operations have been absorbed into these quantities giving them the following general form. The prime denotes that the material tensors have been modified.

$$[\boldsymbol{\mu}'_r] = \begin{bmatrix} \boldsymbol{\mu}'_{xx} & \boldsymbol{\mu}'_{xy} & \boldsymbol{\mu}'_{xz} \\ \boldsymbol{\mu}'_{yx} & \boldsymbol{\mu}'_{yy} & \boldsymbol{\mu}'_{yz} \\ \boldsymbol{\mu}'_{zx} & \boldsymbol{\mu}'_{zy} & \boldsymbol{\mu}'_{zz} \end{bmatrix} = \begin{bmatrix} \boldsymbol{\mu}_{xx} \mathbf{s}_x^{-1} \mathbf{s}_y \mathbf{s}_z & \mathbf{R}_x^- \mathbf{R}_y^+ \boldsymbol{\mu}_{xy} & \mathbf{R}_x^- \mathbf{R}_z^+ \boldsymbol{\mu}_{xz} \\ \mathbf{R}_y^- \mathbf{R}_x^+ \boldsymbol{\mu}_{yx} & \boldsymbol{\mu}_{yy} \mathbf{s}_x \mathbf{s}_y^{-1} \mathbf{s}_z & \mathbf{R}_y^- \mathbf{R}_z^+ \boldsymbol{\mu}_{yz} \\ \mathbf{R}_z^- \mathbf{R}_x^+ \boldsymbol{\mu}_{zx} & \mathbf{R}_z^- \mathbf{R}_y^+ \boldsymbol{\mu}_{zy} & \boldsymbol{\mu}_{zz} \mathbf{s}_x \mathbf{s}_y \mathbf{s}_z^{-1} \end{bmatrix} \quad (2.120)$$

$$[\boldsymbol{\varepsilon}'_r] = \begin{bmatrix} \boldsymbol{\varepsilon}'_{xx} & \boldsymbol{\varepsilon}'_{xy} & \boldsymbol{\varepsilon}'_{xz} \\ \boldsymbol{\varepsilon}'_{yx} & \boldsymbol{\varepsilon}'_{yy} & \boldsymbol{\varepsilon}'_{yz} \\ \boldsymbol{\varepsilon}'_{zx} & \boldsymbol{\varepsilon}'_{zy} & \boldsymbol{\varepsilon}'_{zz} \end{bmatrix} = \begin{bmatrix} \boldsymbol{\varepsilon}_{xx} \mathbf{s}_x^{-1} \mathbf{s}_y \mathbf{s}_z & \mathbf{R}_x^+ \mathbf{R}_y^- \boldsymbol{\varepsilon}_{xy} & \mathbf{R}_x^+ \mathbf{R}_z^- \boldsymbol{\varepsilon}_{xz} \\ \mathbf{R}_y^+ \mathbf{R}_x^- \boldsymbol{\varepsilon}_{yx} & \boldsymbol{\varepsilon}_{yy} \mathbf{s}_x \mathbf{s}_y^{-1} \mathbf{s}_z & \mathbf{R}_y^+ \mathbf{R}_z^- \boldsymbol{\varepsilon}_{yz} \\ \mathbf{R}_z^+ \mathbf{R}_x^- \boldsymbol{\varepsilon}_{zx} & \mathbf{R}_z^+ \mathbf{R}_y^- \boldsymbol{\varepsilon}_{zy} & \boldsymbol{\varepsilon}_{zz} \mathbf{s}_x \mathbf{s}_y \mathbf{s}_z^{-1} \end{bmatrix} \quad (2.121)$$

[illegible]

(2.123)

36

as $\mathbf{R}_i^+ = (\mathbf{R}_i^-)^H$. Using interpolation matrices in this manner allows straightforward implementation of higher order interpolation schemes without having to modify the rest of the FDFD code.

Maxwell's curl equations can now be written in block matrix form as

$$\mathbf{C}^e \vec{\mathbf{e}} = [\boldsymbol{\mu}'_r] \vec{\mathbf{h}} \quad (2.124)$$

$$\mathbf{C}^h \vec{\mathbf{h}} = [\boldsymbol{\epsilon}'_r] \vec{\mathbf{e}} \quad (2.125)$$

$$\vec{\mathbf{e}} = \begin{bmatrix} \mathbf{e}_x \\ \mathbf{e}_y \\ \mathbf{e}_z \end{bmatrix} \quad \vec{\mathbf{h}} = \begin{bmatrix} \tilde{\mathbf{h}}_x \\ \tilde{\mathbf{h}}_y \\ \tilde{\mathbf{h}}_z \end{bmatrix} \quad (2.126)$$

$$\mathbf{C}^e = \begin{bmatrix} \mathbf{0} & -\mathbf{D}_{z'}^e & \mathbf{D}_{y'}^e \\ \mathbf{D}_{z'}^e & \mathbf{0} & -\mathbf{D}_{x'}^e \\ -\mathbf{D}_{y'}^e & \mathbf{D}_{x'}^e & \mathbf{0} \end{bmatrix} \quad \mathbf{C}^h = \begin{bmatrix} \mathbf{0} & -\mathbf{D}_{z'}^h & \mathbf{D}_{y'}^h \\ \mathbf{D}_{z'}^h & \mathbf{0} & -\mathbf{D}_{x'}^h \\ -\mathbf{D}_{y'}^h & \mathbf{D}_{x'}^h & \mathbf{0} \end{bmatrix} \quad (2.127)$$

2.5.1.3 Matrix Wave Equation

A matrix wave equation can be derived for the electric field by solving Eq. (2.124) for $\vec{\mathbf{h}}$ and substituting that expression into Eq. (2.125). A similar wave equation can be derived for the magnetic field by solving Eq. (2.125) for $\vec{\mathbf{e}}$ and substituting that expression into Eq. (2.124). It is useful to write the matrix equations in terms of a wave matrix \mathbf{A} and the unknown fields, $\vec{\mathbf{e}}$ or $\vec{\mathbf{h}}$.

$$\mathbf{A}_e \vec{\mathbf{e}} = \mathbf{0} \quad \mathbf{A}_e = \mathbf{C}^h [\boldsymbol{\mu}'_r]^{-1} \mathbf{C}^e - [\boldsymbol{\epsilon}'_r] \quad (2.128)$$

$$\mathbf{A}_h \vec{\mathbf{h}} = \mathbf{0} \quad \mathbf{A}_h = \mathbf{C}^e [\boldsymbol{\epsilon}'_r]^{-1} \mathbf{C}^h - [\boldsymbol{\mu}'_r] \quad (2.129)$$

These equations cannot yet be solved because a source has not yet been incorporated.

2.5.1.4 Assignment of Anisotropic Materials to the Grid

The manner in which the materials are assigned to the grid can be discerned from Eqs. (2.107) - (2.112) and is illustrated in Figure 2.5.1. The tensor elements ϵ_{xx} , ϵ_{yx} , and ϵ_{zx} are defined to exist at the same points as E_x . The tensor elements ϵ_{xy} , ϵ_{yy} , and ϵ_{zy} are defined to exist at the

same points as E_y . The tensor elements ε_{xz} , ε_{yz} and ε_{zz} are defined to exist at the same points as E_z . Likewise, the tensor elements μ_{xx} , μ_{yx} , and μ_{zx} are defined to exist at the same points as H_x . The tensor elements μ_{xy} , μ_{yy} , and μ_{zy} are defined to exist at the same points as H_y . The tensor elements μ_{xz} , μ_{yz} and μ_{zz} are defined to exist at the same points as H_z .

The material tensors at each point in the grid can be completely unique. Physical materials have only three degrees of freedom where the three numbers represent the material response along the principle axes of the material \hat{a} , \hat{b} , and \hat{c} . When the tensors are expressed in this canonical system, they are diagonal and the three degrees of freedom are explicit. Most often, anisotropic materials are specified in this manner.

$$\begin{bmatrix} \varepsilon_a & 0 & 0 \\ 0 & \varepsilon_b & 0 \\ 0 & 0 & \varepsilon_c \end{bmatrix} \quad \text{and} \quad \begin{bmatrix} \mu_a & 0 & 0 \\ 0 & \mu_b & 0 \\ 0 & 0 & \mu_c \end{bmatrix} \quad (2.130)$$

To incorporate a tensor into a Cartesian grid, it is first necessary to convert the tensor given along the principle axes $[\varepsilon^{abc}]$ to an equivalent tensor in the coordinates of the model $[\varepsilon^{xyz}]$. In this case, that is Cartesian coordinates that may differ from the axes of the anisotropic material. The transformation is accomplished using Eq. (2.131) where \mathbf{R} is a transformation matrix

$$[\varepsilon^{xyz}] = \mathbf{R}[\varepsilon^{abc}]\mathbf{R}^T \quad (2.131)$$

$$\mathbf{R} = \begin{bmatrix} \hat{x} \bullet \hat{a} & \hat{x} \bullet \hat{b} & \hat{x} \bullet \hat{c} \\ \hat{y} \bullet \hat{a} & \hat{y} \bullet \hat{b} & \hat{y} \bullet \hat{c} \\ \hat{z} \bullet \hat{a} & \hat{z} \bullet \hat{b} & \hat{z} \bullet \hat{c} \end{bmatrix} \quad (2.132)$$

The Cartesian tensor can be rotated into an arbitrary orientation using rotation matrices. Eq. (2.133) rotates the tensor $[\varepsilon]$ by angle θ about the i^{th} axis. Rotation matrices are both real and unitary so $[R]^T = [R]^{-1}$.

$$[\varepsilon^{\text{rot}}] = [R_i(\theta)][\varepsilon^{xyz}][R_i(\theta)]^T \quad (2.133)$$

Rotation matrices that rotate about the x , y , and z axes by an angle θ are given by Eq. (2.134), Eq. (2.135), and Eq. (2.136) respectively.

$$[R_x(\theta)] = \begin{bmatrix} 1 & 0 & 0 \\ 0 & \cos \theta & -\sin \theta \\ 0 & \sin \theta & \cos \theta \end{bmatrix} \quad (2.134)$$

$$[R_y(\theta)] = \begin{bmatrix} \cos \theta & 0 & \sin \theta \\ 0 & 1 & 0 \\ -\sin \theta & 0 & \cos \theta \end{bmatrix} \quad (2.135)$$

$$[R_z(\theta)] = \begin{bmatrix} \cos \theta & -\sin \theta & 0 \\ \sin \theta & \cos \theta & 0 \\ 0 & 0 & 1 \end{bmatrix} \quad (2.136)$$

Rotation matrices can also be used in combination. For example, to rotate a tensor by 30° about the z -axis and then 120° about the x -axis, the following sequence of multiplications should be used.

$$[\varepsilon^{\text{rot}}] = [R_x(120^\circ)][R_z(30^\circ)][\varepsilon^{\text{xyz}}][R_z(30^\circ)]^T [R_x(120^\circ)]^T \quad (2.137)$$

2.5.1.5 Total-Field/Scattered-Field Formulation

The powerful total-field/scattered-field (TF/SF) technique described in [43] for incorporating a source can still be applied, but three field components are needed. The source field $\vec{\mathbf{e}}_{\text{src}}$ is constructed according to Eq. (2.138). It is a column vector composed of three smaller column vectors $\mathbf{e}_{x,\text{src}}$, $\mathbf{e}_{y,\text{src}}$, and $\mathbf{e}_{z,\text{src}}$ that each contain the field components of the source throughout the grid, but reshaped into 1D arrays.

$$\vec{\mathbf{e}}_{\text{src}} = \begin{bmatrix} \mathbf{e}_{x,\text{src}} \\ \mathbf{e}_{y,\text{src}} \\ \mathbf{e}_{z,\text{src}} \end{bmatrix} \quad (2.138)$$

$$\mathbf{e}_{x,\text{src}} = \begin{bmatrix} e_{x,\text{src}}^{(1,1,1)} \\ e_{x,\text{src}}^{(1,1,2)} \\ \vdots \\ e_{x,\text{src}}^{(N_x, N_y, N_z)} \end{bmatrix} \quad \mathbf{e}_{y,\text{src}} = \begin{bmatrix} e_{y,\text{src}}^{(1,1,1)} \\ e_{y,\text{src}}^{(1,1,2)} \\ \vdots \\ e_{y,\text{src}}^{(N_x, N_y, N_z)} \end{bmatrix} \quad \mathbf{e}_{z,\text{src}} = \begin{bmatrix} e_{z,\text{src}}^{(1,1,1)} \\ e_{z,\text{src}}^{(1,1,2)} \\ \vdots \\ e_{z,\text{src}}^{(N_x, N_y, N_z)} \end{bmatrix} \quad (2.139)$$

The masking matrix \mathbf{Q} is constructed to be in the form of Eq. (2.140). It is a block diagonal matrix composed of three matrices along its diagonal. \mathbf{Q}_x is the scattered-field masking for the E_x field, \mathbf{Q}_y is the scattered-field masking matrix for E_y field, and \mathbf{Q}_z is the scattered-field masking matrix for the E_z field.

$$\mathbf{Q} = \begin{bmatrix} \mathbf{Q}_x & \mathbf{0} & \mathbf{0} \\ \mathbf{0} & \mathbf{Q}_y & \mathbf{0} \\ \mathbf{0} & \mathbf{0} & \mathbf{Q}_z \end{bmatrix} \quad (2.140)$$

Given the wave matrix \mathbf{A} , source field \mathbf{f}_{src} , and the masking matrix \mathbf{Q} , the source vector \mathbf{b} is calculated according to

$$\mathbf{b} = (\mathbf{QA} - \mathbf{AQ})\bar{\mathbf{e}}_{\text{src}} \quad (2.141)$$

Now that a source has been incorporated, the field is calculated according to Eq. (2.142). Note that $\bar{\mathbf{e}}$ must be parsed to extract the individual components \mathbf{e}_x , \mathbf{e}_y , and \mathbf{e}_z . These three terms can then be reshaped back to the original grid.

$$\bar{\mathbf{e}} = \begin{bmatrix} \mathbf{e}_x \\ \mathbf{e}_y \\ \mathbf{e}_z \end{bmatrix} = \mathbf{A}^{-1}\mathbf{b} \quad (2.142)$$

If needed, the magnetic field can be calculated using Eq. (2.126). This is

$$\tilde{\mathbf{h}} = [\boldsymbol{\mu}'_r]^{-1} \mathbf{C}^e \bar{\mathbf{e}} \quad (2.143)$$

2.5.2 Benchmark Simulation

2.5.2.1 Scattering from an Anisotropic Guided-Mode Resonance Filter

Guided-mode resonance (GMR) filters consist of two electromagnetically coupled devices; a grating and a slab waveguide. When an external electromagnetic wave is incident on the device and a precise phase matching condition is met, the external wave is diffracted by the grating and coupled into guided mode within the slab. Due to reciprocity, the guided waves slowly leak back out of the slab waveguide. The leaked wave interferes with the incident wave to produce the overall frequency response [44, 46, 47].

GMR devices using ruled gratings are inherently sensitive to polarization due to the birefringence imposed by the grating. By incorporating anisotropy into the design, it becomes possible to introduce birefringence that counteracts the grating to realize polarization independent designs. Using the AFDFD code, an anisotropic ruled-grating GMR filter was designed to be polarization insensitive. The results were verified by simulating the same design with Ansys HFSS. Both HFSS and AFDFD used a plane wave as a source and periodic boundaries on the sides. AFDFD used UMPL's on the top and bottom, but HFSS used Floquet ports.

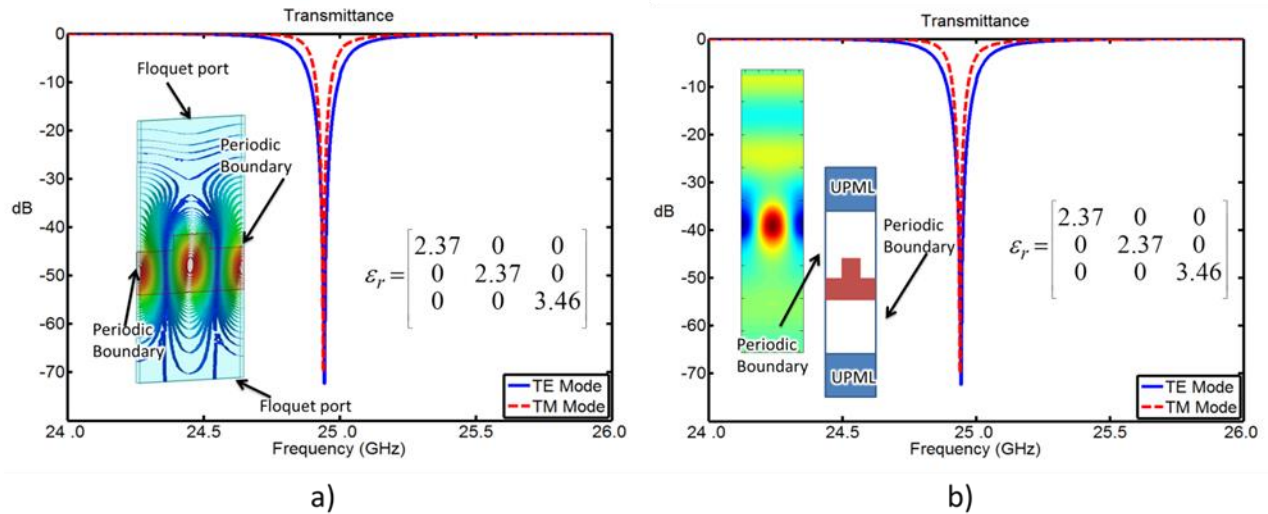


Figure 2.5.2: Anisotropic GMR filter spectral response simulated with Ansys HFSS b) Anisotropic GMR spectral response simulated with AFDFD

Figure 2.5.2 depicts the spectral response of an anisotropic GMR filter. Both the transvers electric (TE) and transvers magnetic (TM) modes were made resonant at the same frequency. Using the method presented in Chapter 3, a device could be realized using an anisotropic metamaterial like the one shown in Figure 2.5.3.

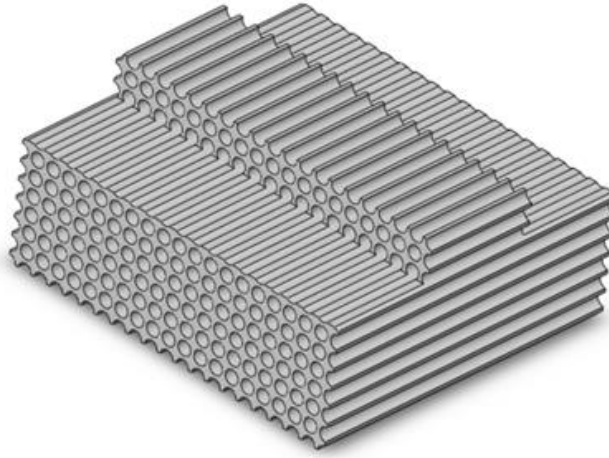


Figure 2.5.3: Prototype of anisotropic GMR filter

2.6 Tool for Synthesizing Spatially Variant Lattices

The spatially variant lattice (SVL) tool is capable of simultaneously spatially varying every property of a periodic structure throughout a volume in a way that renders the final geometry smooth and continuous. Avoiding discontinuities is important because these produce scattering and field concentrations that can degrade the performance of the overall device [48]. A detailed description of this algorithm is given in Ref. [48].

2.6.1 Required Data

Before performing the synthesis procedure, several sets of data must be defined. This usually begins by designing the lattice unit cell that performs the desired function. While dozens of functions are possible, this work is concentrating on anisotropy. An example unit cell is shown in Figure 2.6.1(left).

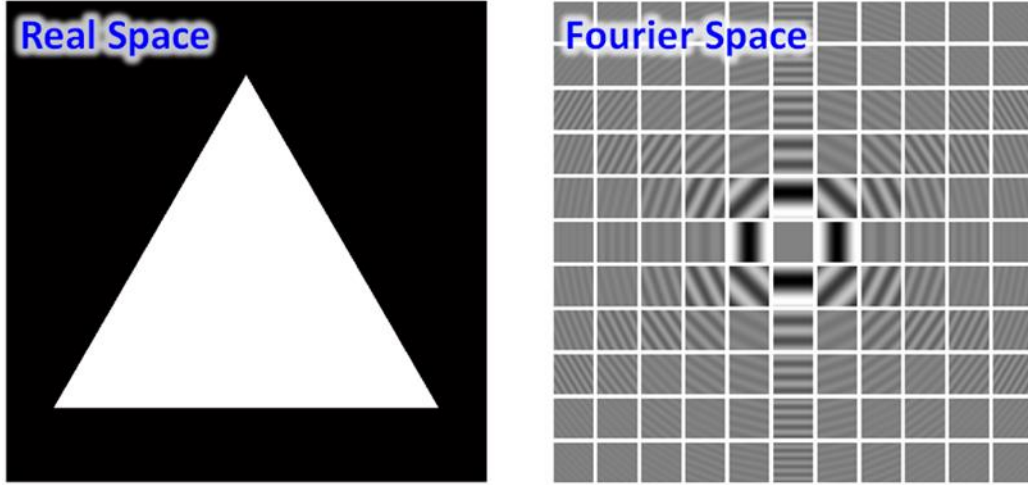


Figure 2.6.1: Metamaterial unit cell and its constituent 1D gratings [12]

The unit cell is decomposed into a set of constituent 1D gratings using a fast Fourier transform (FFT). These are called spatial harmonics and each of them has a complex amplitude a_m and a grating vector \vec{K}_m associated with it. The complex amplitudes are the Fourier coefficients. The grating vectors for rectangular symmetry are calculated according to

$$\begin{aligned} K_x &= \frac{2\pi p}{\Lambda_x} & p = \dots, -2, -1, 0, 1, 2, \dots \\ K_y &= \frac{2\pi q}{\Lambda_y} & q = \dots, -2, -1, 0, 1, 2, \dots \end{aligned} \quad (2.144)$$

This set of 1D gratings is shown in Figure 2.6.1(right). The original unit cell containing a triangle can be reconstructed by summing all of the 1D gratings. An infinite number of spatial harmonics are needed to perfectly reconstruct the original unit cell. In practice, excellent reconstruction is still possible using only a limited set of harmonics. Eq. (2.145) shows this truncated summation taken over M spatial harmonics.

$$\varepsilon_r(\vec{r}) = \sum_{m=1}^M a_m \exp(-j\vec{K}_m \bullet \vec{r}) \quad (2.145)$$

Next, a direction field is constructed that defines the local orientations that the unit cells should have throughout the volume. An example direction field and the resulting spatially variant lattice is shown in Figure 2.6.2.

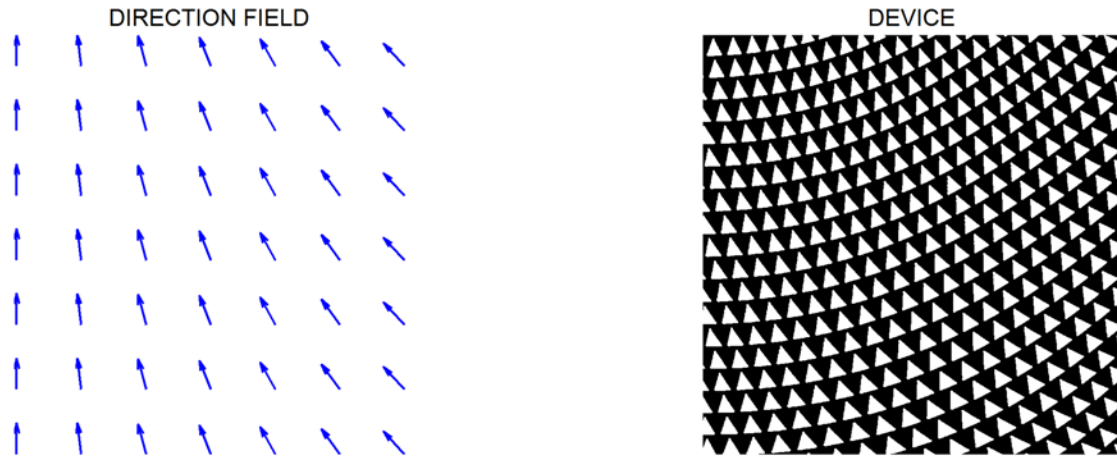


Figure 2.6.2: Direction field and resulting spatially variant lattice [12]

Finally, fields defining the spatially variant lattice period fill factor, or even geometry can be defined. Figure 2.6.3 shows a map of how the lattice period should be spatially varied, along with the resulting spatially variant lattice.

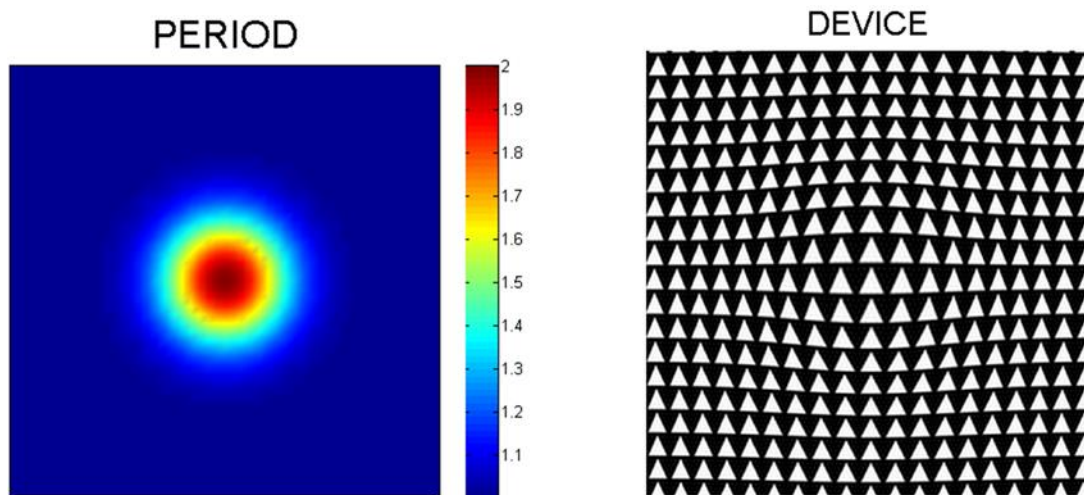


Figure 2.6.3: Lattice period field and resulting spatially variant lattice [12]

2.6.2 Formulation

At this point, all of the information that is needed to perform the synthesis is defined. The synthesis tool is a loop that builds the overall device by spatially varying each 1D grating independently and then adding the results. The steps performed inside this loop are described below.

Step 1 – Construct Spatially Variant K-Field

Given the grating vector \vec{K}_m of a spatial harmonic, an array $\vec{K}'_m(\vec{r})$ is constructed that places this vector uniformly across the grid. This is called the “K-field.” If a grating were reconstructed from this data, a simple uniform sinusoidal grating would be observed.

Next, each point in the K-field is converted to polar coordinates. This produces a “magnitude field” and an “angle field” where spatially variant properties are more easily and intuitively incorporated. The angular tilt defined by the direction field is added to the angle field. This incorporates spatially variant unit cell orientation. Variations in the lattice period are incorporated into the magnitude field. The spatially variant K-field is reconstructed by converting from polar coordinates back into rectangular coordinates.

Step 2 – Compute Grating Phase Function

At this point it is tempting to construct the spatially variant 1D grating by directly using Eq. (2.146). This approach, however, fails to properly reconstruct the spatially variant 1D grating as illustrated in Figure 2.6.4(b)

$$\varepsilon_m(\vec{r}) = \sum_{m=1}^M a_m \exp \left[-j \vec{K}'_m(\vec{r}) \bullet \vec{r} \right] \quad (2.146)$$

The correct approach is to apply the concept of grating phase function which treats a 1D grating mathematically like a wave. The grating phase $\phi_m(\vec{r})$ is related to the K-field through the following differential Eq..

$$\nabla \phi_m(\vec{r}) = \vec{K}'_m(\vec{r}) \quad (2.147)$$

Figure 2.6.4(c) shows the grating phase function that was calculated from the K-field shown in Figure 2.6.4(a). To correctly reconstruct the 1D grating, Eq. (2.148) is solved for ϕ_m and then the grating phase term is directly used to reconstruct the grating according to

$$\varepsilon_m(\vec{r}) = a_m \exp[-j\phi_m(\vec{r})] \quad (2.148)$$

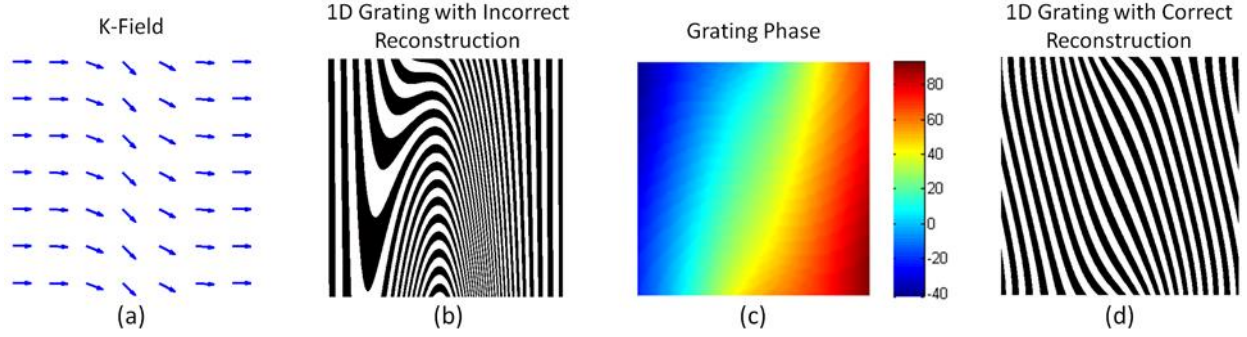


Figure 2.6.4.: Correct method for generating spatially variant 1D gratings [12]

Eq. (2.147) was solved for the grating phase using the finite-difference method. The derivatives in this equation were approximated using finite-differences. The resulting equation is written for each point in the grid. This large set of equations is written in matrix form as

$$\begin{bmatrix} \mathbf{D}_x \\ \mathbf{D}_y \\ \mathbf{D}_z \end{bmatrix} \Phi_m = \begin{bmatrix} \mathbf{K}_{x,m} \\ \mathbf{K}_{y,m} \\ \mathbf{K}_{z,m} \end{bmatrix} \quad (2.149)$$

The term Φ_m is a column vector containing the grating phase at each point on the grid. These are not known at this point, but will be solved for shortly. The terms \mathbf{D}_x , \mathbf{D}_y , and \mathbf{D}_z are banded matrices that perform derivative operations across the grid. The terms $\mathbf{K}_{x,m}$, $\mathbf{K}_{y,m}$, and $\mathbf{K}_{z,m}$ are diagonal matrices containing the components of the K-field across the grid. This matrix equation is solved for the grating phase as follows.

$$\Phi_m = \begin{bmatrix} \mathbf{D}_x \\ \mathbf{D}_y \\ \mathbf{D}_z \end{bmatrix}^{-1} \begin{bmatrix} \mathbf{K}_{x,m} \\ \mathbf{K}_{y,m} \\ \mathbf{K}_{z,m} \end{bmatrix} \quad (2.150)$$

Step 3 – Construct Spatially Variant 1D Grating

Given the grating phase function across the grid, the 1D grating associated with the m^{th} spatial harmonic is reconstructed using Eq. (2.148). It is important to note that the dielectric function $\varepsilon_m(\vec{r})$ is complex at this point. While it is not needed, the 1D grating can be reconstructed by taking the real part.

Step 4 – Construct Overall Spatially Variant Lattice

The overall spatially variant lattice is reconstructed by summing all of the spatially variant 1D gratings associated with each of the spatial harmonics. This is a complex function since the component 1D gratings are complex. The final device is reconstructed by taking the real part of the summation.

$$\varepsilon(\vec{r}) = \text{Re} \left[\sum_{m=1}^M \varepsilon_m(\vec{r}) \right] \quad (2.151)$$

In many cases, it is advantageous to reconstruct the final device using a threshold function. This can be used to form a binary structure or to control the fill factor.

$$\varepsilon(\vec{r}) = \begin{cases} \varepsilon_1 & \text{Re}[\Sigma \varepsilon_m] \leq \gamma \\ \varepsilon_2 & \text{Re}[\Sigma \varepsilon_m] > \gamma \end{cases} \quad (2.152)$$

2.7 Transformation Optics

The method of transformation optics (TO) was originally developed to work at optical frequencies [49], but since it is based on the fact the Maxwell's Equations are form-invariant, meaning that Maxwell's Equations are the same regardless of coordinate system they are applied to, it can be used at any frequency. TO works by defining a coordinate transform that would “bend” the electromagnetic fields in the desired manner and then incorporating the coordinate transform into the permittivity and permeability tensors. This is shown in Figure 2.7.1.

$$\vec{r}' = T(\vec{r})$$

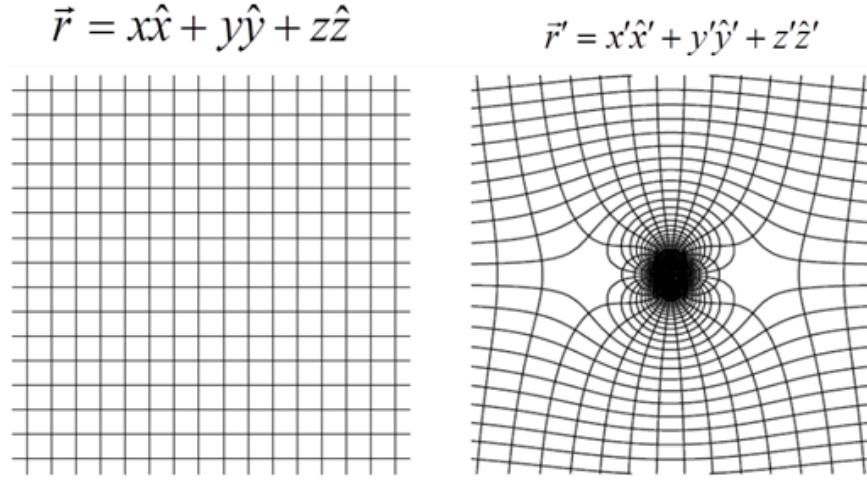


Figure 2.7.1: Example of coordinate transformation [12]

2.7.1 Formulation

To aid in the coordinate transformation, we use the Jacobian transformation matrix. The Jacobian matrix does not perform a coordinate transformation, but it transforms functions and operations between different coordinate systems.

$$[A] = (\nabla \vec{r}')^T = \begin{bmatrix} \frac{\partial x'}{\partial x} & \frac{\partial x'}{\partial y} & \frac{\partial x'}{\partial z} \\ \frac{\partial y'}{\partial x} & \frac{\partial y'}{\partial y} & \frac{\partial y'}{\partial z} \\ \frac{\partial z'}{\partial x} & \frac{\partial z'}{\partial y} & \frac{\partial z'}{\partial z} \end{bmatrix} \quad (2.153)$$

A vector function in two coordinate systems is related through the Jacobian matrix as follows.

$$\vec{E}'(\vec{r}') = ([A]^T)^{-1} \vec{E}(\vec{r}) \quad (2.154)$$

An operation can also be transformed between two coordinate systems using the Jacobian matrix.

$$[F'(\vec{r}')] = \frac{[A][F(\vec{r})][A]^T}{\det[A]} \quad (2.155)$$

Since Maxwell's equations are form-invariant, the coordinate transform can be absorbed solely into the material properties. In any coordinate system Maxwell's equations can be written as

$$\nabla \times \vec{H} = j\omega[\varepsilon]\vec{E} \quad (2.156)$$

$$\nabla \times \vec{E} = j\omega[\mu]\vec{H} \quad (2.157)$$

Now, we apply a coordinate transform to Maxwell's equations and absorb that into the material properties. This result is Maxwell's equations again, but with modified constitutive parameters.

$$\nabla' \times \vec{H}' = j\omega[\varepsilon']\vec{E}' \quad (2.158)$$

$$\nabla' \times \vec{E}' = j\omega[\mu']\vec{H}' \quad (2.159)$$

This can be easily proven. Defining the coordinate transformation as:

$$\vec{r}' = \vec{r}'(\vec{r}) \quad (2.160)$$

We now have

$$\vec{E}'(\vec{r}') = \left([A]^T\right)^{-1} \vec{E}(\vec{r}) \quad (2.161)$$

$$\vec{H}'(\vec{r}') = \left([A]^T\right)^{-1} \vec{H}(\vec{r}) \quad (2.162)$$

$$[\mu'(\vec{r}')] = \frac{[A][\mu(\vec{r})][A]^T}{\det[A]} \quad (2.163)$$

Substituting our functions transforms into Eq. (2.159).

$$\nabla \times \left\{ [A]^T \vec{E}' \right\} = -j\omega \det[A] \left\{ [A]^{-1} [\mu'] \left([A]^T \right)^{-1} \right\} [A]^T \vec{H}' \quad (2.164)$$

Equation (2.164) can be rewritten as

$$\underbrace{\frac{[A](\nabla \times)[A]^T}{\det[A]}}_{\nabla' \times} \vec{E}' = -j\omega[\mu']\vec{H}' \quad (2.165)$$

Which is the as Eq. (2.159), proving that Maxwell's equations are form invariant.

2.7.2 Benchmark Simulations

Using TO and AFDFD, explained in Section 2.5, a lens and electromagnetic cloak were simulated.

2.7.2.1 Scattering from a flat lens for far-zone focusing

Using TO, a flat lens for far-zone focusing was designed in Ref. [50]. The lens effectively converts cylindrical waves into plane waves. The lens was designed by performing the following transform in a standard Cartesian coordinate. The permittivity and permeability tensors are equal to one another so the permeability terms are not written below.

$$\epsilon'_{xx} = \frac{\sqrt{a^2 - x^2} - g}{l} \quad (2.166)$$

$$\epsilon'_{xy} = \epsilon'_{yx} = \frac{x(y - g)}{l\sqrt{a^2 - x^2}} \quad (2.167)$$

$$\epsilon'_{yy} = \frac{1}{\sqrt{a^2 - x^2} - g} \left[\frac{x^2(y - g)^2}{l(a^2 - x^2)} + l \right] \quad (2.168)$$

$$\epsilon'_{zz} = \frac{\sqrt{a^2 - x^2} - g}{l} \quad (2.169)$$

$$\epsilon'_{zx} = \epsilon'_{xz} = \epsilon'_{zy} = \epsilon'_{yz} = 0 \quad (2.170)$$

Where $a = (g^2 + w^2)^{1/2}$. The dimensions used were $w = 0.4$ m, $g = 0.05$ m, and $l = 0.1$ m. The material parameters are shown in Figure 2.7.2.

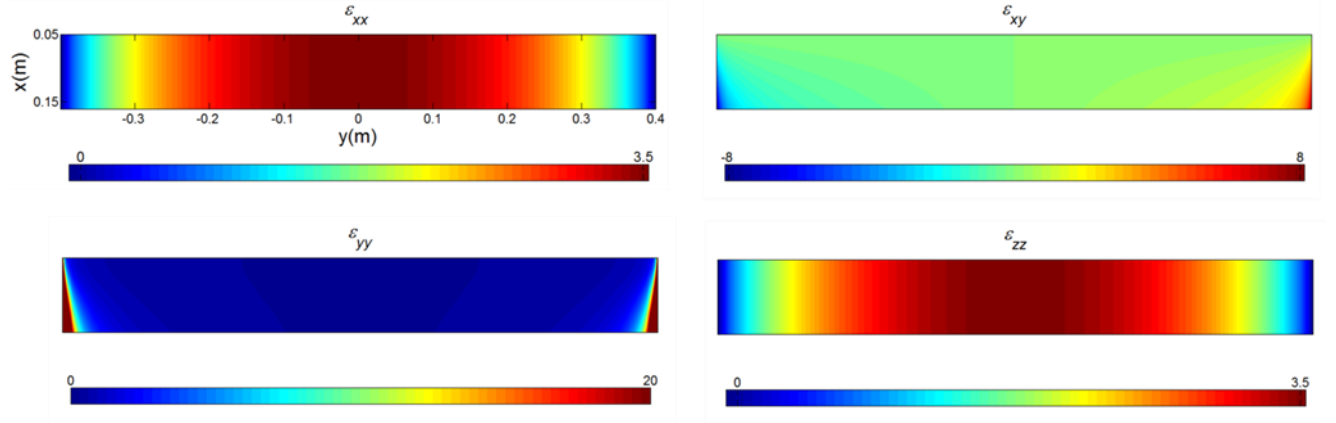


Figure 2.7.2: Material parameters for a far-zone lens

The far zone lens was then simulated using AFDFD. The simulation is shown in Figure 2.7.3. There are UPML's on all four sides of the simulation space. It can be seen that the lens is an effective way of converting a cylindrical wave into plane wave. The simulation very closely matches Ref. [50], but since truncated values were used for the material parameters there are slight reflections at the interface of the cylindrical wave and the lens. Those reflections are the cause of the ripple effect behind the source.

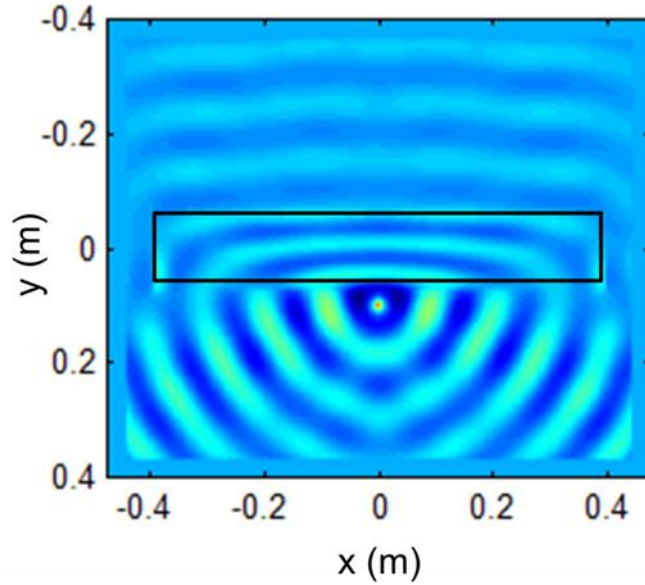


Figure 2.7.3: Simulated far zone lens using AFDFD

2.7.2.3 Scattering from a Cloak

Using TO, cloaks have been designed to work in the microwave region [51] and in the optical region [52]. Using the coordinate transform developed in Ref. [51] a cloak was made using the following coordinate transform in cylindrical coordinate system. The permittivity and permeability tensors are equal to one another so the permeability terms are not written.

$$\varepsilon'_r = \frac{r-a}{r} \quad (2.171)$$

$$\varepsilon'_\theta = \frac{r}{r-a} \quad (2.172)$$

$$\varepsilon'_z = \left(\frac{b}{b-a} \right)^2 \left(\frac{r-a}{r} \right) \quad (2.173)$$

The dimensions used were $a = 20$ cm and $b = 5$ cm. For illustration purpose Eqs. (2.171) - (2.173) were converted into rectangular space and shown in Figure 2.7.4.

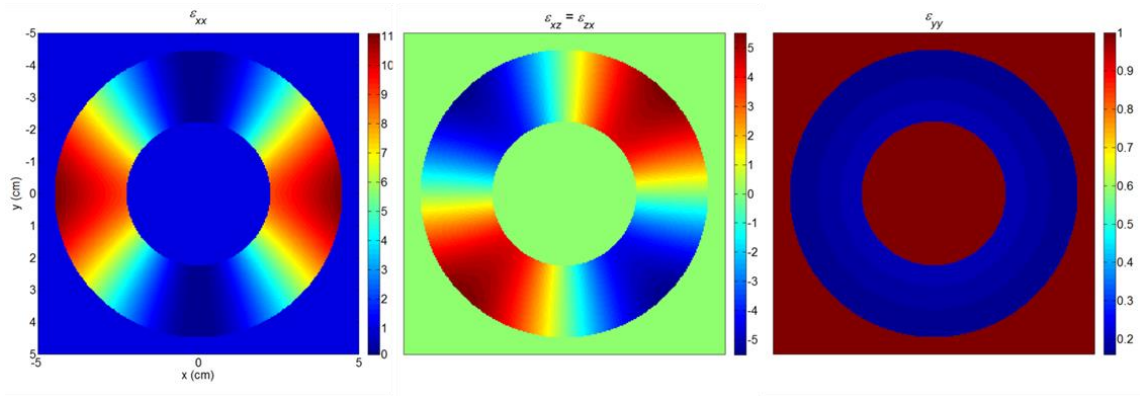


Figure 2.7.4: Material Parameters of Cloak

All other material parameters were equal to zero. It important to note that these are reduced material properties. A standard plane wave was simulated using AFDFD with UMPL's on the top and bottom and Dirichlet boundaries on the other sides. Then the same plane wave was simulated but with the cloak placed in the center of the simulation space. It can be seen in Figure 2.7.5 that the cloak was successfully simulated using AFDFD. The simulations are an exact match to the simulation in Ref. [51].

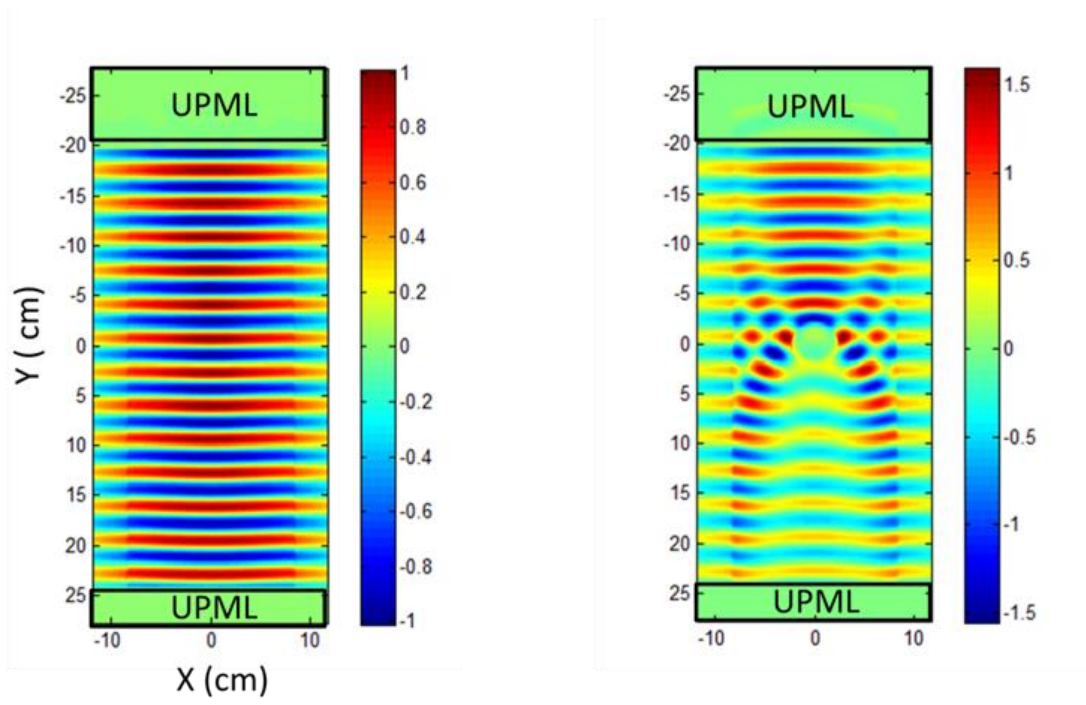


Figure 2.7.5: AFDFD simulation of cloak

Chapter 3: 3D Printing of Anisotropic Metamaterials

This chapter summarizes an artificially anisotropic metamaterial manufactured by 3D printing. First, the design methodology and optimization of a uniaxial metamaterial is discussed. Second, samples were manufactured using FDM and their dielectric tensor properties measured in the lab. The measured results agree well with the model predictions.

3.1 Device Design

The PWEM, derived in section 2.3, was used to predict the effective tensor parameters of the anisotropic metamaterial. The method discretizes Maxwell's equations by expanding the field into a plane wave basis. This is highly efficient for all-dielectric structures with low to moderate dielectric contrast. Retrieving the constitutive parameters was simple because our structures operate in the long wavelength limit where branching [53, 54] does not occur. Given the dielectric function $\varepsilon(\vec{r})$ of the unit cell and a Bloch wave vector $\vec{\beta}$, the PWEM solves Maxwell's equations as an eigen-value problem where the eigen-value is square of the free space wave number k_0^2 . To ensure the model operates in the long wavelength limit, the magnitude of the Bloch wave vector was made very small (i.e. $\beta < 0.1/a$). The effective refractive index of a Bloch wave can be calculated using Eq. (3.1) by dividing the magnitude of the Bloch wave vector by the wave number of the first order band [54].

$$n_{\text{eff}} = |\vec{k}|/k_0 \quad (3.1)$$

In this work, an all-dielectric uniaxial metamaterial was designed. Being uniform in the z -direction, it was possible to model the device using a 2D PWEM code. In this case, Maxwell's equations decouple into two distinct modes, TM and TE. The TE mode has the electric field polarized in the x - y plane while the TM mode has the electric field polarized perpendicular to this plane. The ordinary refractive index n_o was retrieved by using a Bloch wave vector confined to the x - y plane. The direction in this plane was arbitrary due to the structure having uniaxial symmetry. The extraordinary refractive index n_e was retrieved using a Bloch wave vector

parallel to the z -axis. Assuming there was no magnetic response in the bulk material, the dielectric tensor of the metamaterial along the principle axes was

$$\epsilon_{r,\text{eff}} = \begin{bmatrix} n_o^2 & 0 & 0 \\ 0 & n_o^2 & 0 \\ 0 & 0 & n_e^2 \end{bmatrix} \quad (3.2)$$

A systematic study was performed to identify what canonical structures exhibit the greatest anisotropy when using a material with dielectric constant $\epsilon_r = 2.57$. For the optimization, the strength of the anisotropy was defined as the difference between the ordinary and extraordinary dielectric constants.

$$\Delta\epsilon = n_e^2 - n_o^2 \quad (3.3)$$

The study included arrays of holes, arrays of dielectric rods, and different shaped holes and rods. Only square and hexagonal arrays were considered because only these are uniaxial in three dimensions. These combinations are illustrated in Figure 3.1.1. It was found that arrays of dielectric rods in air consistently produced stronger anisotropy than arrays of air holes in dielectric. Further, hexagonal arrays produced stronger anisotropy than square arrays due to the greater packing density of the rods. Of all the combinations, a hexagonal array of hexagonal shaped rods suspended in air provided the strongest anisotropy. Considering ease of design and manufacturing, a hexagonal array of circular rods was the final design. In addition, support features were added in order to produce a final lattice that is free standing and mechanically robust. To minimize their effect, supports were added along only two directions producing a lattice that was weakly biaxial, but still essentially uniaxial.

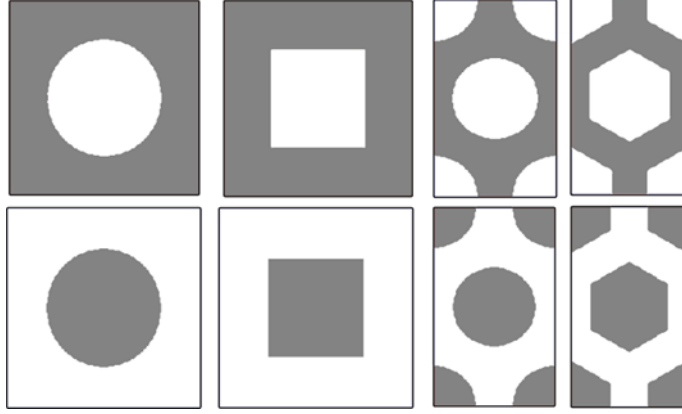


Figure 3.1.1: Pictures of various unit cells simulated

Given the basic design shown in Figure 3.1.2 a double parameter sweep was performed to determine the rod radius and thickness of the supports that optimize the anisotropy. The dielectric was chosen to be polycarbonate (PC) which has a dielectric constant of $\epsilon_r = 2.57$. The baseline unit cell and the data calculated from the double parameters sweep are provided in Figure 3.1.2. It was concluded from this data that the support features should be made as small as possible while still being mechanically robust. The radius of the dielectric rods that optimizes the anisotropy is $0.45a$. Under these conditions, the ordinary and extraordinary dielectric constants were calculated to be $\epsilon_o = 1.9514$ and $\epsilon_e = 2.0525$. This yields a dielectric tensor of

$$\epsilon_{\text{simulated}} = \begin{bmatrix} 1.9514 & 0 & 0 \\ 0 & 1.9514 & 0 \\ 0 & 0 & 2.0525 \end{bmatrix} \quad (3.4)$$

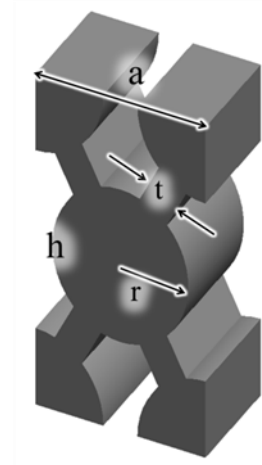
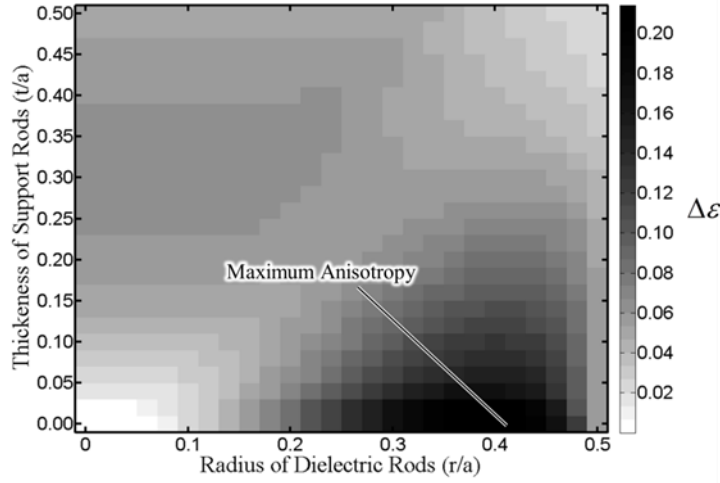


Figure 3.1.2: Double Parameter Sweep of Anisotropic Unit Cell

3.2 Experimental Results

The final design dimensions were $a = 8.0$ mm, $r = 6.4$ mm, $h = 13.86$ mm, and $t = 1.8$ mm. The thickness of the rods t was determined by printing various test structures while shrinking the thickness each time until the mechanical integrity was no longer acceptable. The final device was manufactured by FDM. FDM was chosen because it could handle the feature size and the current materials it uses have less loss than other 3D printing methods. First, a bulk sample of the PC material was printed and the dielectric constant was measured in the L-band (1.7–2.6 GHz) to be $\epsilon_r = 2.57$ with a loss tangent of $\tan \delta = 0.02$. To measure the three tensor components of the metamaterial, three samples were printed in three orientations. The form factor was chosen to fit perfectly into a rectangular L-band waveguide with the dimensions of $109.22 \text{ mm} \times 54.61 \text{ mm} \times 35.56 \text{ mm}$. A photograph of these samples are shown in Figure 3.2.1.

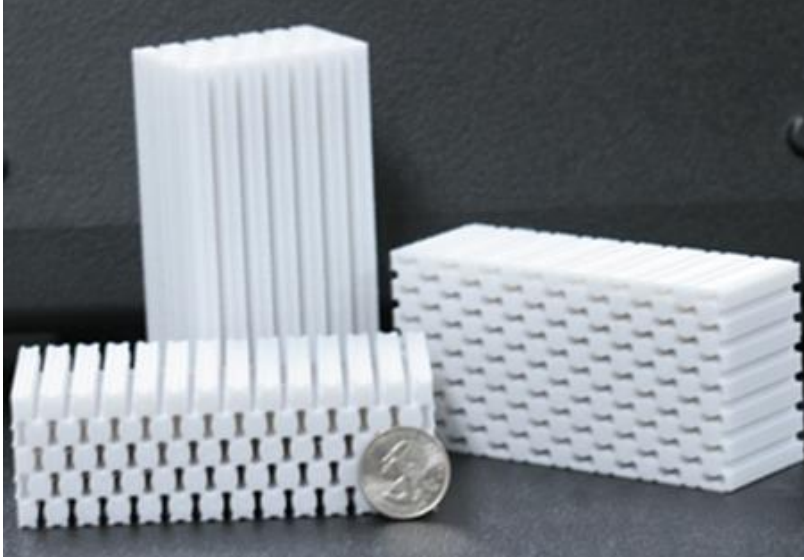


Figure 3.2.1: Manufactured Anisotropic Metamaterials

Each sample was tested using the materials measurement software installed on an Agilent N5245 PNA-X vector network analyzer (VNA). The transmission line method was selected for parameter retrieval [55] so the samples were inserted into a waveguide section and measured separately as shown in Figure 3.2.2. The dielectric constant of the x and y orientations should be equal because the metamaterial was uniaxial, but a small deviation in the symmetry was introduced during the manufacturing of about 1.25% which is attributed to small deformation in the manufacturing. The final dimensions of the printed unit cell were $a = 8.1$ mm, $r = 6.5$ mm, $h = 13.8$ mm, and $t = 1.8$ mm.

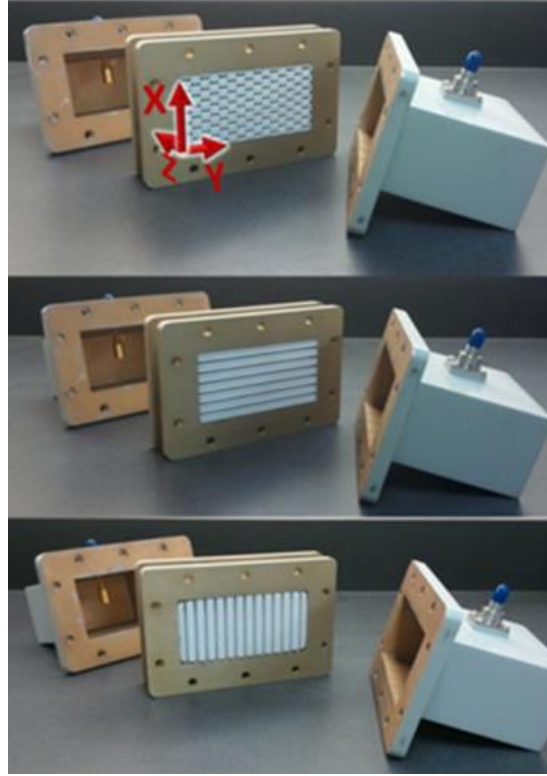


Figure 3.2.2: Materials under test. (Top) Rods in the z -direction. (Middle) Rods in the y -direction. (Bottom) Rods in the x -direction

The measured data over the L-band is provided in Figure 3.2.3. As anticipated, the x and y orientations were similar and the z orientation produced the largest effective dielectric constant. The measurements showed a sharp spike at the high frequency side of the spectrum. This is where the frequency is high enough for the resonant effects to become significant. This represents the upper frequency cutoff of the metamaterial. The cutoff frequency can be moved to a higher frequency by reducing the lattice constant.

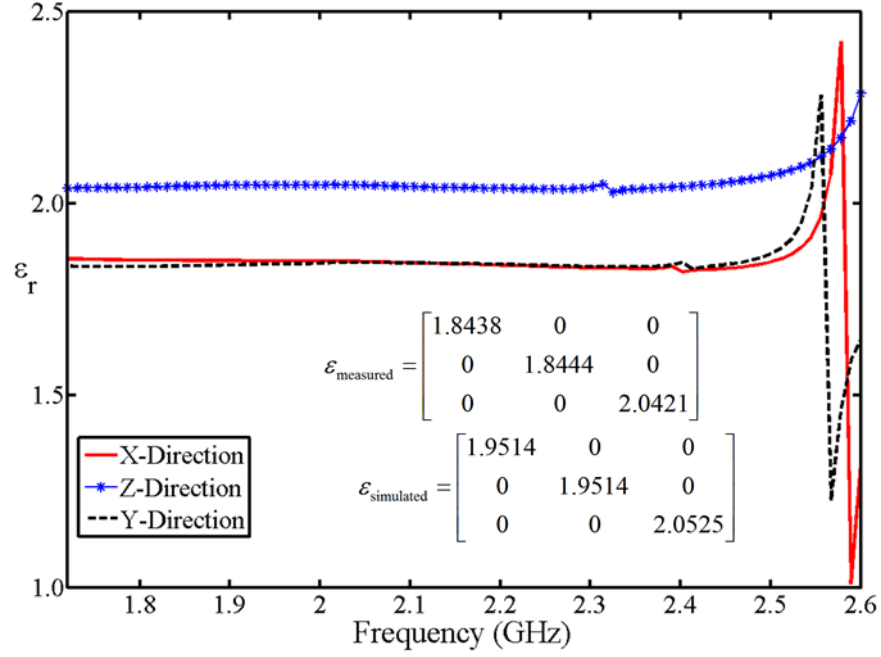


Figure 3.2.3: Measured dielectric tensor

3.3 Conclusions

An all-dielectric uniaxial anisotropic metamaterial was successfully designed, fabricated, and tested. It was manufactured from polycarbonate using a form of 3D printing called fused deposition modeling. The full dielectric tensor was measured in the lab and the experimental results corresponded well to the measured results.

Chapter 4: Electromagnetic Isolation of A Microstrip by Embedding in a Spatially Variant Anisotropic Metamaterial

The numerical tool, described in section 2.4, was used to study how the field surrounding a microstrip transmission line can be sculpted by embedding it in a SVAM. The impact of the strength of the anisotropy as well as the orientation of the spatial variance was studied. Based on these findings, the concept was demonstrated experimentally by isolating a microstrip transmission line from a metal object placed in close proximity by embedding it in a specifically designed SVAM.

4.1 Microstrip embedded in anisotropic media

First, a series of simulations was performed to study the effect of the strength of the anisotropy, or birefringence, of the dielectric medium. Birefringence is defined as $\Delta\epsilon = \epsilon_{xx} - \epsilon_{yy}$ when the crystal axes are chosen so that the tensor is diagonal. The results of this analysis are provided in Figure 4.1.1. The distributed inductance was not affected because the electrostatic approximation decouples the magnetic field from the electric field. The distributed capacitance increased as the dielectric constant of the ϵ_{yy} tensor element was increased. This lowered the impedance of the transmission line as expected from Eq. (2.85). The shape of the field was also affected by the increasing anisotropy. After observing the trend in Figure 4.1.2, we conclude that the field does tend to develop along the axis with the highest dielectric constant. Here, the field developed more strongly in the vertical direction because $\epsilon_{yy} > \epsilon_{xx}$. The degree to which this occurs was observed to be proportional to the birefringence.

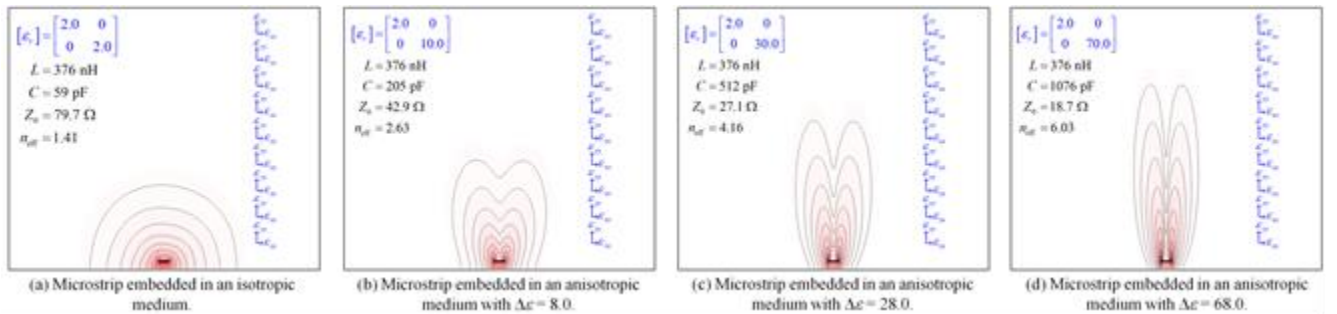


Figure 4.1.1: Study on the effect of the strength of the anisotropy of the surrounding medium

Next, the effect of spatially varying the orientation of the anisotropy was studied in a series of simulations summarized in Figure 4.1.2. The first device was the same microstrip modeled previously, but with the dielectric constant set to 2.0. The second device was a transmission line embedded in an anisotropic medium with $\epsilon_{xx} = 2.0$ and $\epsilon_{yy} = 70.0$. The impedance of the line changed significantly after embedding it in a SVAM, so it was concluded that transmission lines must be designed to be embedded. The shape of the field responded consistent with the discussion around Figure 4.1.1. For the third device shown in Figure 4.1.2(c), the orientation of the anisotropy around the transmission line was tilted to the left by 60° . Consistent with the discussion above, the field shifted in this new direction. The impedance of the line increased somewhat due to the tilt. In the final device shown in Figure 4.1.2(d), the orientation of the anisotropy was spatially varied and the field still followed the anisotropy through the spatial variance. The impedance of this line changed only very slightly. This suggests that after a device is designed to be embedded in an anisotropic medium, the near-field can be arbitrarily sculpted using spatially variant anisotropy with minimal impact on the properties of the line.

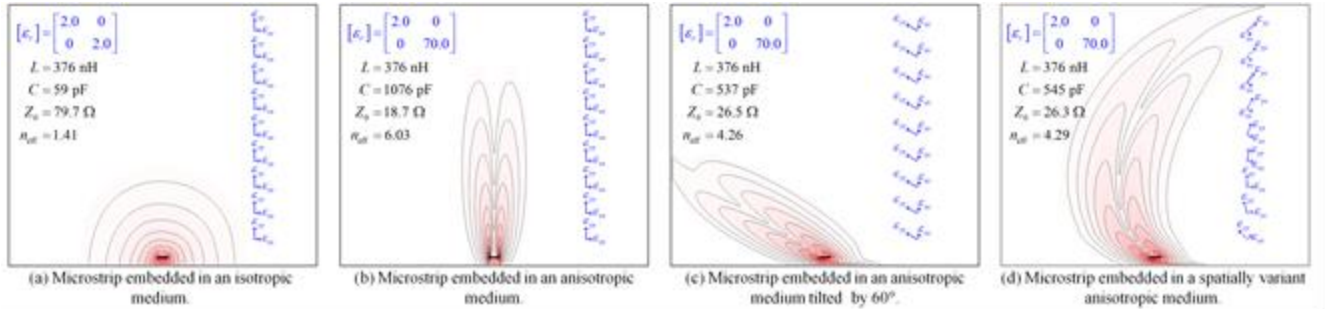


Figure 4.1.2: Study on the effect of the strength of spatially varying the anisotropy of the surrounding medium

To prove the concept in a more rigorous manner, a series of simulations was performed using Ansys HFSS™, which is a 3D full-wave electromagnetic field solver. A standard 50Ω microstrip transmission line was designed on Rogers RT/Duroid®. The line was simulated with and without a metal ball placed in close proximity. Cross sections of the field from these

simulations are shown in Figure 4.1.3. These show that the near-field of the transmission line shifts toward the metal ball when it is introduced.

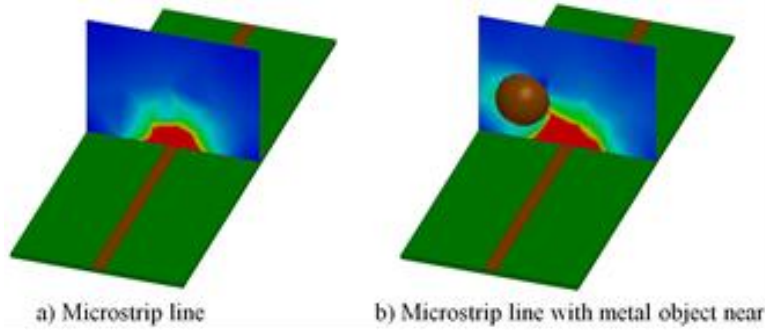


Figure 4.1.3: Rigorous 3D simulation of standard microstrip transmission line with and without a metal ball placed in close proximity.

Next, the microstrip was embedded in a SVAM where the anisotropy was rotated from the surface normal by 60° away from the metal ball. This was done to shift the field away from the ball so that its presence would not be felt by the microstrip. Cross sections of the field from these simulations are shown in Figure 4.1.4. In this case, the presence of the ball had much less effect on the shape of the near field, confirming our concept.

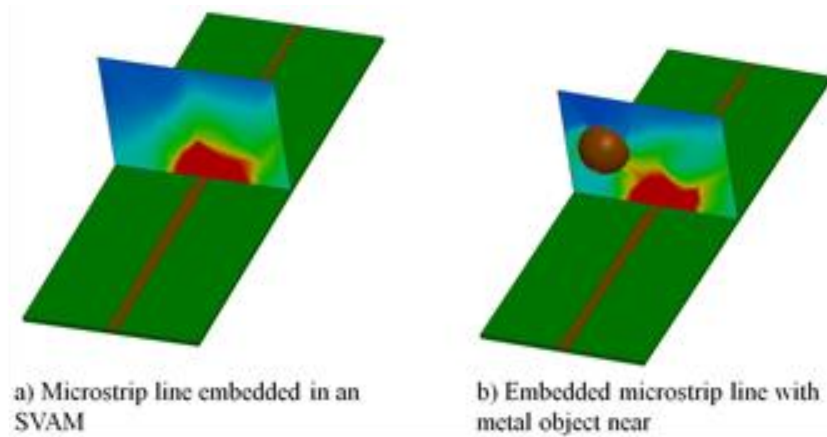


Figure 4.1.4: Rigorous 3D simulation of standard microstrip transmission line with and without a metal ball placed in close proximity.

4.2 Device Design

First, an all-dielectric uniaxial metamaterial was designed to provide the required anisotropy. It was a square array of high dielectric constant cylinders embedded in a low

dielectric constant medium. This geometry was chosen because it is known to provide stronger anisotropy as shown in Section 3.1.2. The SVAM was composed of PC thermoplastic backfilled with titanium dioxide (TiO₂) nano-powder. The dielectric constant of the PC was measured to be 2.33. The dielectric constant of the TiO₂ powder was estimated to be 40 using the Bruggeman model [56] and assuming the packing density was about 64% by volume [57]. Based on these dielectric constants, the dielectric tensor can be quickly estimated using the Weiner bounds [58].

$$[\epsilon_r] = \begin{bmatrix} \epsilon_{xx} & 0 & 0 \\ 0 & \epsilon_{yy} & 0 \\ 0 & 0 & \epsilon_{zz} \end{bmatrix} \quad (4.1)$$

$$\frac{1}{\epsilon_{xx}} = \frac{1}{\epsilon_{zz}} = \frac{f_o}{\epsilon_{r1}} + \frac{1-f_o}{\epsilon_{r2}} \quad (4.2)$$

$$\epsilon_{yy} = f_e \epsilon_{r1} + (1-f_e) \epsilon_{r2} \quad (4.3)$$

With optimized dimensions, the weight terms in the above equations are $f_o \cong 0.72$ and $f_e \cong 0.72$ leading to values of $\epsilon_{xx} = 7.24$ and $\epsilon_{yy} = 24.55$. Rigorous values were obtained by modeling the unit cell with the PWEM shown in Section 2.3. Using the PWEM, the dimensions were optimized to maximize the birefringence. The lattice spacing a should be much less than $\lambda/4$ to ensure the lattice is not resonant. In practice, this dimension should be made as small as possible so that the geometry of the unit cell still forms well after manufacturing. The optimum diameter of the cylinder was found to be $d = 0.84a$. This result is valid essentially independent of the choice of ϵ_{r1} and ϵ_{r2} . The resulting unit cell, shown in Figure 4.2.1, was predicted to have $\epsilon_{xx} = 7.29$ and $\epsilon_{yy} = 24.15$.

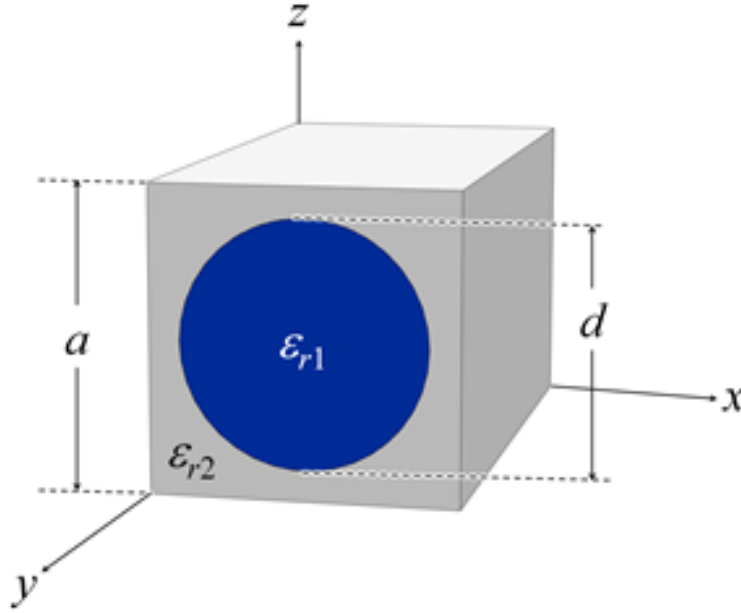


Figure 4.2.1: Cross section of the unit cell. For $\epsilon_{r1} = 40$ and $\epsilon_{r2} = 2.33$, the optimized ratio d/a is 0.8.

The SVAM was designed so that it could be placed on top of an otherwise ordinary microstrip. It was tapered at either end of the device to provide a smoother transition of impedance from the bare microstrip into the SVAM region. A small hole was formed through the device so that a metal ball could be inserted and located to within 2 mm of the microstrip. A computer model of the SVAM is shown in Figure 4.2.2.

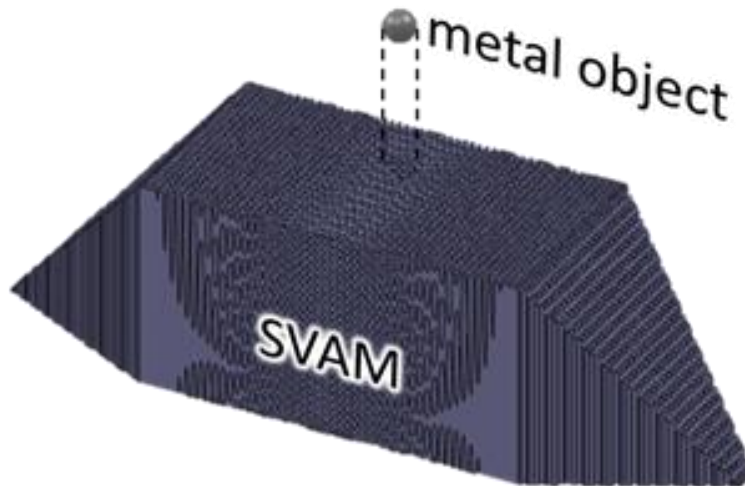


Figure 4.2.2: SVAM to be placed on top of an otherwise ordinary microstrip

With the cylinders oriented vertically, the near-field around the line would develop vertically as shown in Figure 4.2.1(b). To move the field away from the ball, the cylinders were tilted away from the ball to an angle of 60° following a Gaussian profile. The device and the change in the orientation of the anisotropy is illustrated in Figure 4.2.3. For this simple design, it was not necessary to employ a more sophisticated design technique like transformation optics shown in Section 2.7, but it is certainly possible to do this.

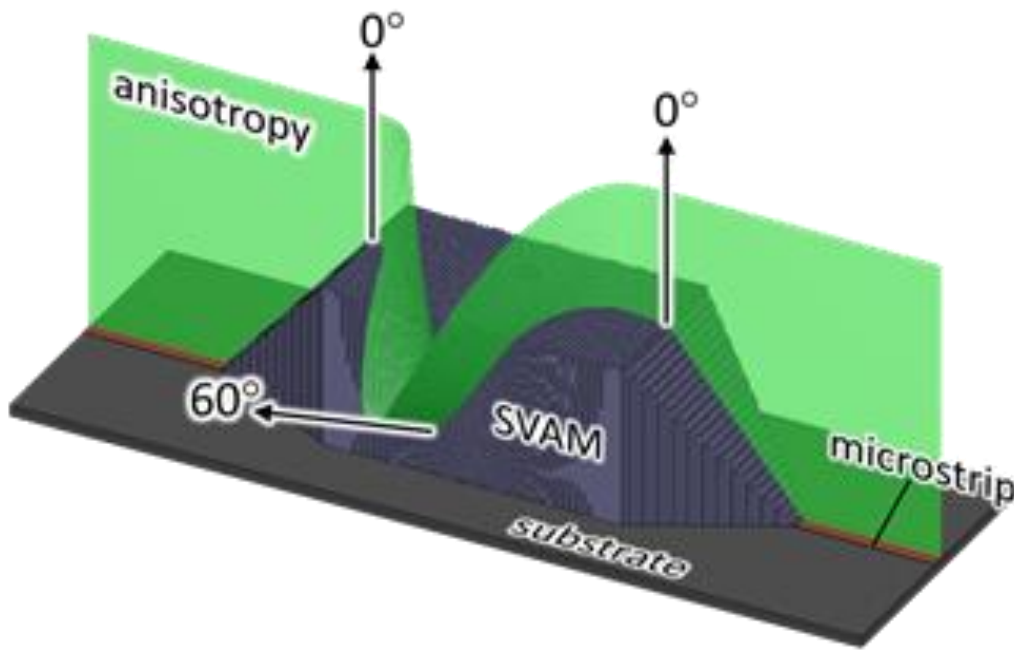


Figure 4.2.3: Orientation of the anisotropy of the SVAM

In order to spatially vary the orientation of the unit cells throughout a lattice without changing the size and shape of the unit cells, using the SVL tool shown in Section 2.6.

4.3 Experimental Results

The SVAM was manufactured by FDM. FDM was chosen because it had the resolution to print the SVAM and the materials used in this process have lower loss than other 3D printing methods. Several small test samples were printed to assess the minimum diameter of the holes so that they would form well in the final device. This was determined to be 2.0 mm.

Photographs of the finished device are shown in Figure 4.3.1. In this device, the density of the holes is uniform. The density of the holes appears different throughout the device only because their orientation has been spatially varied and the device is shown from two different perspectives.

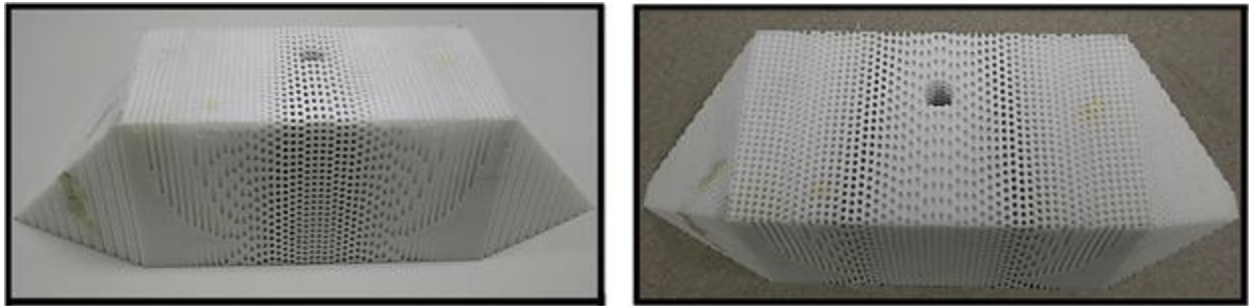


Figure 4.3.1: 3D printed spatially variant anisotropic metamaterial

Next, the holes were packed with the TiO_2 nano-powder. TiO_2 was chosen because it has a dielectric constant of around 40 at the operating frequency. First, a long wavelength vibrating table was used to shake the powder down into the holes. This achieved about a 95% fill. Second, the device was placed in an ultrasonicator to densify the powder. The remaining voids were filled by hand and then the device was placed back into the ultrasonicator one last time. Photographs of the packed SVAM are shown in Figure 4.3.2. The long term vision for this technology is to manufacture the entire circuit and SVAM completely by 3D printing. At present, no high dielectric constant material is commercially available for 3D printing so the TiO_2 powder was used instead.

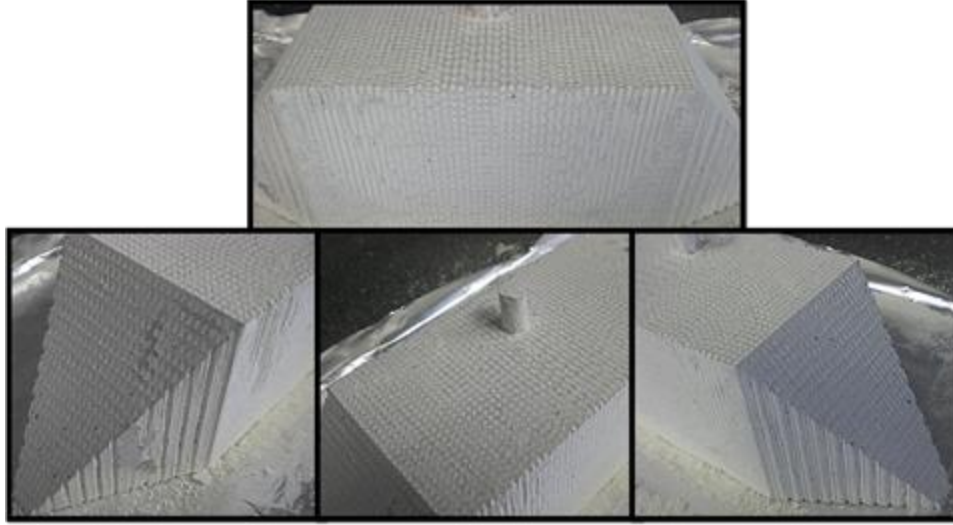


Figure 4.3.2: SVAM packed with TiO_2 nano-powder

To test the SVAM, a microstrip transmission line was designed specifically to be placed under the SVAM. The microstrip transmission was built on a piece of cardboard and designed to be 50 ohms. The width of the line was made to be 10 mm so that it would be large relative to the periodic structure of the metamaterial. In practice, the SVAMs would be 3D printed with much finer dimensions so they can function around transmission lines having more typical dimensions. The microstrip was placed onto a cardboard substrate that was 2.8 mm thick. A ground plane was placed under the cardboard. Pictures of the microstrip with and without the SVAM in place are shown in Figure 4.3.3.



Figure 4.3.3: Microstrip transmission line in test setup, with and without the SVAM in place

The scattering parameters from the transmission line were measured using an Agilent N5245 PNA-X vector network analyzer. The data is shown in Figure 4.3.4. Little was done to match impedance so the return loss from the bare microstrip averaged around -15 dB. The dips in this spectrum arose from the Fabry-Perot resonance established between the connectors at either end of the line. When the SVAM was inserted, the spectrum shifted and reflection dropped by around 4 dB on the low frequency side. It is important to note that this data only shows the background reflection from the bare microstrip and SVAM. No metal ball was involved in these measurements.

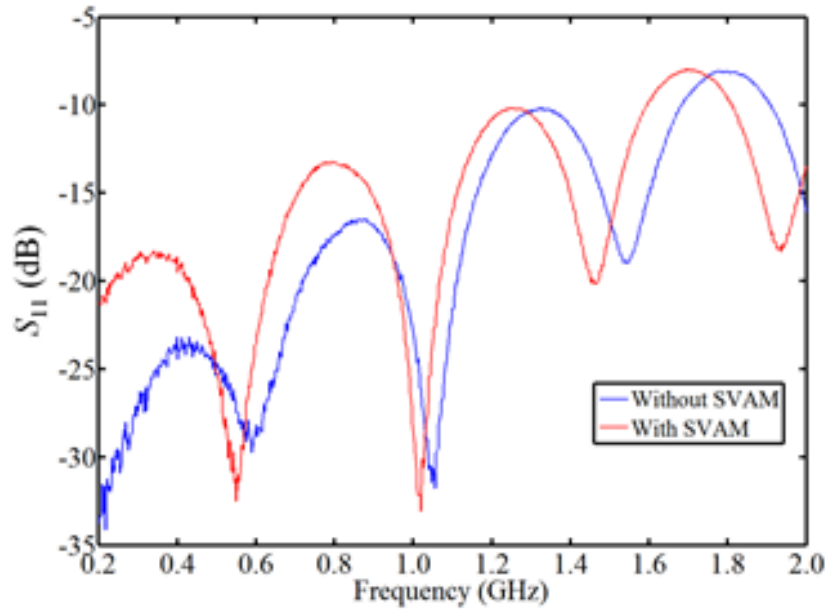


Figure 4.3.4: Reflection from the bare microstrip, with and without the SVAM in place

From here, the scattering parameters of the microstrip were measured with and without the metal ball in place. The return loss of the microstrip and the insertion loss of the SVAM itself were calibrated out of the measurements so that only the effects of the metal ball were measured. The resulting change in S_{11} , with and without the ball in place, is plotted as a solid blue line in Figure 4.3.5. Fluctuations approaching 8 dB were measured. This same procedure was repeated, but with the SVAM in place. The change in S_{11} is plotted as a dashed red line in this same figure. For the second case, virtually no change in S_{11} was detected because the

SVAM sculpted the field away from the ball. Fluctuations in this second curve were less than 0.5 dB.

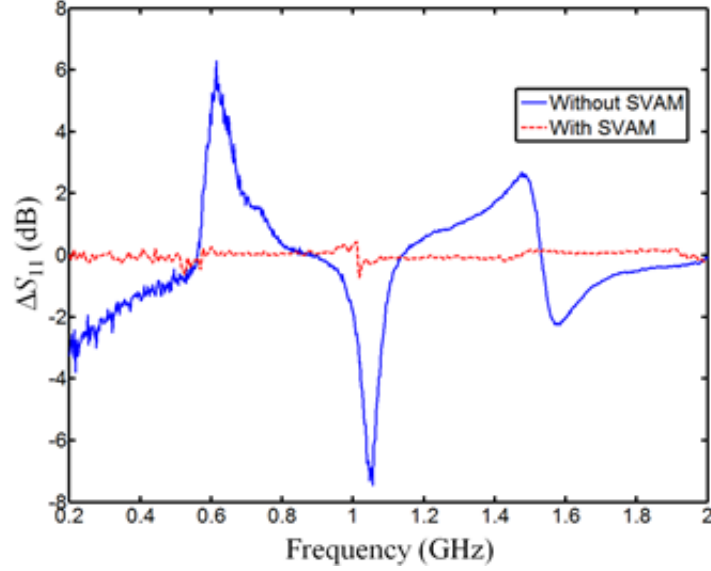


Figure 4.3.5: Change in S11 as ball is placed and removed for two cases: (1) solid blue line is for the microstrip in air, and (2) dashed red line is for the microstrip embedded in the SVAM.

4.4 Conclusions

For the first time, spatially variant anisotropic metamaterials were used as means to sculpt the near-field around devices. To begin this study a simple but powerful technique to study transmission lines embedded in spatially variant anisotropic media was outlined. This model was used to show that the near-field can be sculpted almost arbitrarily with minimal change to the properties of the device itself. This conclusion was confirmed with a rigorous 3D model. Based on these results, a microstrip transmission line was isolated from a metal ball placed in close proximity by embedding the line in a SVAM. The presence of the SVAM virtually eliminated any interference of the ball on the microstrip, confirming the novel concept to manage fields in 3D printed systems

Chapter 5: Effects of Extreme Surface Roughness on a 3D Printed Horn Antenna

This chapter summarizes the design and experimental verification of a 3D printed horn antenna. Electron beam melting (EBM) [59-61] and selective laser melting [62, 63] are dominant methods for printing metal structures. A drawback of many 3D printing technologies is rough surface finish. In EBM, an electron beam is used to melt and fuse together metal particles in a powder bed. The surface finish from EBM is highly dependent on the particle size, but the powders can become explosive when the particle size is too small. This leads to a surface roughness on the order of tens of microns. It is known that rough finish on metal parts can seriously degrade the electromagnetic performance [64-66]. In this section, the effect of the surface roughness from EBM by comparing 3D printed horn antennas to a standard gain horn antenna sold by Pasternack is evaluated.

5.1 Device and Manufacturing

Two horn antennas were designed in SolidWorks to work in the Ku-band (12-15 GHz) region. Only the horn was printed; the coax-to-waveguide adaptor was not. Photographs of the devices are provided in Figure 5.1.1.

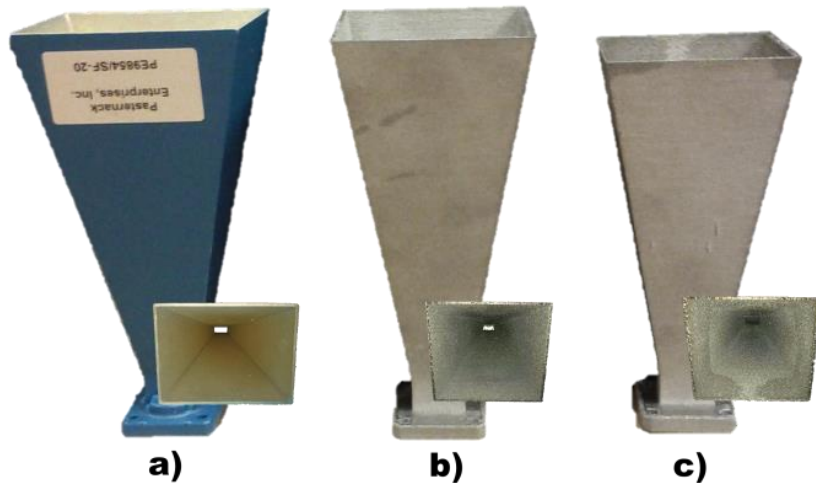


Figure 5.1.1: (a) Reference horn, (b) 3D printed horn #1, (c) 3D printed horn #2.

In order to evaluate the effect of surface roughness, nothing was done during the production to minimize surface roughness. The surface roughness of the finished parts was measured to be $25.9\text{ }\mu\text{m}$ (RMS) for antenna #1 and $39.7\text{ }\mu\text{m}$ (RMS) for antenna #2. The surface roughness was measured with a KLA-Tencor AlphaStep Profilometer. No post-processing steps were taken to polish or otherwise improve the surface finish. All of the dimensions around the feed were made identical, but the antennas differed slightly in the width of aperture, resulting in devices with slightly different directivity and gain. The dimensions of the antennas are illustrated in Figure 5.1.2 and the values are summarized in Table 5.1.1.

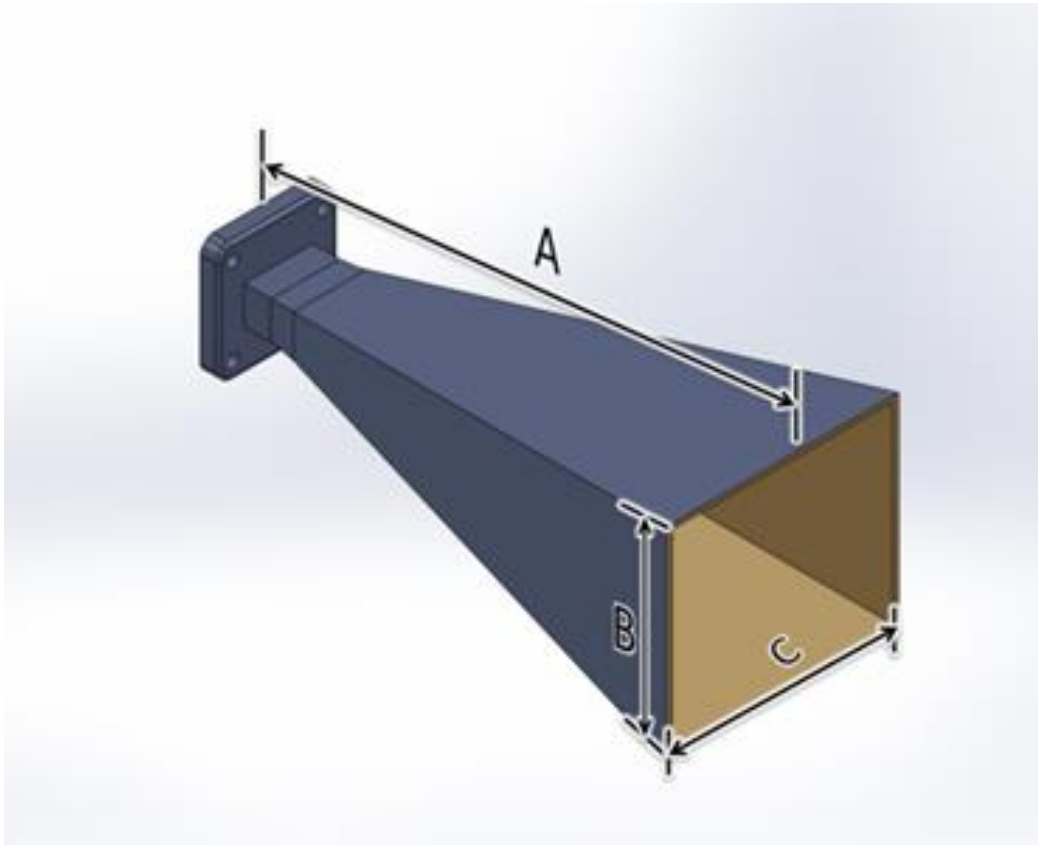


Figure 5.1.2: Geometry of horn antennas

Table 5.1.1: Measured lengths of horn antennas

Name	A (mm)	B (mm)	C (mm)
Reference Horn	145.1	52.8	71.3
3D Printed Horn #1	145.1	52.8	66.2
3D Printed Horn #2	131.9	47.3	55.2

All three antennas were simulated using Ansys HFSS without any surface roughness, and the results are shown in Table 5.1.2.

Table 5.1.2: Simulated and measured gain at 15 GHz at normal incidence

Name	Simulated Gain (dBi)	Measured Gain (dBi)
Reference Horn	19.56	20.00
3D Printed Horn #1	18.98	19.02
3D Printed Horn #2	18.42	17.78

5.2 Experimental Results

All three antennas were calibrated and tested in our anechoic facility. Each antenna was used on the transmit side and made to transmit a signal over a distance of 1.2 meters. The receiving antenna was a Pasternack© standard gain WR62 20 dB horn antenna. The transmission, S_{21} , through this simple setup was measured using an Agilent N5246 PNA-X vector network analyzer. A photograph of the experimental setup is shown in Figure 5.2.1. The measured transmittance for all three antennas is plotted in Figure 5.2.2.

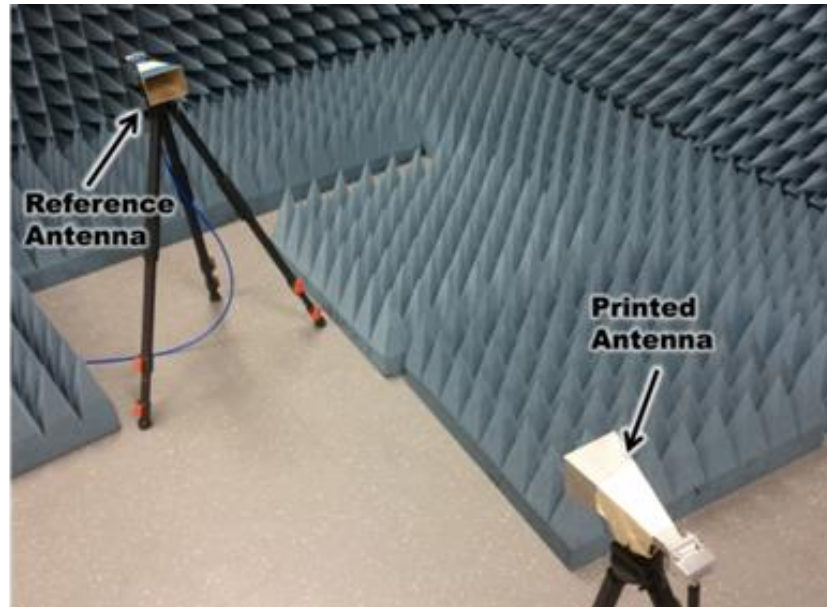


Figure 5.2.1: Experimental Setup

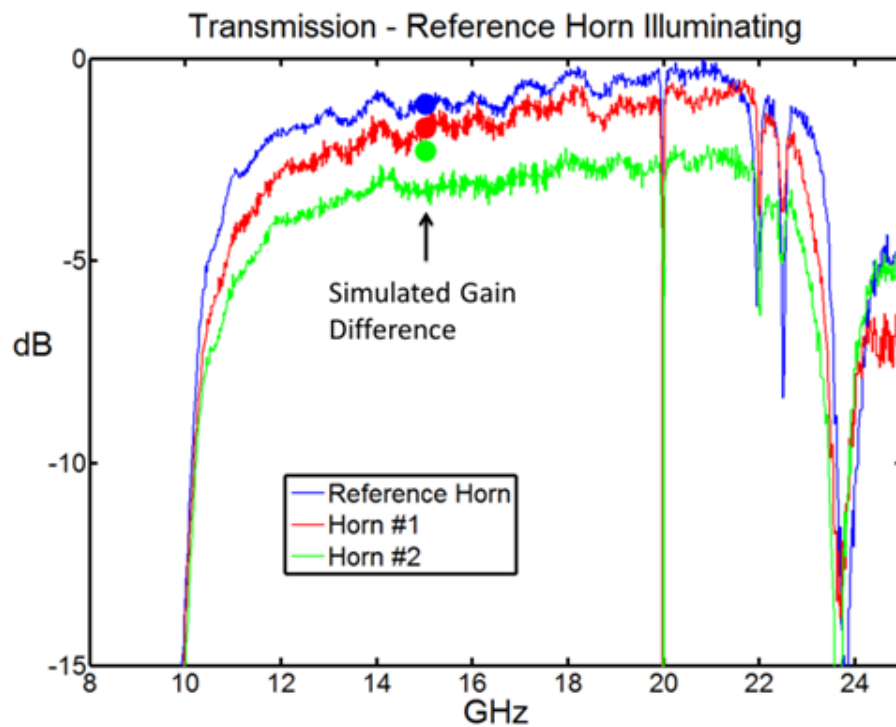


Figure 5.2.2: Measured transmission

The transmission from the first two horns matched the simulations of “perfect” horns extremely well, while the third differed by about 1 dB. Figure 5.2.2 includes an overlay of the difference of the simulated transmittances from each of the antennas at 15.0 GHz. This implies

that the difference in the S_{21} measurements between the reference horn and horn #1 was due to their different directivities and not the surface roughness. Horn #2, which had a much rougher surface than horn #1, experienced around a 1 dB loss, which was attributed to the surface roughness.

5.4 Conclusions

To evaluate the impact of surface roughness resulting from 3D printing of metals, two Ku-band horn antennas were 3D printed using EBM. No post-processing steps were taken to polish or otherwise improve the surface finish, which was measured to be on the order of 20 to 40 microns. The antennas were experimentally tested and compared to a standard horn antenna purchased from Pasternack. It was observed that the surface roughness of horn #1 (25.9 μm RMS) had no measurable effect on the performance. Horn #2 had almost twice the surface roughness (39.7 μm RMS) and measured a 1 dB loss.

Chapter 6: Electromagnetic Isolation of Cell Phone Antennas by Embedding in a Spatially Variant Anisotropic Metamaterial

A SVAM was built into a cell phone case to reduce the electromagnetic interaction of two cell phone antennas placed in close proximity. The antennas were designed and simulated in HFSS and the SVAM decreased the envelope correlation coefficient (ECC) dramatically.

6.1 Envelope Correlation Coefficient

The envelope correlation coefficient (ECC), ρ_e , is the standard way to assess the degree to which multiple antennas are coupled. When the ECC is large, the capacity of the system may decrease [67]. There are two major ways to calculate the ECC. The most accurate way requires the 3D field radiation pattern [25, 26, 67, 68]. The formula for calculating the ECC with the 3D radiation is provided in Eq. (6.1).

$$\rho_e = \frac{\left| \iint_{4\pi} \vec{F}_1(\theta, \phi) \bullet \vec{F}_2^*(\theta, \phi) d\Omega \right|^2}{\iint_{4\pi} \left| \vec{F}_1(\theta, \phi) \right|^2 d\Omega \iint_{4\pi} \left| \vec{F}_2(\theta, \phi) \right|^2 d\Omega} \quad (6.1)$$

$\vec{F}_i(\theta, \phi)$ is the 3D field radiation pattern of the system when port i is excited, all other port are perfectly matched, and \bullet denotes a Hermitian product [68]. An easier way to calculate the ECC is by using the scattering parameters. It is not as accurate as Eq. (6.1), but is widely accepted as a method to obtain the ECC [22-24, 68]. The formula for calculating the ECC with scattering parameters is shown in Eq. (6.2).

$$\rho_e = \frac{\left| S_{11}^* S_{12} + S_{21}^* \right|^2}{\left(1 - |S_{11}|^2 - |S_{21}|^2 \right) \left(1 - |S_{22}|^2 - |S_{12}|^2 \right)} \quad (6.2)$$

The $*$ denotes a complex conjugate operation.

An ECC of 0.5 is considered to be the borderline between a poor antenna system and good antenna system. The antenna system is considered to be working better the closer the ECC is to zero [68, 69].

6.2 Cell Phone Antenna Design

A typical inverted-F antenna (IFA) was designed to work at 740 MHz when embedded in the middle of a 10 mm cell phone case. The manufacturing method identified for this work is SL because it is capable of printing the needed resolution. 740 MHz was chosen because it is close the currently active cellular frequencies of United States cell phone providers. IFA's can easily be tuned to work at virtually any desired frequency [70]. . The design is shown in Figure 6.1.

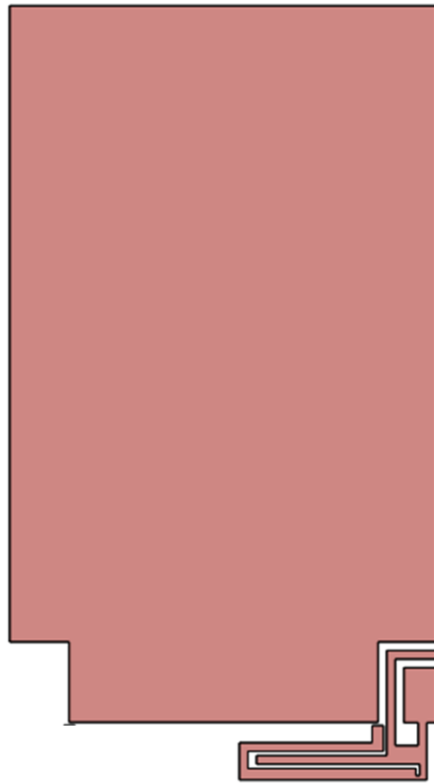


Figure 6.1.1: One IFA design

The IFA was drawn in SolidWorks and then simulated in HFSS. The results are shown in Figure 6.1.2.

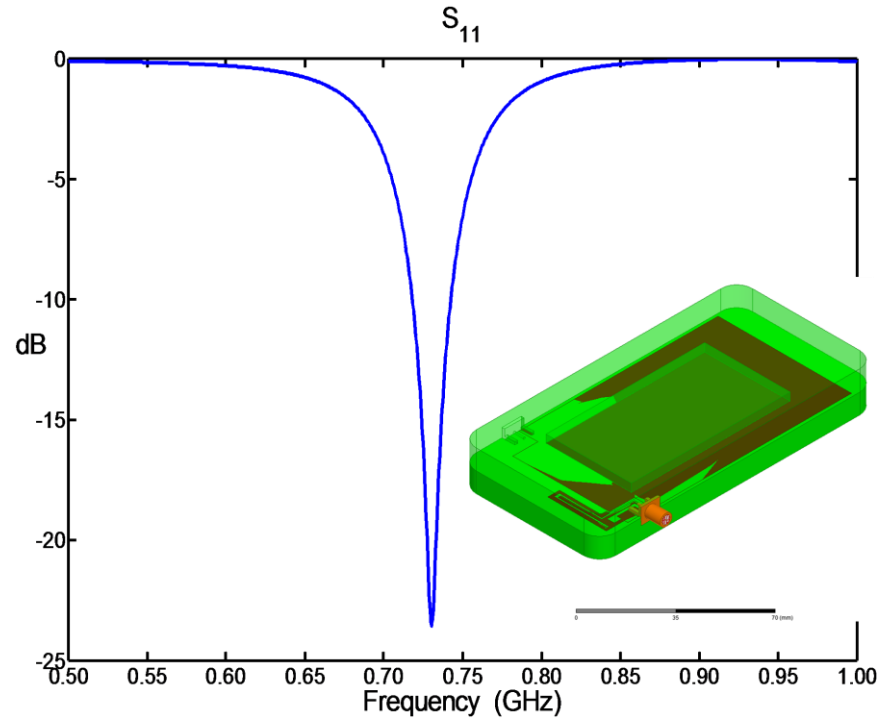


Figure 6.1.2: Simulated IFA

A rule-of-thumb is that an antenna is considered to be resonating if the return loss, S_{11} , is lower than -10 dB. Figure 6.1.2 shows that the IFA is resonating at 740 MHz with a return loss of -24 dB. The 3D field radiation pattern is shown in Figure 6.2.3.

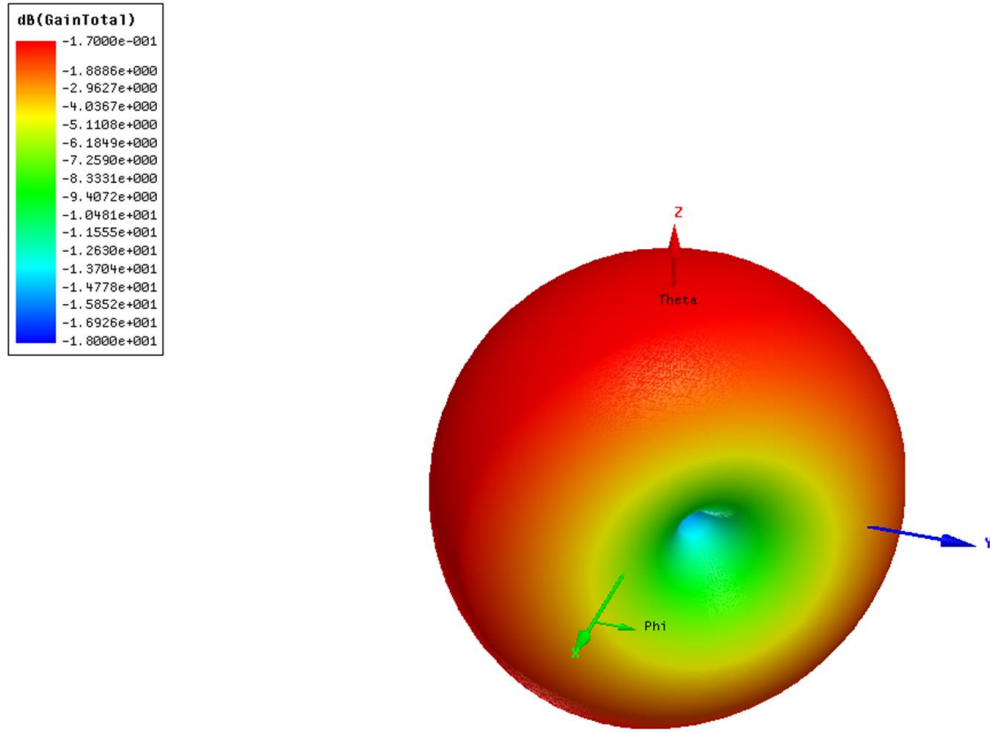


Figure 6.2.3: 3D field radiation pattern of IFA at 740 MHz

6.3 Effects of Second Antenna

The first IFA was mirrored on to the other side and simulated to assess the effects of introducing a second IFA antenna on to the first IFA. The two IFA design is shown in Figure 6.3.1. The simulated results are shown in Figure 6.3.2.

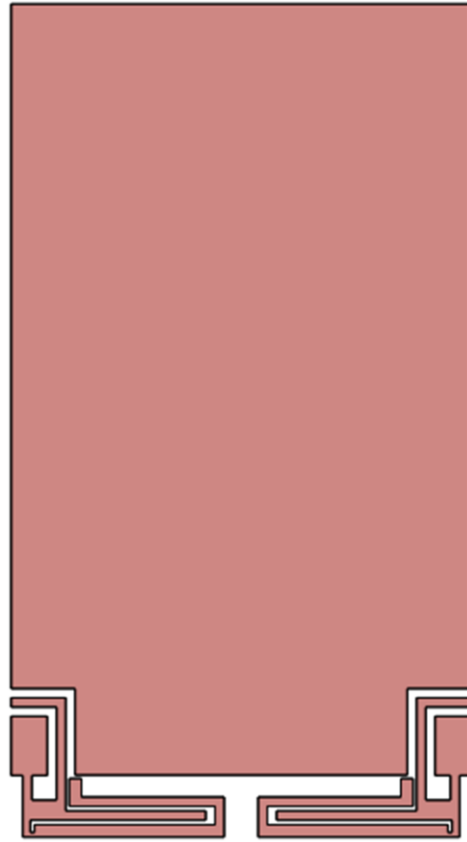


Figure 6.3.1: Two IFA design

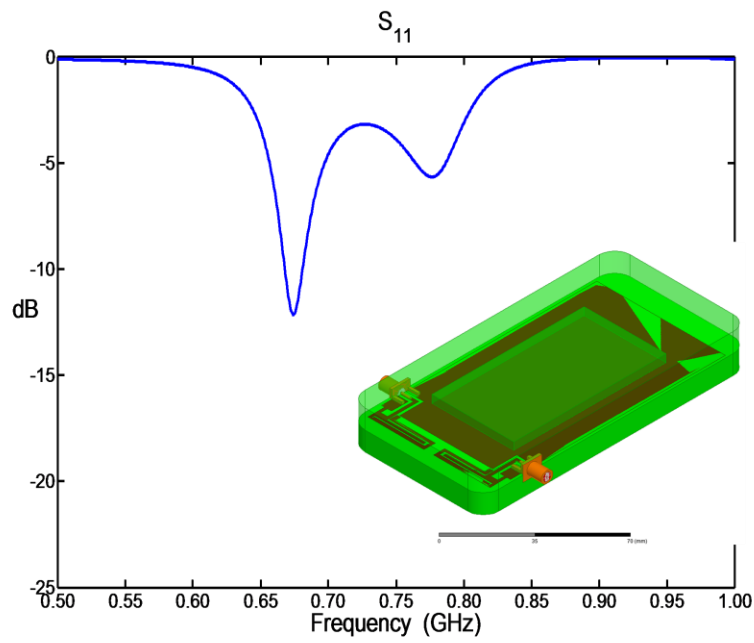


Figure 6.3.2: Simulated two antenna design

Figure 6.3.2 shows that the introduction of the second IFA significantly decreases the performance of the first antenna. The main resonance shifts to a lower frequency because the antenna is not electrically larger and the return loss is much weaker. There is also an introduction of a second resonance. The degradation in the performance is attributed to the electromagnetic coupling of the two IFA's. By looking at the near-field it becomes apparent that they are coupled. The near-field was calculated on a cross section where the fields were most intense, the center of the two IFA's. The near-field is shown in Figure 6.3.3.

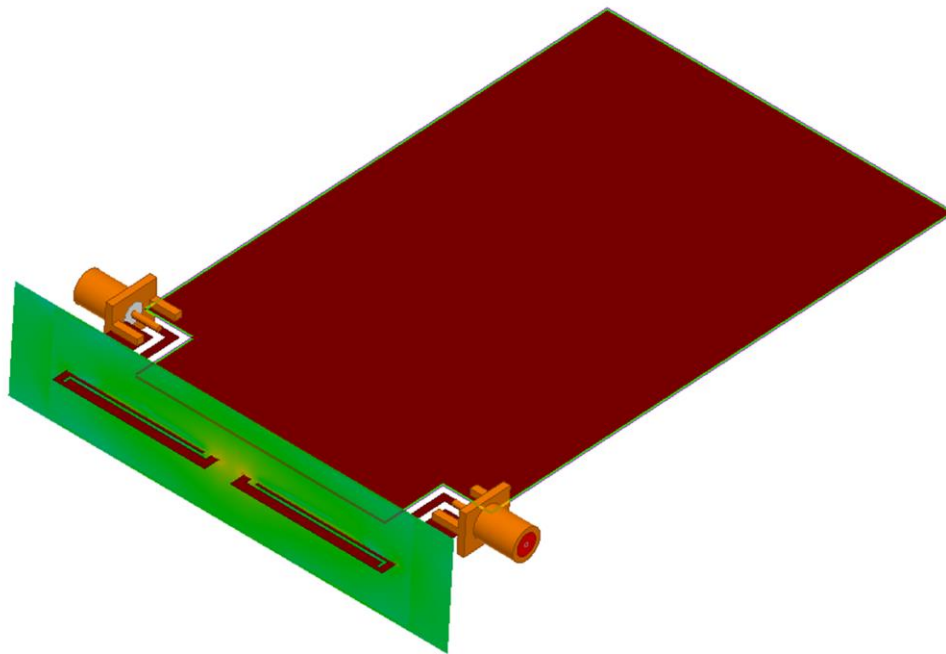


Figure 6.3.3: Near-field of two IFA's

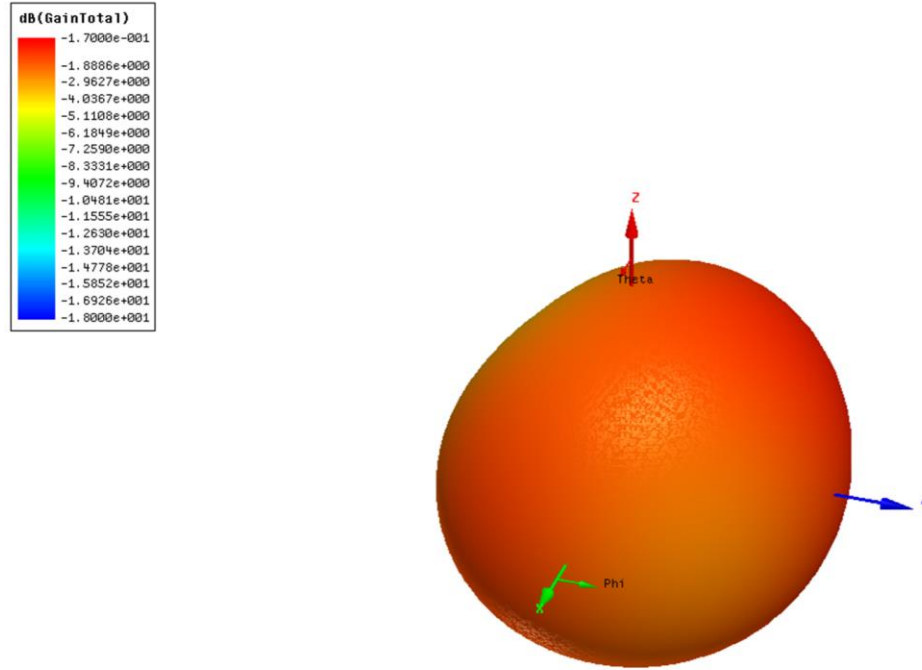


Figure: 6.3.4: 3D field radiation pattern of IFA one excited at 660 MHz

As expected, the 3D field radiation pattern, shown in Figure 6.3.4, has been dramatically changed by the introduction of the second IFA. The ECC was calculated, using Eq. (6.1), to be 0.659, which indicates very poor performance.

6.4 SVAM Design

A hexagonal unit cell was designed with circular rods. The rods had a dielectric constant of 27. 27 was chosen because LairdTM provided us a dielectric powder with that value. The outer part of the unit cell was set to be 2.57, the dielectric constant of the SL material. The unit cell is shown in Figure 6.4.1.

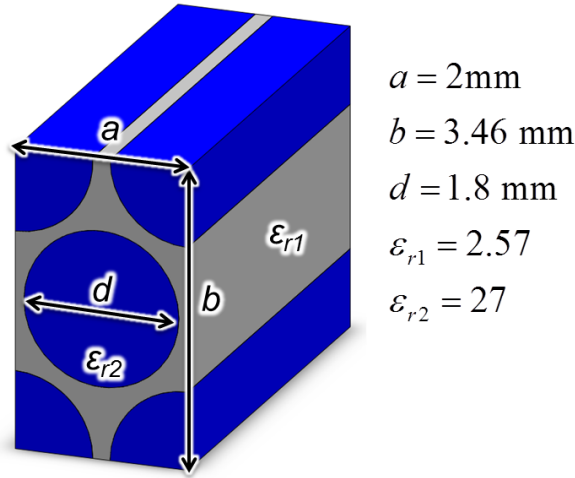


Figure 6.4.1: SVAM unit cell design

The SVAM's rods were spatially varied to have the center rods to be vertical and slowly bend outwards when moving away from the center. This configuration is considered to be a simple canonical configuration of the SVAM and it is possible that better performance could be obtained by exploring other configurations. The SVAM was also designed to be placed completely over both antennas. The SVAM has to be placed where the vertical rods are directly in the middle of the two IFA's and the antennas have to be as close the center of the SVAM as possible. The SVAM design is shown in Figure 6.4.2.



Figure 6.4.2: SVAM to be incorporated in cell phone packaging

6.5 SVAM Reduction of ECC

The SVAM was built into the cell phone case and simulated with HFSS. Both IFAs were present during the simulation.

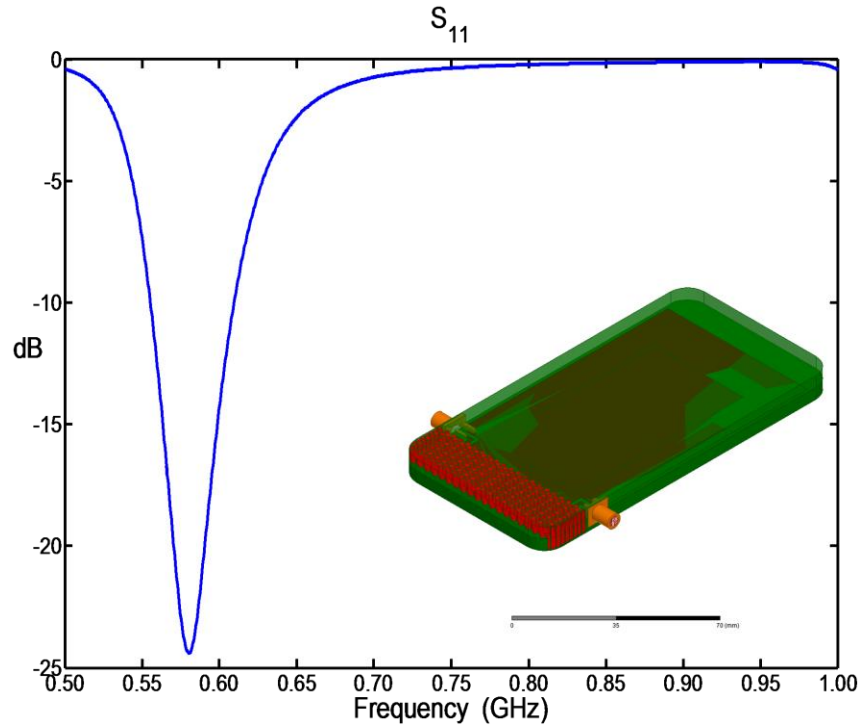


Figure 6.4.2: Simulated cell phone with SVAM

The simulated return loss of the first IFA, even in the presence of the second IFA, was extremely similar to the return loss of one IFA by itself. The resonant frequency has shifted to a lower frequency and is a bit wider, but that is expected because the overall surrounding dielectric constant has increased. This result is attributed to the decrease in the coupling between the two IFAs have decreased. A visualization of the near-field is shown in Figure 6.4.3.

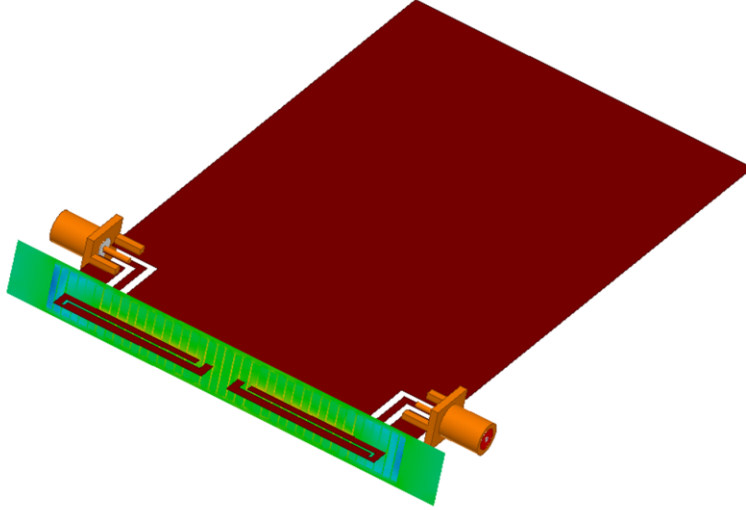


Figure 6.4.3: Near-field of two IFA's embedded in a SVAM

It is obvious from Figure 6.4.3 that the two IFA's are no longer coupled. There are discontinuities in the near field because the dielectric rods are a bit too large for the operating frequency. This particular hole size was used because it is at the limit of what SL can print. The ECC was calculated to be 0.01 using Eq. (6.1).

6.6 Conclusions

A SVAM was successfully designed to be incorporated into the packaging of a cell phone. It was shown through simulation to dramatically improve the ECC of two cell phone antennas in close proximity. The reduction in ECC can lead to denser packaging, smaller size, and more functions. The results are summarized in Table 6.6.1.

Table 6.6.1: ECC

Condition	ECC
Two Antennas	0.659
Two antennas with SVAM	0.013

The ECC reduction, using the designed SVAM, yielded incredible results.

Chapter 7: Conclusions

7.1 Conclusions

The work shown in this dissertation demonstrates that 3D printed all-dielectric spatially variant metamaterials (SVAM's) can be used to mitigate the problems that arise when designing fully 3D devices. All custom numerical tools used were formulated in this dissertation.

First, an all-dielectric uniaxial anisotropic metamaterial was successfully designed, fabricated, and tested. It was manufactured from polycarbonate using a form of 3D printing called fused deposition modeling. The full dielectric tensor was measured in the lab and the experimental results corresponded well to the measured results.

Next, for the first time, an SVAM was used as means to sculpt the near-field around devices. To begin this study, a simple but powerful technique to study transmission lines embedded in spatially variant anisotropic media was outlined. This model was used to show that the near-field can be sculpted almost arbitrarily with minimal change to the properties of the device itself. This conclusion was confirmed with a rigorous 3D model. Based on these results, a microstrip transmission line was isolated from a metal ball placed in close proximity by embedding the line in a SVAM. The presence of the SVAM virtually eliminated any interference of the ball on the microstrip, confirming this novel concept of managing fields in 3D printed systems

Next, to evaluate the impact of surface roughness resulting from 3D printing of metals, two Ku-band horn antennas were 3D printed using EBM. No post-processing steps were taken to polish or otherwise improve the surface finish, which was measured to be on the order of 20 to 40 microns. The antennas were experimentally tested and compared to a standard horn antenna purchased from Pasternack. It was observed that the surface roughness of horn #1 (25.9 μm RMS) had no measurable effect on the performance. Horn #2 had almost twice the surface roughness (39.7 μm RMS) and we measured a 1 dB loss.

Finally, a SVAM was designed to dramatically enhance the performance of cell phone antennas in close proximity. When two cell phone antennas were placed in close proximity the

ECC was 0.659. Then an SVAM was designed to be built into the case of the cell phone that decreased the ECC to 0.01. The cell phone system can be full 3D printed.

7.2 Suggestion for Future Work

The design for the fully 3D printed cell phone is ready to be printed and experimentally verified. The design is shown in Figure 7.2.1.

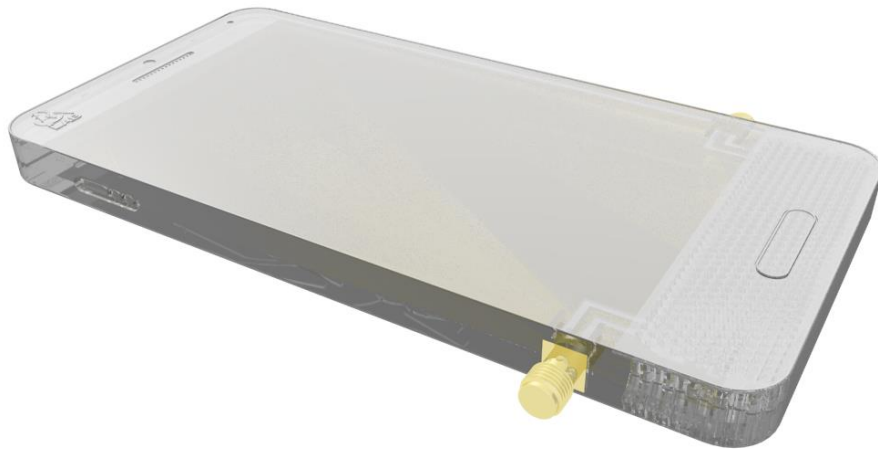


Figure 7.2.1: Cell phone with SVAM design

The SVAM was made to cover the entire area of the antennas. The SVAM could be optimized to only be placed in the necessary location to achieve the same behavior. This leaves more space for additional components or to accommodate smaller size.

All the devices designed in this dissertation used simple canonical configurations for the anisotropy. . Future work could focus on developing a design methodology to improve the technology even more. One possible methodology is the hybridization of TO and the SVL tool.

TO only calculates material properties, whereas the SVL tool calculates the actual geometry that can be directly fabricated. From this perspective, hybridizing the two methods will provide a single tool that can generate a device's geometry directly from a spatial map of the electromagnetic fields. Additional information needed to accomplish this includes lookup tables that quantify the effective properties of different metamaterial unit cells as a function of their

structural parameters. Given this information, the geometry of the metamaterial at each point in the lattice can be determined and the synthesis tool can then generate a smooth and continuous lattice with the prescribed spatial variance. This will be particularly powerful and useful for devices with complex geometries. This idea is depicted in Figure 7.2.2.

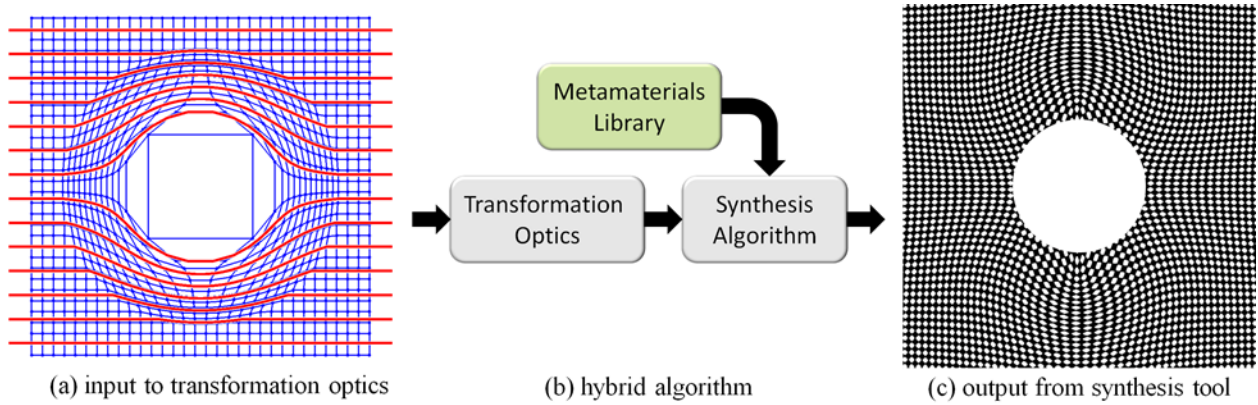


Figure 7.2.2: Illustration of hybrid algorithm composed of transformation optics and spatially variant synthesis

References

- [1] I. Gibson, D. W. Rosen, and B. Stucker, *Additive manufacturing technologies*: Springer, 2010.
- [2] L. B. Gravelle and P. F. Wilson, "EMI/EMC in printed circuit boards-a literature review," *Electromagnetic Compatibility, IEEE Transactions on*, vol. 34, pp. 109-116, 1992.
- [3] D. A. Hill, K. H. Cavcey, and R. T. Johnk, "Crosstalk between microstrip transmission lines," *Electromagnetic Compatibility, IEEE Transactions on*, vol. 36, pp. 314-321, 1994.
- [4] J. Isaacs Jr and N. Strakhov, "Crosstalk in uniformly coupled lossy transmission lines," *Bell Syst. Tech. J.*, vol. 52, pp. 101-115, 1973.
- [5] F. Xiao, W. Liu, and Y. Kami, "Analysis of crosstalk between finite-length microstrip lines: FDTD approach and circuit-concept modeling," *Electromagnetic Compatibility, IEEE Transactions on*, vol. 43, pp. 573-578, 2001.
- [6] J.-P. Kruth, M. Leu, and T. Nakagawa, "Progress in additive manufacturing and rapid prototyping," *CIRP Annals-Manufacturing Technology*, vol. 47, pp. 525-540, 1998.
- [7] G. N. Levy, R. Schindel, and J.-P. Kruth, "Rapid manufacturing and rapid tooling with layer manufacturing (LM) technologies, state of the art and future perspectives," *CIRP Annals-Manufacturing Technology*, vol. 52, pp. 589-609, 2003.
- [8] CustomPartNet. (4/16/14). *Fused Deposition Modeling (FDM)*. Available: <http://www.custompartnet.com/wu/fused-deposition-modeling>
- [9] CustomPartNet. (4/16/2014). *Stereolithography*. Available: <http://www.custompartnet.com/wu/stereolithography>
- [10] D. Cormier, O. Harrysson, and H. West, "Characterization of H13 steel produced via electron beam melting," *Rapid Prototyping Journal*, vol. 10, pp. 35-41, 2004.
- [11] thre3d.com. *How Electron Beam Melting (EBM) Works*. Available: <https://thre3d.com/how-it-works/powder-bed-fusion/electron-beam-melting-ebm>
- [12] R. C. Rumpf, "Computational Electromagnetics (CEM): Lecture Series," ed: University of Texas at El Paso, 2011.
- [13] A. Sihvola, "Metamaterials in electromagnetics," *Metamaterials*, vol. 1, pp. 2-11, 2007.
- [14] N. Engheta, "Circuits with light at nanoscales: optical nanocircuits inspired by metamaterials," *Science*, vol. 317, pp. 1698-1702, 2007.
- [15] C. Caloz and T. Itoh, "Novel microwave devices and structures based on the transmission line approach of meta-materials," in *Microwave Symposium Digest, 2003 IEEE MTT-S International*, 2003, pp. 195-198.
- [16] D. Smith, J. Pendry, and M. Wiltshire, "Metamaterials and negative refractive index," *Science*, vol. 305, pp. 788-792, 2004.
- [17] J. H. Kim and D. C. Park, "A simple method of crosstalk reduction by metal filled via hole fence in bent transmission lines on PCBs," in *Electromagnetic Compatibility, 2006. EMC-Zurich 2006. 17th International Zurich Symposium on*, 2006, pp. 363-366.
- [18] G. E. Ponchak, D. Chun, J.-G. Yook, and L. P. Katehi, "Experimental verification of the use of metal filled via hole fences for crosstalk control of microstrip lines in LTCC packages," *Advanced Packaging, IEEE Transactions on*, vol. 24, pp. 76-80, 2001.
- [19] R. Y. Sharma, T. Chakravarty, and A. B. Bhattacharyya, "Transient Analysis of Microstrip-Like Interconnections Guarded by Ground Tracks," *Progress In Electromagnetics Research*, vol. 82, pp. 189-202, 2008.

- [20] A. R. Mallahzadeh, A. Ghasemi, S. Akhlaghi, B. Rahmati, and R. Bayderkhani, "Crosstalk reduction using step shaped transmission line," *Progress In Electromagnetics Research C*, vol. 12, pp. 139-148, 2010.
- [21] J. H. Wu, J. Scholvin, J. A. del Alamo, and K. A. Jenkins, "A Faraday cage isolation structure for substrate crosstalk suppression," *Microwave and Wireless Components Letters, IEEE*, vol. 11, pp. 410-412, 2001.
- [22] M. Karaboikis, C. Soras, G. Tsachtsiris, and V. Makios, "Compact dual-printed inverted-F antenna diversity systems for portable wireless devices," *Antennas and Wireless Propagation Letters, IEEE*, vol. 3, pp. 9-14, 2004.
- [23] M. K. T. Al-Nuaimi and W. G. Whittow, "Performance investigation of a dual element IFA array at 3 GHz for MIMO terminals," in *Antennas and Propagation Conference (LAPC), 2011 Loughborough*, 2011, pp. 1-5.
- [24] A. Lhilali, A. Diallo, C. Luxey, and P. Brachat, "Multiband multi-antenna system for MIMO WLAN box," in *Antenna Technology and Applied Electromagnetics & the American Electromagnetics Conference (ANTEM-AMEREM), 2010 14th International Symposium on*, 2010, pp. 1-4.
- [25] S. Zhang, A. A. Glazunov, Z. Ying, and S. He, "Reduction of the envelope correlation coefficient with improved total efficiency for mobile LTE MIMO antenna arrays: Mutual scattering mode," *IEEE transactions on antennas and propagation*, vol. 61, pp. 3280-3291, 2013.
- [26] C. Votis, G. Tatsis, and P. Kostarakis, "Envelope Correlation Parameter Measurements in a MIMO Antenna Array Configuration," *Engineering*, vol. 2, 2010.
- [27] Ansys. *Ansys HFSS*. Available: <http://www.ansys.com/Products/Simulation+Technology/Electronics/Signal+Integrity/ANSYS+HFSS>
- [28] D. W. Berreman, "Optics in stratified and anisotropic media: 4×4 -matrix formulation," *JOSA*, vol. 62, pp. 502-510, 1972.
- [29] R. Azzam, "Propagation of partially polarized light through anisotropic media with or without depolarization: a differential 4×4 matrix calculus," *JOSA*, vol. 68, pp. 1756-1767, 1978.
- [30] P. Karasinski, "Application of the 4×4 matrix method for the modeling of planar waveguide sensors," in *Lightguides and their Applications*, 2000, pp. 229-234.
- [31] P. Lin-Chung and S. Teitler, " 4×4 Matrix formalisms for optics in stratified anisotropic media," *JOSA A*, vol. 1, pp. 703-705, 1984.
- [32] N. J. Higham, *Functions of matrices: theory and computation*: Siam, 2008.
- [33] R. Redheffer, "Difference equations and functional equations in transmission-line theory," *Modern mathematics for the engineer*, vol. 12, pp. 282-337, 1961.
- [34] S. Guo and S. Albin, "Simple plane wave implementation for photonic crystal calculations," *Optics Express*, vol. 11, pp. 167-175, 2003.
- [35] S. Johnson and J. Joannopoulos, "Block-iterative frequency-domain methods for Maxwell's equations in a planewave basis," *Optics Express*, vol. 8, pp. 173-190, 2001.
- [36] K. Leung and Y. Liu, "Photon band structures: The plane-wave method," *Physical Review B*, vol. 41, p. 10188, 1990.
- [37] R. Meade, A. Rappe, K. Brommer, J. Joannopoulos, and O. Alherhand, "Erratum: Accurate theoretical analysis of photonic band-gap materials (Phys. Rev. B 48, 8434 (1993))," *Physical Review-Section B-Condensed Matter*, vol. 55, p. 15942, 1997.

- [38] S. Shi, C. Chen, and D. W. Prather, "Plane-wave expansion method for calculating band structure of photonic crystal slabs with perfectly matched layers," *JOSA A*, vol. 21, pp. 1769-1775, 2004.
- [39] H. Sözüer and J. P. Dowling, "Photonic band calculations for woodpile structures," *Journal of Modern Optics*, vol. 41, pp. 231-239, 1994.
- [40] R. C. Rumpf, "Design and optimization of nano-optical elements by coupling fabrication to optical behavior," University of Central Florida Orlando, Florida, 2006.
- [41] R. C. Rumpf, C. R. Garcia, H. H. Tsang, J. E. Padilla, and M. D. Irwin, "Electromagnetic Isolation of A Microstrip by Embedding in a Spatially Variant Anisotropic Metamaterial," *Progress In Electromagnetics Research*, vol. 142, 2013.
- [42] S. Y. Poh, W. C. Chew, and J. Kong, "Approximate formulas for line capacitance and characteristic impedance of microstrip line," *IEEE TRANS. MICROWAVE THEORY AND TECH.*, vol. 29, pp. 135-142, 1981.
- [43] R. C. Rumpf, "Simple implementation of arbitrarily shaped total-field/scattered-field regions in finite-difference frequency-domain," *Progress In Electromagnetics Research B*, vol. 36, 2012.
- [44] S. Boonruang, A. Greenwell, and M. Moharam, "Multiline two-dimensional guided-mode resonant filters," *Applied optics*, vol. 45, pp. 5740-5747, 2006.
- [45] K. S. Yee, "Numerical solution of initial boundary value problems involving Maxwell's equations," *IEEE Trans. Antennas Propag*, vol. 14, pp. 302-307, 1966.
- [46] J. H. Barton, R. C. Rumpf, R. W. Smith, C. Kozikowski, and P. Zellner, "ALL-DIELECTRIC FREQUENCY SELECTIVE SURFACES WITH FEW NUMBER OF PERIODS," *Progress In Electromagnetics Research B*, vol. 41, 2012.
- [47] A. J. Pung, S. R. Carl, I. R. Srimathi, and E. G. Johnson, "Method of fabrication for encapsulated polarizing resonant gratings," *Photonics Technology Letters, IEEE*, vol. 25, pp. 1432-1434, 2013.
- [48] R. C. Rumpf and J. Pazos, "Synthesis of spatially variant lattices," *Optics express*, vol. 20, pp. 15263-15274, 2012.
- [49] J. B. Pendry, D. Schurig, and D. R. Smith, "Controlling electromagnetic fields," *science*, vol. 312, pp. 1780-1782, 2006.
- [50] D.-H. Kwon and D. H. Werner, "Transformation optical designs for wave collimators, flat lenses and right-angle bends," *New Journal of Physics*, vol. 10, p. 115023, 2008.
- [51] D. Schurig, J. Mock, B. Justice, S. A. Cummer, J. Pendry, A. Starr, *et al.*, "Metamaterial electromagnetic cloak at microwave frequencies," *Science*, vol. 314, pp. 977-980, 2006.
- [52] W. Cai, U. K. Chettiar, A. V. Kildishev, and V. M. Shalaev, "Optical cloaking with metamaterials," *Nature photonics*, vol. 1, pp. 224-227, 2007.
- [53] S. Datta, C. Chan, K. Ho, and C. Soukoulis, "Effective dielectric constant of periodic composite structures," *Physical Review B*, vol. 48, p. 14936, 1993.
- [54] A. Krokhin, P. Halevi, and J. Arriaga, "Long-wavelength limit (homogenization) for two-dimensional photonic crystals," *Physical Review B*, vol. 65, p. 115208, 2002.
- [55] A. Nicolson and G. Ross, "Measurement of the intrinsic properties of materials by time-domain techniques," *Instrumentation and Measurement, IEEE Transactions on*, vol. 19, pp. 377-382, 1970.
- [56] G. A. Niklasson, C. Granqvist, and O. Hunderi, "Effective medium models for the optical properties of inhomogeneous materials," *Applied Optics*, vol. 20, pp. 26-30, 1981.

- [57] H. M. Jaeger and S. R. Nagel, "Physics of the granular state," *Science*, vol. 255, pp. 1523-1531, 1992.
- [58] D. Aspnes, "Local-field effects and effective-medium theory: A microscopic perspective," *Am. J. Phys.*, vol. 50, 1982.
- [59] S. Gaytan, L. Murr, E. Martinez, J. Martinez, B. Machado, D. Ramirez, *et al.*, "Comparison of microstructures and mechanical properties for solid and mesh cobalt-base alloy prototypes fabricated by electron beam melting," *Metallurgical and Materials Transactions A*, vol. 41, pp. 3216-3227, 2010.
- [60] L. Murr, S. Gaytan, A. Ceylan, E. Martinez, J. Martinez, D. Hernandez, *et al.*, "Characterization of titanium aluminide alloy components fabricated by additive manufacturing using electron beam melting," *Acta Materialia*, vol. 58, pp. 1887-1894, 2010.
- [61] J. Parthasarathy, B. Starly, S. Raman, and A. Christensen, "Mechanical evaluation of porous titanium (Ti6Al4V) structures with electron beam melting (EBM)," *Journal of the mechanical behavior of biomedical materials*, vol. 3, pp. 249-259, 2010.
- [62] A. Gebhardt, F.-M. Schmidt, J.-S. Hötter, W. Sokalla, and P. Sokalla, "Additive manufacturing by selective laser melting the realizer desktop machine and its application for the dental industry," *Physics Procedia*, vol. 5, pp. 543-549, 2010.
- [63] T. Pereira, M. Silva, M. Oliveira, I. Maia, J. Silva, M. Costa, *et al.*, "Effect of process parameters on the properties of selective laser sintered Poly (3-hydroxybutyrate) scaffolds for bone tissue engineering," *Virtual and Physical Prototyping*, vol. 7, pp. 275-285, 2012.
- [64] C. L. Holloway and E. F. Kuester, "Power loss associated with conducting and superconducting rough interfaces," *Microwave Theory and Techniques, IEEE Transactions on*, vol. 48, pp. 1601-1610, 2000.
- [65] Y. Ning and W. Jiang, "The electromagnetic characteristics of conducting rough surfaces at millimeter wave frequencies," in *Microwave and Millimeter Wave Technology, 2008. ICMMT 2008. International Conference on*, 2008, pp. 326-328.
- [66] Y. Uehara, Y. Suzuki, H. Komagata, T. Tsuruoka, and S. Ushioda, "Electron Energy Loss Spectra Showing the Effects of Surface Roughness and Electromagnetic Retardation---Theory and Experiment," *Journal of the Physical Society of Japan*, vol. 70, p. 2012, 2001.
- [67] N. Chiurtu, B. Rimoldi, I. Telatar, and V. Pauli, "Impact of correlation and coupling on the capacity of MIMO systems," in *Signal Processing and Information Technology, 2003. ISSPIT 2003. Proceedings of the 3rd IEEE International Symposium on*, 2003, pp. 154-157.
- [68] J. Thaysen and K. B. Jakobsen, "Envelope correlation in (N, N) MIMO antenna array from scattering parameters," *Microwave and optical technology letters*, vol. 48, pp. 832-834, 2006.
- [69] R. G. Vaughan and J. B. Andersen, "Antenna diversity in mobile communications," *Vehicular Technology, IEEE Transactions on*, vol. 36, pp. 149-172, 1987.
- [70] P. Panayi, M. Al-Nuaimi, and L. Ivrisimtzis, "Tuning techniques for the planar inverted-F antenna," 1999.

Appendix

A1 Derivation of Expression for Scattering Parameters

$$\begin{bmatrix} \mathbf{W}_1 & \mathbf{W}_1 \\ -\mathbf{V}_1 & \mathbf{V}_1 \end{bmatrix} \begin{bmatrix} \mathbf{c}'^+_1 \\ \mathbf{c}'^-_1 \end{bmatrix} = \begin{bmatrix} \mathbf{W}_i & \mathbf{W}_i \\ -\mathbf{V}_i & \mathbf{V}_i \end{bmatrix} \begin{bmatrix} \mathbf{c}'^+_i \\ \mathbf{c}'^-_i \end{bmatrix} \quad (1.1)$$

$$\begin{bmatrix} \mathbf{W}_i & \mathbf{W}_i \\ -\mathbf{V}_i & \mathbf{V}_i \end{bmatrix} \begin{bmatrix} e^{-\lambda_i k_0 L_i} & \mathbf{0} \\ \mathbf{0} & e^{\lambda_i k_0 L_i} \end{bmatrix} \begin{bmatrix} \mathbf{c}'^+_i \\ \mathbf{c}'^-_i \end{bmatrix} = \begin{bmatrix} \mathbf{W}_2 & \mathbf{W}_2 \\ -\mathbf{V}_2 & \mathbf{V}_2 \end{bmatrix} \begin{bmatrix} \mathbf{c}'^+_2 \\ \mathbf{c}'^-_2 \end{bmatrix} \quad (1.2)$$

Solving (1.1) for $\begin{bmatrix} \mathbf{c}'^+_i \\ \mathbf{c}'^-_i \end{bmatrix}$

$$\begin{bmatrix} \mathbf{W}_i & \mathbf{W}_i \\ -\mathbf{V}_i & \mathbf{V}_i \end{bmatrix}^{-1} \begin{bmatrix} \mathbf{W}_1 & \mathbf{W}_1 \\ -\mathbf{V}_1 & \mathbf{V}_1 \end{bmatrix} \begin{bmatrix} \mathbf{c}'^+_1 \\ \mathbf{c}'^-_1 \end{bmatrix} = \begin{bmatrix} \mathbf{c}'^+_i \\ \mathbf{c}'^-_i \end{bmatrix} \quad (1.3)$$

Substituting (1.3) into (1.2)

$$\begin{bmatrix} \mathbf{W}_i & \mathbf{W}_i \\ -\mathbf{V}_i & \mathbf{V}_i \end{bmatrix} \begin{bmatrix} \mathbf{X}_i & \mathbf{0} \\ \mathbf{0} & \mathbf{X}_i^{-1} \end{bmatrix} \begin{bmatrix} \mathbf{W}_i & \mathbf{W}_i \\ -\mathbf{V}_i & \mathbf{V}_i \end{bmatrix}^{-1} \begin{bmatrix} \mathbf{W}_1 & \mathbf{W}_1 \\ -\mathbf{V}_1 & \mathbf{V}_1 \end{bmatrix} \begin{bmatrix} \mathbf{c}'^+_1 \\ \mathbf{c}'^-_1 \end{bmatrix} = \begin{bmatrix} \mathbf{W}_2 & \mathbf{W}_2 \\ -\mathbf{V}_2 & \mathbf{V}_2 \end{bmatrix} \begin{bmatrix} \mathbf{c}'^+_2 \\ \mathbf{c}'^-_2 \end{bmatrix} \quad (1.4)$$

Solving $\begin{bmatrix} \mathbf{W}_i & \mathbf{W}_i \\ -\mathbf{V}_i & \mathbf{V}_i \end{bmatrix}^{-1}$

$$\begin{aligned}
& \left[\begin{array}{cc|cc} \mathbf{W}_i & \mathbf{W}_i & \mathbf{1} & \mathbf{0} \\ -\mathbf{V}_i & \mathbf{V}_i & \mathbf{0} & \mathbf{1} \end{array} \right] \\
& \left[\begin{array}{cc|cc} \mathbf{1} & \mathbf{1} & \mathbf{W}_i^{-1} & \mathbf{0} \\ -\mathbf{V}_i & \mathbf{V}_i & \mathbf{0} & \mathbf{1} \end{array} \right] \\
& \left[\begin{array}{cc|cc} \mathbf{1} & \mathbf{1} & \mathbf{W}_i^{-1} & \mathbf{0} \\ \mathbf{0} & 2\mathbf{V}_i & \mathbf{V}_i \mathbf{W}_i^{-1} & \mathbf{1} \end{array} \right] \\
& \left[\begin{array}{cc|cc} & & \mathbf{W}_i^{-1} & \mathbf{0} \\ \mathbf{1} & \mathbf{1} & & \\ \mathbf{0} & \mathbf{1} & \frac{\mathbf{V}_i^{-1} \mathbf{V}_i \mathbf{W}_i^{-1}}{2} & \frac{\mathbf{V}_i^{-1}}{2} \end{array} \right] \\
& \left[\begin{array}{cc|cc} & & \mathbf{W}_i^{-1} & \mathbf{0} \\ \mathbf{1} & \mathbf{1} & & \\ \mathbf{0} & \mathbf{1} & \frac{\mathbf{W}_i^{-1}}{2} & \frac{\mathbf{V}_i^{-1}}{2} \end{array} \right] \\
& \left[\begin{array}{cc|cc} & & 2\mathbf{W}_i^{-1} - \frac{\mathbf{W}_i^{-1}}{2} & -\frac{\mathbf{V}_i^{-1}}{2} \\ \mathbf{1} & \mathbf{0} & & \\ \mathbf{0} & \mathbf{1} & \frac{\mathbf{W}_i^{-1}}{2} & \frac{\mathbf{V}_i^{-1}}{2} \end{array} \right] \\
& \left[\begin{array}{cc|cc} & & \mathbf{W}_i^{-1} & -\frac{\mathbf{V}_i^{-1}}{2} \\ \mathbf{1} & \mathbf{0} & \frac{\mathbf{W}_i^{-1}}{2} & \frac{\mathbf{V}_i^{-1}}{2} \\ \mathbf{0} & \mathbf{1} & \frac{\mathbf{W}_i^{-1}}{2} & \frac{\mathbf{V}_i^{-1}}{2} \end{array} \right] \\
& \left[\begin{array}{cc} \mathbf{W}_i & \mathbf{W}_i \\ -\mathbf{V}_i & \mathbf{V}_i \end{array} \right]^{-1} = \frac{1}{2} \left[\begin{array}{cc} \mathbf{W}_i^{-1} & -\mathbf{V}_i^{-1} \\ \mathbf{W}_i^{-1} & \mathbf{V}_i^{-1} \end{array} \right]
\end{aligned} \tag{1.5}$$

Substituting (1.5) into (1.4)

Substituting (1.9) into (1.7)

$$\mathbf{X}_i \mathbf{A}_{i,i-1} \mathbf{c}_1^{r+} - \mathbf{X}_i \mathbf{B}_{i,i-1} \mathbf{A}_{i,j-1}^{-1} \mathbf{B}_{i,i-1} \mathbf{c}_1^{r+} + \mathbf{X}_i \mathbf{B}_{i,i-1} \mathbf{A}_{i,j-1}^{-1} \mathbf{X}_i \mathbf{B}_{i,i+1} \mathbf{c}_2^{r+} + \mathbf{X}_i \mathbf{B}_{i,i-1} \mathbf{A}_{i,j-1}^{-1} \mathbf{X}_i \mathbf{A}_{i,i+1} \mathbf{c}_2^{r-} = \mathbf{A}_{i,i+1} \mathbf{c}_2^{r+} + \mathbf{B}_{i,i+1} \mathbf{c}_2^{r-} \quad (1.10)$$

Solving (1.10) for \mathbf{c}_2^{r+}

$$\begin{aligned} \mathbf{X}_i \mathbf{B}_{i,j-1} \mathbf{A}_{i,j-1}^{-1} \mathbf{X}_i \mathbf{B}_{i,i+1} \mathbf{c}_2^{r+} - \mathbf{A}_{i,i+1} \mathbf{c}_2^{r+} &= \mathbf{X}_i \mathbf{B}_{i,j-1} \mathbf{A}_{i,j-1}^{-1} \mathbf{B}_{i,i-1} \mathbf{c}_1^{r+} - \mathbf{X}_i \mathbf{A}_{i,i-1} \mathbf{c}_1^{r+} - \mathbf{X}_i \mathbf{B}_{i,j-1} \mathbf{A}_{i,j-1}^{-1} \mathbf{X}_i \mathbf{A}_{i,i+1} \mathbf{c}_2^{r-} + \mathbf{B}_{i,i+1} \mathbf{c}_2^{r-} \\ (\mathbf{A}_{i,i+1} - \mathbf{X}_i \mathbf{B}_{i,j-1} \mathbf{A}_{i,j-1}^{-1} \mathbf{X}_i \mathbf{B}_{i,i+1}) \mathbf{c}_2^{r+} &= (\mathbf{X}_i \mathbf{A}_{i,i-1} - \mathbf{X}_i \mathbf{B}_{i,j-1} \mathbf{A}_{i,j-1}^{-1} \mathbf{B}_{i,i-1}) \mathbf{c}_1^{r+} + (\mathbf{X}_i \mathbf{B}_{i,j-1} \mathbf{A}_{i,j-1}^{-1} \mathbf{X}_i \mathbf{A}_{i,i+1} - \mathbf{B}_{i,i+1}) \mathbf{c}_2^{r-} \\ \mathbf{c}_2^{r+} &= (\mathbf{A}_{i,i+1} - \mathbf{X}_i \mathbf{B}_{i,j-1} \mathbf{A}_{i,j-1}^{-1} \mathbf{X}_i \mathbf{B}_{i,i+1})^{-1} (\mathbf{X}_i \mathbf{A}_{i,i-1} - \mathbf{X}_i \mathbf{B}_{i,j-1} \mathbf{A}_{i,j-1}^{-1} \mathbf{B}_{i,i-1}) \mathbf{c}_1^{r+} + (\mathbf{A}_{i,i+1} - \mathbf{X}_i \mathbf{B}_{i,j-1} \mathbf{A}_{i,j-1}^{-1} \mathbf{X}_i \mathbf{B}_{i,i+1})^{-1} (\mathbf{X}_i \mathbf{B}_{i,j-1} \mathbf{A}_{i,j-1}^{-1} \mathbf{X}_i \mathbf{A}_{i,i+1} - \mathbf{B}_{i,i+1}) \mathbf{c}_2^{r-} \end{aligned} \quad (1.11)$$

Solving (1.7) for \mathbf{c}_2^{r+}

$$\mathbf{c}_2^{r+} = \mathbf{A}_{i,i+1}^{-1} \mathbf{X}_i \mathbf{A}_{i,i-1} \mathbf{c}_1^{r+} + \mathbf{A}_{i,i+1}^{-1} \mathbf{X}_i \mathbf{B}_{i,i-1} \mathbf{c}_1^{r-} - \mathbf{A}_{i,i+1}^{-1} \mathbf{B}_{i,i+1} \mathbf{c}_2^{r-} \quad (1.12)$$

Substituting (1.12) into (1.8)

$$\mathbf{B}_{i,i-1} \mathbf{c}_1^{r+} + \mathbf{A}_{i,i-1} \mathbf{c}_1^{r-} = \mathbf{X}_i \mathbf{B}_{i,i+1} \mathbf{A}_{i,j+1}^{-1} \mathbf{X}_i \mathbf{A}_{i,i-1} \mathbf{c}_1^{r+} + \mathbf{X}_i \mathbf{B}_{i,i+1} \mathbf{A}_{i,j+1}^{-1} \mathbf{X}_i \mathbf{B}_{i,i-1} \mathbf{c}_1^{r-} - \mathbf{X}_i \mathbf{B}_{i,i+1} \mathbf{A}_{i,j+1}^{-1} \mathbf{B}_{i,i+1} \mathbf{c}_2^{r-} + \mathbf{X}_i \mathbf{A}_{i,i+1} \mathbf{c}_2^{r-} \quad (1.13)$$

Solving (1.13) for \mathbf{c}_1^{r-}

$$\begin{aligned} \mathbf{A}_{i,i-1} \mathbf{c}_1^{r-} - \mathbf{X}_i \mathbf{B}_{i,i+1} \mathbf{A}_{i,j+1}^{-1} \mathbf{X}_i \mathbf{B}_{i,i-1} \mathbf{c}_1^{r-} &= \mathbf{X}_i \mathbf{B}_{i,i+1} \mathbf{A}_{i,j+1}^{-1} \mathbf{X}_i \mathbf{A}_{i,i-1} \mathbf{c}_1^{r+} - \mathbf{B}_{i,i-1} \mathbf{c}_1^{r+} - \mathbf{X}_i \mathbf{B}_{i,i+1} \mathbf{A}_{i,j+1}^{-1} \mathbf{B}_{i,i+1} \mathbf{c}_2^{r-} + \mathbf{X}_i \mathbf{A}_{i,i+1} \mathbf{c}_2^{r-} \\ (\mathbf{A}_{i,i-1} - \mathbf{X}_i \mathbf{B}_{i,i+1} \mathbf{A}_{i,j+1}^{-1} \mathbf{X}_i \mathbf{B}_{i,i-1}) \mathbf{c}_1^{r-} &= (\mathbf{X}_i \mathbf{B}_{i,i+1} \mathbf{A}_{i,j+1}^{-1} \mathbf{X}_i \mathbf{A}_{i,i-1} - \mathbf{B}_{i,i-1}) \mathbf{c}_1^{r+} + (\mathbf{X}_i \mathbf{A}_{i,i+1} - \mathbf{X}_i \mathbf{B}_{i,i+1} \mathbf{A}_{i,j+1}^{-1} \mathbf{B}_{i,i+1}) \mathbf{c}_2^{r-} \\ \mathbf{c}_1^{r-} &= (\mathbf{A}_{i,i-1} - \mathbf{X}_i \mathbf{B}_{i,i+1} \mathbf{A}_{i,j+1}^{-1} \mathbf{X}_i \mathbf{B}_{i,i-1})^{-1} (\mathbf{X}_i \mathbf{B}_{i,i+1} \mathbf{A}_{i,j+1}^{-1} \mathbf{X}_i \mathbf{A}_{i,i-1} - \mathbf{B}_{i,i-1}) \mathbf{c}_1^{r+} + (\mathbf{A}_{i,i-1} - \mathbf{X}_i \mathbf{B}_{i,i+1} \mathbf{A}_{i,j+1}^{-1} \mathbf{X}_i \mathbf{B}_{i,i-1})^{-1} (\mathbf{X}_i \mathbf{A}_{i,i+1} - \mathbf{X}_i \mathbf{B}_{i,i+1} \mathbf{A}_{i,j+1}^{-1} \mathbf{B}_{i,i+1}) \mathbf{c}_2^{r-} \end{aligned} \quad (1.14)$$

Putting (1.11) and (1.14) together

$$\begin{bmatrix} \mathbf{c}_1^{r-} \\ \mathbf{c}_2^{r+} \end{bmatrix} = \begin{bmatrix} (\mathbf{A}_{i,i-1} - \mathbf{X}_i \mathbf{B}_{i,i+1} \mathbf{A}_{i,j+1}^{-1} \mathbf{X}_i \mathbf{B}_{i,i-1})^{-1} (\mathbf{X}_i \mathbf{B}_{i,i+1} \mathbf{A}_{i,j+1}^{-1} \mathbf{X}_i \mathbf{A}_{i,i-1} - \mathbf{B}_{i,i-1}) & (\mathbf{A}_{i,i-1} - \mathbf{X}_i \mathbf{B}_{i,i+1} \mathbf{A}_{i,j+1}^{-1} \mathbf{X}_i \mathbf{B}_{i,i-1})^{-1} \mathbf{X}_i (\mathbf{A}_{i,i+1} - \mathbf{B}_{i,i+1} \mathbf{A}_{i,j+1}^{-1} \mathbf{B}_{i,i+1}) \\ (\mathbf{A}_{i,i+1} - \mathbf{X}_i \mathbf{B}_{i,i-1} \mathbf{A}_{i,j-1}^{-1} \mathbf{X}_i \mathbf{B}_{i,i+1})^{-1} \mathbf{X}_i (\mathbf{A}_{i,i-1} - \mathbf{B}_{i,i-1} \mathbf{A}_{i,j-1}^{-1} \mathbf{B}_{i,i-1}) & (\mathbf{A}_{i,i+1} - \mathbf{X}_i \mathbf{B}_{i,i-1} \mathbf{A}_{i,j-1}^{-1} \mathbf{X}_i \mathbf{B}_{i,i+1})^{-1} (\mathbf{X}_i \mathbf{B}_{i,i-1} \mathbf{A}_{i,j-1}^{-1} \mathbf{X}_i \mathbf{A}_{i,i+1} - \mathbf{B}_{i,i+1}) \end{bmatrix} \begin{bmatrix} \mathbf{c}_1^{r+} \\ \mathbf{c}_2^{r-} \end{bmatrix} \quad (1.15)$$

A2 Derivation of Redheffer Star Product

$$\begin{bmatrix} \mathbf{c}'^-_1 \\ \mathbf{c}'^+_2 \end{bmatrix} = \begin{bmatrix} \mathbf{A}_{11} & \mathbf{A}_{12} \\ \mathbf{A}_{21} & \mathbf{A}_{22} \end{bmatrix} \begin{bmatrix} \mathbf{c}'^+_1 \\ \mathbf{c}'^-_2 \end{bmatrix} \quad (1.1)$$

$$\begin{bmatrix} \mathbf{c}'^-_2 \\ \mathbf{c}'^+_3 \end{bmatrix} = \begin{bmatrix} \mathbf{B}_{11} & \mathbf{B}_{12} \\ \mathbf{B}_{21} & \mathbf{B}_{22} \end{bmatrix} \begin{bmatrix} \mathbf{c}'^+_2 \\ \mathbf{c}'^-_3 \end{bmatrix} \quad (1.2)$$

Expanding (1.1) and (1.2)

$$\begin{bmatrix} \mathbf{c}'^-_1 \\ \mathbf{c}'^+_2 \end{bmatrix} = \begin{bmatrix} \mathbf{A}_{11}\mathbf{c}'^+_1 + \mathbf{A}_{12}\mathbf{c}'^-_2 \\ \mathbf{A}_{21}\mathbf{c}'^+_1 + \mathbf{A}_{22}\mathbf{c}'^-_2 \end{bmatrix} \quad (1.3)$$

$$\begin{bmatrix} \mathbf{c}'^-_2 \\ \mathbf{c}'^+_3 \end{bmatrix} = \begin{bmatrix} \mathbf{B}_{11} & \mathbf{B}_{12} \\ \mathbf{B}_{21} & \mathbf{B}_{22} \end{bmatrix} \begin{bmatrix} \mathbf{c}'^+_2 \\ \mathbf{c}'^-_3 \end{bmatrix} \quad (1.4)$$

Separating (1.3) and (1.4)

$$\mathbf{c}'^-_1 = \mathbf{A}_{11}\mathbf{c}'^+_1 + \mathbf{A}_{12}\mathbf{c}'^-_2 \quad (1.5)$$

$$\mathbf{c}'^+_2 = \mathbf{A}_{21}\mathbf{c}'^+_1 + \mathbf{A}_{22}\mathbf{c}'^-_2 \quad (1.6)$$

$$\mathbf{c}'^-_2 = \mathbf{B}_{11}\mathbf{c}'^+_2 + \mathbf{B}_{12}\mathbf{c}'^-_3 \quad (1.7)$$

$$\mathbf{c}'^+_3 = \mathbf{B}_{21}\mathbf{c}'^+_2 + \mathbf{B}_{22}\mathbf{c}'^-_3 \quad (1.8)$$

Substituting (1.7) into (1.6)

$$\begin{aligned} \mathbf{c}'^+_2 &= \mathbf{A}_{21}\mathbf{c}'^+_1 + \mathbf{A}_{22}\mathbf{B}_{12}\mathbf{c}'^-_3 \\ \mathbf{c}'^+_2 - \mathbf{A}_{22}\mathbf{B}_{11}\mathbf{c}'^+_2 &= \mathbf{A}_{21}\mathbf{c}'^+_1 + \mathbf{A}_{22}\mathbf{B}_{12}\mathbf{c}'^-_3 \\ (\mathbf{I} - \mathbf{A}_{22}\mathbf{B}_{11})\mathbf{c}'^+_2 &= \mathbf{A}_{21}\mathbf{c}'^+_1 + \mathbf{A}_{22}\mathbf{B}_{12}\mathbf{c}'^-_3 \\ \mathbf{c}'^+_2 &= (\mathbf{I} - \mathbf{A}_{22}\mathbf{B}_{11})^{-1} \mathbf{A}_{21}\mathbf{c}'^+_1 + (\mathbf{I} - \mathbf{A}_{22}\mathbf{B}_{11})^{-1} \mathbf{A}_{22}\mathbf{B}_{12}\mathbf{c}'^-_3 \end{aligned} \quad (1.9)$$

Substituting (1.6) into (1.7)

$$\begin{aligned}
\mathbf{c}'_2 &= \mathbf{B}_{11}\mathbf{A}_{21}\mathbf{c}'_1 + \mathbf{B}_{11}\mathbf{A}_{22}\mathbf{c}'_2 + \mathbf{B}_{12}\mathbf{c}'_3 \\
\mathbf{c}'_2 - \mathbf{B}_{11}\mathbf{A}_{22}\mathbf{c}'_2 &= \mathbf{B}_{11}\mathbf{A}_{21}\mathbf{c}'_1 + \mathbf{B}_{12}\mathbf{c}'_3 \\
(\mathbf{I} - \mathbf{B}_{11}\mathbf{A}_{22})\mathbf{c}'_2 &= \mathbf{B}_{11}\mathbf{A}_{21}\mathbf{c}'_1 + \mathbf{B}_{12}\mathbf{c}'_3 \\
\mathbf{c}'_2 &= (\mathbf{I} - \mathbf{B}_{11}\mathbf{A}_{22})^{-1}\mathbf{B}_{11}\mathbf{A}_{21}\mathbf{c}'_1 + (\mathbf{I} - \mathbf{B}_{11}\mathbf{A}_{22})^{-1}\mathbf{B}_{12}\mathbf{c}'_3
\end{aligned} \tag{1.10}$$

Substituting (1.9) into (1.8)

$$\begin{aligned}
\mathbf{c}'_3 &= \mathbf{B}_{21}(\mathbf{I} - \mathbf{A}_{22}\mathbf{B}_{11})^{-1}\mathbf{A}_{21}\mathbf{c}'_1 + \mathbf{B}_{21}(\mathbf{I} - \mathbf{A}_{22}\mathbf{B}_{11})^{-1}\mathbf{A}_{22}\mathbf{B}_{12}\mathbf{c}'_3 + \mathbf{B}_{22}\mathbf{c}'_3 \\
\mathbf{c}'_3 &= \mathbf{B}_{21}(\mathbf{I} - \mathbf{A}_{22}\mathbf{B}_{11})^{-1}\mathbf{A}_{21}\mathbf{c}'_1 + (\mathbf{B}_{21}(\mathbf{I} - \mathbf{A}_{22}\mathbf{B}_{11})^{-1}\mathbf{A}_{22}\mathbf{B}_{12} + \mathbf{B}_{22})\mathbf{c}'_3
\end{aligned} \tag{1.11}$$

Substituting (1.10) into (1.5)

$$\begin{aligned}
\mathbf{c}'_1 &= \mathbf{A}_{11}\mathbf{c}'_1 + \mathbf{A}_{12}(\mathbf{I} - \mathbf{B}_{11}\mathbf{A}_{22})^{-1}\mathbf{B}_{11}\mathbf{A}_{21}\mathbf{c}'_1 + \mathbf{A}_{12}(\mathbf{I} - \mathbf{B}_{11}\mathbf{A}_{22})^{-1}\mathbf{B}_{12}\mathbf{c}'_3 \\
\mathbf{c}'_1 &= (\mathbf{A}_{11} + \mathbf{A}_{12}(\mathbf{I} - \mathbf{B}_{11}\mathbf{A}_{22})^{-1}\mathbf{B}_{11}\mathbf{A}_{21})\mathbf{c}'_1 + \mathbf{A}_{12}(\mathbf{I} - \mathbf{B}_{11}\mathbf{A}_{22})^{-1}\mathbf{B}_{12}\mathbf{c}'_3
\end{aligned} \tag{1.12}$$

Combining (1.11) and (1.12) into block matrix form

$$\begin{aligned}
\mathbf{c}'_1 &= (\mathbf{A}_{11} + \mathbf{A}_{12}(\mathbf{I} - \mathbf{B}_{11}\mathbf{A}_{22})^{-1}\mathbf{B}_{11}\mathbf{A}_{21})\mathbf{c}'_1 + \mathbf{A}_{12}(\mathbf{I} - \mathbf{B}_{11}\mathbf{A}_{22})^{-1}\mathbf{B}_{12}\mathbf{c}'_3 \\
\mathbf{c}'_3 &= \mathbf{B}_{21}(\mathbf{I} - \mathbf{A}_{22}\mathbf{B}_{11})^{-1}\mathbf{A}_{21}\mathbf{c}'_1 + (\mathbf{B}_{21}(\mathbf{I} - \mathbf{A}_{22}\mathbf{B}_{11})^{-1}\mathbf{A}_{22}\mathbf{B}_{12} + \mathbf{B}_{22})\mathbf{c}'_3 \\
\begin{bmatrix} \mathbf{c}'_1 \\ \mathbf{c}'_3 \end{bmatrix} &= \begin{bmatrix} \mathbf{A}_{11} + \mathbf{A}_{12}(\mathbf{I} - \mathbf{B}_{11}\mathbf{A}_{22})^{-1}\mathbf{B}_{11}\mathbf{A}_{21} & \mathbf{A}_{12}(\mathbf{I} - \mathbf{B}_{11}\mathbf{A}_{22})^{-1}\mathbf{B}_{12} \\ \mathbf{B}_{21}(\mathbf{I} - \mathbf{A}_{22}\mathbf{B}_{11})^{-1}\mathbf{A}_{21} & \mathbf{B}_{21}(\mathbf{I} - \mathbf{A}_{22}\mathbf{B}_{11})^{-1}\mathbf{A}_{22}\mathbf{B}_{12} + \mathbf{B}_{22} \end{bmatrix} \begin{bmatrix} \mathbf{c}'_1 \\ \mathbf{c}'_3 \end{bmatrix}
\end{aligned} \tag{1.13}$$

Vita

Cesar R. Garcia earned his Bachelors of Science in Engineering Physics from The University of Texas at Brownsville in 2009. During his undergraduate he started working in applied electromagnetics at the Applied Microwave & Electromagnetic Laboratory (AMEL). He developed a novel negative index metamaterial and used it to miniaturize a patch antenna. This work gave him the opportunity to be the only undergraduate to present at the "iWAT 2009 : IEEE International Workshop on Antenna Technology - Small Antennas and Novel Metamaterials". After graduating, he spent the summer working as a summer provost intern, under Dr. Ruyan Guo at the Multifunction Electronic Materials Devices Research Lab (MeMDRL) located at The University of Texas at San Antonio. He worked on simulating the effect of a piezoelectric on an impinging electromagnetic wave. That work led to another peer reviewed publication

Dr. Garcia research is focused on 3D printed electromagnetics. He developed and demonstrated the world's first spatially variant anisotropic metamaterial to sculpt the fields around devices like they are clay. He is using this to isolate electromagnetic components placed in close proximity and to enhance the performance of components forced into awkward form factors. Dr. Garcia developed and tested the world's first 3D printed horn antenna to show that surface roughness can be tolerated. He assisted in the design and demonstration of the world's first spatially variant self-collimating photonic crystal that the team is using to control the flow of waves in all three dimensions. This work is now being implemented at the nano-scale for integrated optical devices. Dr. Garcia is an author on four peer-reviewed journal articles, two as first author, and has more publications pending. He was also a winner of the prestigious NSF Louis Stokes Alliance for Minority Participation Bridge to Doctorate Fellowship.

Dr. Garcia plans on working in industry. After serving some tenure in industry, he plans to return to academia and start his own research group in the area of applied electromagnetics.

Permanent address: 9375 Viscount BLVD Apt 2014
El Paso, TX, 79925

This dissertation was typed by the author.